JOURNAL OF # LOW DIMENSIONAL SYSTEMS
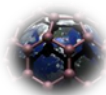
Physics, Chemistry and Biology of Low Dimensional Systems

Aims and scope

Journal of Low Dimensional Systems publishes research and review papers on fundamental aspects of applied physics, chemistry and biology. Papers reporting work on electronic, spectroscopic and structural properties of low dimensional systems, including perfect and defect lattices, surfaces, two-dimensional electron systems, interfaces, thin films and multilayers, amorphous materials, layered-, micro- and nanostructures. This journal accepts articles related to the biomaterials for medical purposes as well.

Typical examples include the preparation and characterization of novel and advanced materials, concerning their electrical, magnetic, optical, thermal and mechanical properties and the application of appropriate experimental and theoretical techniques in these realms.

Journal of LDS

Table of Contents

THE ROLE OF PHYSICAL FACTORS AND NANOTECHNOLOGY IN THE FIGHT AGAINST THE COVID-19 VIRUS

I. S. AHMADOV, M.A. RAMAZANOV

Faculty of Physics, Nano research Center, Department of Chemical-physics of nanomaterials,
Baku State University, Az1148, Z.Khalilov str., 23, Baku, Azerbaijan

This review article provides information on the Covid-19 virus and its infection. The structure of this little-known virus, which is accompanied by respiratory syndrome, the process of infection, the results of scientific research on the genome and the role of physical factors and nanoparticles in the fight against it are given briefly.

1. INTRODUCTION

At now everyone understands that the Covid-19 pandemic is a disaster for humanity. This catastrophe will not only lead to the death of thousands of people, it will be accompanied by a serious collapse of the world economy, deterioration of people's well-being, cracks in relations between countries and, finally, the initial stage of globalization. However, its positive trend is also predicted. These predictions include the improvement of the environment for a certain period of time, the stimulation of fundamental science and technologies, a serious turn in the development of the world and countries, the strengthening of trends in human psychology, humanism and tolerance, and finally the strengthening of human faith.

What is Covid-19? Covid-19 or coronavirus 2 (SARS-CoV-2) is an infection caused by acute respiratory syndrome. Covid-19 is a highly contagious disease that has never been seen before in humans. Although SARS belongs to the same type of virus as coronavirus (SARS-Cov) and influenza viruses, Covid-19 is a different infection in its characteristics. Covid-19 was first discovered in Wuhan, China (in a woman selling in the market), in December 2019, and soon spread around the world. The World Health Organization (WHO) has declared Covid-19 an outbreak of pandemics due to its rate and extent of spread.

Because COVID-19 is a new type of virus, no one is immune to it, which means that the entire population of the world can be exposed to this infection. Scientists are trying to understand how easily and persistently the disease can spread among humans. Based on the available evidence, researchers believe that it not only spreads through the air, but also has other means of transmission. People over the age of 60 are at high risk for Covid-19 infection, while children are at less risk than adults. There are no reports of transmission of the virus from breast-infected pregnant women to infants through breastfeeding.

The virus is called a coronavirus (like a crown) because of the protein protrusions on its surface. There are four main subgroups of coronaviruses, known as alpha, beta, gamma, and delta. Human coronaviruses were first identified in the mid-1960s. They are - 229E, NL63, OC43, HKU1 (beta coronavirus). Other human coronaviruses are MERS-CoV (beta coronavirus or MERS that causes Middle East Respiratory Syndrome), SARS-CoV (beta coronavirus or SARS that causes Acute Respiratory Syndrome), SARS-CoV-2 (new coronavirus causing coronavirus disease 2019 or Covid -19). People around the world are generally infected with coronaviruses 229E, NL63, OC43 and HKU1.
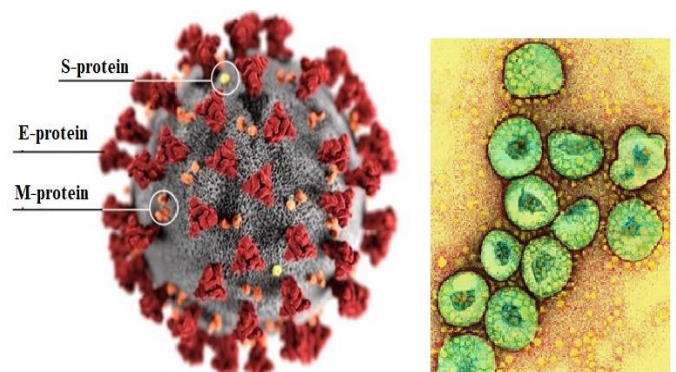

Figure 1. Model (on the left) and a SEM image of cluster of corona viruses (on the right): E- coating protein, S- binding protein, M-membrane protein
© Science Photo Library / Dr. Gopal Murti

2. THE GENETIC STRUCTURE OF THE COVID-19

The genetic structure of the Covid-19 virus suggests that the virus does not resemble known viruses, nor is it a mixture of what expected. This shows that this virus is not an artificially created virus. This virus has unusual features, and have similarities to the recently observed viruses that was in scaly ants, bats , but not completely is same [1]. Covid-19 is one of the largest viruses with a diameter of 60-220 nm and a changeable shape. The glycoprotein coating consists of crown-shaped protrusions. Its genome is much larger than the genome of RNA viruses known so far and is 27-32 kb.

Coronavirus genome comprises (Fig. 2) of 5′ untranslated region (5UTR) including 5′ leader sequence, open reading frame (**orf**) 1a/b (yellow box) encoding non-structural proteins (**nsp**) for replication, structural proteins including envelop (orange box), membrane (red) and nucleoprotein (cyan box), accessory proteins (purple boxes) such as **orf** 3, 6, 7a, 7b 8 and 9b of 2019-nCoV (HKU-SZ-005b) genome, and 3′ untranslated region (3UTR). Examples of each betacoronavirus lineage are human coronavirus (HCoV) HKU1 (lineage A), 2019-nCoV (HKU-SZ-005b) and SARS-CoV (lineage B), Human MERS-CoV and bat CoV HKU9 (lineage C) [2,3].
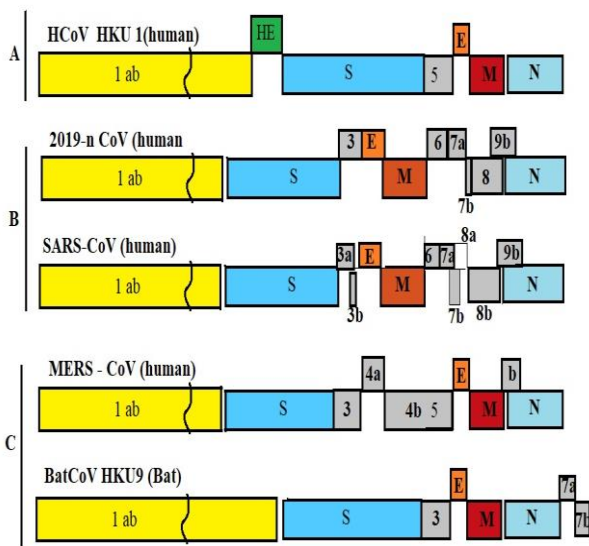
Figure 2.Betacoronavirus genome organization.

3. HOW DOES THE COVID-19 VIRUS ENTER HUMAN CELLS?

The researchers found that the Covid-19 virus (79% homologue of SARS-CoV) first binds by glycoprotein - S, the binding protein in the envelope of virus with the enzyme 2 (ACE2) on the cell membrane, which is responsible for converting angiotensin and then enters the cell (Fig. 3).
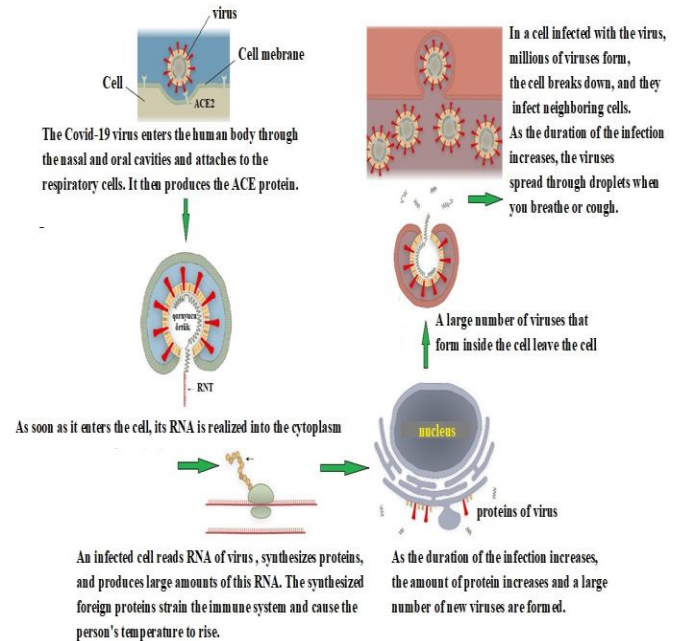
Figure 3. The process of infection and its consequences
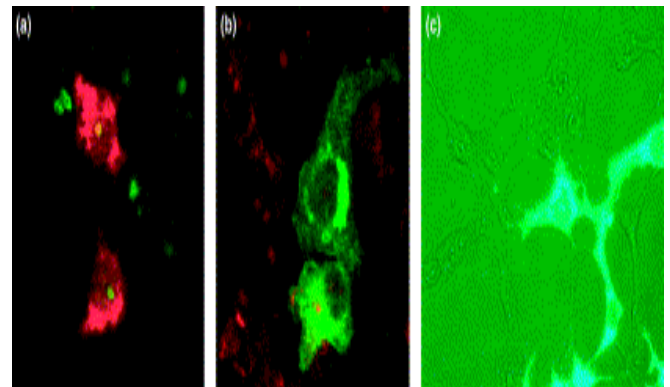
Figure 4.Image of a coronavirus-infected cell under a confocal microscope. Viral proteins are shown in red and nuclear fibrils are shown in green. Most viral proteins remain in the cytoplasm, but nucleoproteins can be localized in the nucleus and distribute fibrillarin. The expression of individual proteins (and mutants) after their localization in the cell has greatly contributed to the study of cornovirus infection. b) the membrane protein is green and the nucleic acid is red. c) phase-contrast image of the cell, the green fluorescent protein that expresses - the protein that combines with the nucleoproteins is given in green (Images (a) and (b) are the courtesy of Torsten Wurm, and image (c) is the courtesy of Jae-Hwan You).

During infection, the S protein breaks down into two subunits, S1 and S2. The binding receptor domain (RBD) of the S1 protein binds directly to the peptidase domain (PD) of ACE2. S2 probably plays a role in its

binding to the membrane. Now the main task is to reveal the mechanism of how Covid-19 is combined with ACE2-B0AT1 complex via RBD. Therefore, all efforts are focused on studying the structure of ACE2. The structure of the ACE2-B0AT1 complex does not allow the development of antiviral drugs, as well as vaccines, as they have not yet been identified. ACE2 blockade plays a key role in preventing Covid-19 infection. Experiments show that Covid-19 forms an S-protein trimer, in which its 2 RBD domains are oriented in one direction (down) and the other domain in the opposite direction (up).

During Covid-19 infection, the immune system causes a fever, because it fights hard to clear the virus. In severe cases, the immune system overreacts and begins to attack lung cells. Fluid and dead cells accumulate in the lungs, the respiratory process slows down, and breathing becomes difficult. As a result, respiratory syndrome develops, which leads to death. The only way to fight Covid-19 infection is to create a vaccine. The vaccine helps the body make antibodies that fight infection, which has not yet been developed for Covid-19. Existing influenza vaccines are not suitable for this virus because the antibodies they produce do not affect the coronavirus.

Figure 5. Drugs currently used in the fight against Covid-19 virus infection

4. HOW IS THE COVID-19 VIRUS IDENTIFIED?

To identify the virus, samples of the fluid from the bronchial alveoli of infected patients are taken and injected into the cells of monkeys or humans, and the virus multiplies in these cells. It has been established that the virus can infect even epithelial cells of the respiratory tract [4]. Using in vitro analysis, it was found that infectious serous infection from cured patients convincingly neutralized [5]. Using the isolated Covid-19 virus, the authors subsequently determined the critical host susceptibility factor [6]. When cultured cells overexpress the transmembrane angiotensin converting enzyme 2 (ACE2) protein from humans, bats, pigs, or civet cats, they become hypersensitive to infection, indicating that ACE2 is a Covid-19 receptor [7]. These data refer to the earlier SARS-CoV, which also uses human and animal ACE2 proteins as receptors and shows a zoonotic distribution that corresponds to its binding to ACE2 receptor orthologs [8]. They also reflect the behavior of the Middle East Respiratory Syndrome (MERS)-CoV, which, although it relies on the separate protein receptor dipeptidyl peptidase 4 (DPP4), is similarly distributed among animal species in correlation with its binding to DPP4 orthologs.

There are quarantine measures to limit the Covid-19 epidemic, but the risk of a global pandemic is real. The development of effective vaccines and antiviral drugs is a priority to reduce the burden of this virus. The immediate objective is to create vaccines based on Covid-19, which contain conserved epitopes and cause widely neutralizing antibodies, as well as virus-specific T-cell responses. Similar daunting challenges lie ahead in identifying safe and effective drugs that inhibit the penetration and replication of SARS-CoV-2, and in developing recommendations for their clinical use. If given too late, they cannot change the course of the disease, even if the viral loads are reduced. Interested research communities can and will rely on fundamental knowledge that already exists and respond accordingly to these challenges.

Methods to combat the Covid-19 virus are improving, and a number of questions need to be answered before a vaccine can be found. One of these questions is to clarify the dependence of the virus on temperature and humidity. Everyone is wondering how the Covid -19 virus will behave as a result of climate change, how its development and rate of infection will change. In hot weather, humidity will the spread and multiplication of the virus decrease when it decreases? Therefore, physicists study how the structure of the virus changes depending on temperature and humidity, and in what cases it spreads. Because of this University of Utah physicists are developing a hollow (genome-free) synthetic cover for the Covid-19 virus to study its resistance to temperature and humidity and the extent of its spread. As the humidity increases, the droplets containing the virus become larger and settle faster in

the air. On the contrary, when the humidity is low, the droplets evaporate rapidly during respiration. Viral droplets can remain in the air for a long time, increasing the time and distance of infection. Dr. Alan Evangelista claims that "there is no guarantee that Covid-19 will behave like known coronaviruses ... the laws of physics must be applied." [8].

It is well known that UV radiation is one of the most effective ways to disinfect air, surfaces and water. It is possible that exposure to ultraviolet rays is a good way to destroy Covid-19 viruses on the surface of human skin, in exposed areas [9]. Known around the world as a UV specialist, Dr. Wladyslaw J. Kowalski recent report by provides the latest information on the UV sensitivity of the Covid-19 virus [10].In fact, one of the most aggressive oxidizing antimicrobial agents known to man is ozone, which reacts to any organic compound by oxidizing double carbon bonds. Ozone is used in various types of hospital rooms, offices, doctor's consultation rooms, quarantine rooms, medical equipment, hand sterilization when mixed with water, etc. can be used effectively in disinfection.

5. THE ROLE OF NANOTECHNOLOGY IN THE FIGHT AGAINST THE COVID-19 VIRUS

What can be the role of nanotechnology in the fight against the Covid-19 virus? The main materials of nanotechnology - nanoparticles - have a very different effect and mechanism in the fight against viruses. Second, nanoparticles have been shown to have biomimetic properties that cause internal antiviral properties [11]. Third, the capsule formulation of drugs allows to increase their stability, ensure dose optimization, and improve delivery to the target by bringing a stable modified structure (with polymers such as polyethylene glycol) (PEG) [12].

"Nanotrap" particles are thermosensitive hydrogels that can capture live infectious virus, viral RNA, and viral proteins [13]. This new type of technology can be expanded to treat infectious diseases such as the influenza virus. Hendricks et al., used liposomes to deliver glycan-sialylneolacto-N-tetraose with (LSTc) - sialosid-synthetic bait for receptor binding influenza results have shown that these liposomes are highly effective for competitive binding and capture of influenza A viruses and can inhibit the infection of target cells in a dose dependent manner [14]. In a study by Li et al. has been shown that [15] modified silver nanoparticles with oseltamivir effectively reduce H1N1 infection by inhibiting the activity of both HA and NA in vitro. It has been shown that the prevention of DNA fragmentation, chromatin condensation, and caspase-3 activity also contributed to the antiviral properties of these nanostructures. The toxicity profiles of these oseltamivir-modified silver nanoparticles, assessed using the cytopathic effect, transmission electron microscopy and cell viability assays, also showed an improvement in MDCK cells compared to the oseltamivir control groups.

A German-Indian research team has developed nanogels with varying degrees of flexibility that mimic cellular HS proteins. Based on dendritic polyglycerol sulfate, this active compound can effectively and continuously bind and protect against viruses, thus preventing infections. Developed nanogels can flexibly adapt to the surface of the virus. This increases their multivalent interaction with viral particles and reduces the likelihood that pathogens will be able to separate again. Researchers have synthesized two sulfated nanogels that act against herpes and arteriviruses in humans and other animals. The generated nano-gels can achieve an inhibitory effect of up to 90 percent. Substances remain active for a relatively long time and also provide protection against viral particles released from already infected cells. Polymer gels are harmless and "safe for cells" - unlike hard, inflexible materials - and can be broken down into smaller fragments and excreted by the kidneys.

For use with recombinant protein C, researchers are considering two types of vaccine adjuvants. Gold nanoparticles (AuNP), which are expected to function as a carrier antigen and adjuvant for immunization; and Toll-like receptor agonists (TLRs), which, as previously shown, are an effective adjuvant in the SARS-CoV ultraviolet inactivated vaccine. Sekimukai H. and his colleagues showed that all mice immunized with more than 0.5 μg S protein without adjuvant escaped from SARS after infection with mouse-adapted SARS-CoV; however, eosinophilic infiltration was observed in the lungs of almost all immunized mice. Protein adjuvant AuNP induced a strong IgG response, but could not improve vaccine efficacy or reduce eosinophilic infiltration due to highly allergic inflammatory reactions. While similar virus titers were observed in control animals and animals immunized with protein S with or without AuNP, type 1 interferon and pro-inflammatory responses were moderate in mice that received protein S with and without AuNP. On the other hand, a TLR agonist adjuvant vaccine induced highly protective antibodies without eosinophilic infiltration, as well as Th1 / 17 cytokines. The results of this study will contribute to the development of vaccines against severe pneumonia-associated coronaviruses [16].

6. CONCLUSION

The Covid-19 is a new and very mysterious virus, many fundamental research centers around the world have been involved in its study. Measures to combat this virus are an improved form of the measures that now exist. Although the structure and genome of the Covid-19 virus do not differ significantly from the viruses studied so far, there are significant differences. This RNA virus is really dangerous because it is a virus that causes respiratory syndrome. Therefore, it is necessary to intensify the fight against nanotechnology under the influence of physical factors. But the key is to find a vaccine for the Covid-19 virus.

7. REFERENCES

1. Andersen K.G. et al. The proximal origin of SARS-CoV-2. Nature Medicine.Published online March 17, 2020. doi: 10.1038/s41591-020-0820-9

2. Chan, J. F.-W., Kok, K.-H., Zhu, Z., Chu, H., To, K. K.-W., Yuan, S., & Yuen, K.-Y./ Genomic characterization of the 2019 novel human-pathogenic coronavirus isolated from a patient with atypical pneumonia after visiting Wuhan. Emerging Microbes & Infections, 9(1), 2020,p.221–236.
   doi:10.1080/22221751.2020.1719902;

3. Chan J.F., Yuan S., Kok K.H., et al. /A familial cluster of pneumonia associated with the 2019 novelcoronavirus indicating person-to-person transmission: a study of a family cluster. Lancet. 2020. doi: https://doi.org/10. 1016/S0140-6736(20)30154-9

4. Zhu, N. et al. /A novel coronavirus from patients with pneumonia in China, 2019. N. Engl. J. Med. 2020, 382, 727–733

5. Zhou, P. et al. /A pneumonia outbreak associated with a new coronavirus of probable bat origin. Nature. Published online February 3, 2020. https://doi.org/ 10.1038 / s41586-020-2012-7

6. Zhou, P. et al. / A pneumonia outbreak associated with a new coronavirus of probable bat origin. Nature. Published online February 3, 2020. https://doi.org/ 10.1038 / s41586-020-2012-7

7. Li, W. et al. /Receptor and viral determinants of SARS-coronavirus adaptation to human ACE2. EMBO J. 2005, 24, p.1634–1643

8. http://www.unews.utah.edu.

9. F. Ansaldi, F. Banfi, P. Morelli, L. Valle, P. Durando, L. Sticchi, S. Contos , I. Gasparini, P. / CROVARISARS-CoV, influenza A and syncitial respiratory virus resistance against common disinfectants and ultraviolet irradiation. Journal of preventive medicine and hygiene, 2004, 45,p.5-8.

10. https://www.researchgate.net/publication/3398 87436_2020_COVID-19_Coronavirus_Ultraviolet_Susceptibility [doi: 10.13140 / RG.2.2.22803.22566]

11. Gagliardi M. /Biomimetic and bioinspired nanoparticles for targeted drug delivery. Ther Deliv., 2017; 8: 289–299. Doi: 10.4155 / tde-2017-0013.

12. Gabizon A, Catane R, Uziely B, et al./ circulation time and enhanced accumulation in malignant exudates of doxorubicin encapsulated in polyethylene-glycol coated liposomes. Cancer Res 1994; 54: 987–992.

13. Shafagati N, Patanarut A, Luchini A, et al. / The use of "nanotrap" particles for biodefense and emerging infectious disease diagnostics. Pathog Dis 2014 , 71,p.164–176

14. Hendricks GL, Weirich KL, Viswanathan K, et al./ Sialylneolacto-N-tetraose C (LSTc) - bearing liposomal decoys capture influenza A virus. J Biol Chem 2013, 288,p.8061–8073.

15. Li Y, Lin Z, Zhao M, et al. / Silver nanoparticle based codelivery of oseltamivir to inhibit the activity of the H1N1 influenza virus through ROS-mediated signaling pathways. ACS Appl Mater Interfaces 2016, 8,p.24385–24393.

16. Sekimukai, H., Iwata - Yoshikawa, N., Fukushi, S., Tani, H., Kataoka, M., Suzuki, T., Nagata, N./ Gold nanoparticle - adjuvanted S protein induces a strong antigen - specific IgG response against severe acute respiratory syndrome - related coronavirus infection, but fails to induce protective antibodies and limit eosinophilic infiltration in lungs. Microbiology and Immunology, 2019. doi: 10.1111 / 1348-0421.12754

INFLUENCE OF DOPING MATERIAL ON OPTICAL PARAMETRIC OSCILLATION in $Hg_{1-x}Cd_xGaS_4$ CRYSTAL

SH.A. SHAMILOVA

Baku State University, Az1148, Z.Khalilov str., 23, Baku, Azerbaijan

In this work, we study the parametric interaction with allowance for the phase change of the interacting pump, signal, and idler waves in the infrared spectrum materials in the case of a doped $Hg_{1-x}Cd_xGa_2S_4$ crystal. The values of refractive indexes, angle of phase matching and angular dispersion coefficient of the second-order were calculated with phase matching of 90 degrees.

1. INTRODUCTION

Tunable parametric sources of coherent radiation in combination with the effects of frequency mixing permit to extend considerably the field of tunable wavelengths of laser radiation. The optical multipliers of frequency serve this task too. The optical parametric generators of the mid-infrared region of spectrum are successfully used for for studying semiconductor elements for optical communication systems, the basic components of a new generation of lidar-gas analyzers [1], scientific and medical devices.

However, for the implementation of these tasks, coherent radiation sources with the necessary energy parameters and efficiency are necessary. To solve the mentioned problems of modern nonlinear optics, the search for promising materials continues.

Optical nonlinear infrared crystals (IR), such as $ZnGeP_2$, $AgGaSe_2$, $AgGaS_2$ and $HgGa_2S_4$ [2-4] owing to their unique properties, have become of great interest in application of the middle and far infrared range. IR crystals have a large effective optical nonlinearity [5–10].

The complication of the composition of crystals allows varying their physical properties in wide range and as a result to satisfy the requirements for the elemental base of nonlinear optics.

The choice of mercury thiogallate crystals is due to some considerations. First of all, on the basis of this crystal we can produce parametric generation, where technologically developed and popular Nd: YAG lasers can be used as a pump source (λ_p=1.064 mcm), the signal wavelength λ_s=1.5772 mcm. The output for idler wave occurs on right mirror which has 80-90% of transmission (λ_i= 3.27 mcm). Another reason is the high transmittance of radiation in the range of 12-15 microns. In addition, these crystals have a high nonlinear susceptibility, radiation resistance, and higher mechanical hardness [11].

As can be seen from [11-15], an admixture of cadmium in mercury thiogallate changes the main values of the refractive index and nonlinear coefficients in $Hg_{1-x}Cd_xGa_2S_4$, which means, for example, if the nonlinear coefficient in $HgGa_2S_4$ is 15.57 pm/V, then for $Hg_{1-x}Cd_xGa_2S_4$ it 1.6 times higher and equal to 24.94 pm/V. According to the experiment the value for double refraction is very sensitive to the parameter x. Hence, by changing the part of Cd in the crystal (parameter x), we can establish double refraction, a condition for phase matching, and we can implement a non-critical phase matching mode.

The theoretical investigation of nonlinear interaction mainly are carried by numerical analysis for nonlinear interaction of optical waves. But the analytical method is more appropriate for the sake of better physical clarification. The most known analytical method is constant field approximation [16]. At parametric interaction it is necessary to take into account the threshold character of parametric generation to which the losses and phase mismatch of interacting waves make considerable contribution. The simultaneous account of these two factors may be provided by theoretical analysis of wave interaction in the constant intensity approximation [17, 18], which work well for reverse reaction of excited wave to exciting waves.

In this work, we study in detail the parametric generation of laser radiation in $Hg_{1-x}Cd_xGa_2S_4$ crystal based on theoretical consideration of nonlinear interaction of waves while phase variation of all waves are taken into account. The comparison of the obtained results has been made on conversion efficiency with

existing experimentally measured values. Calculation indexes of refraction for $Hg_{1-x}Cd_xGa_2S_4$ at difference wavelength and the angular disperse coefficient of the second order. To show the ways of increasing intensity of idler wave.

2. THEORY

To consider a wide range of tasks in the theory of nonlinear waves, it is necessary to solve a system of coupled nonlinear differential equations, the so called reduced equations.
Let us analyze the process of parametric generation of the Nd:YAG laser in a crystal with length l. In this crystal the optic wave with frequency ω_p of generates idler wave with frequency of ω_i and signal waves ω_s ($\omega_p = \omega_i + \omega_s$). At this stage we can use the known system of reduced equations [16]. Uncritical phase matching with $\Theta=90^o$ and $\phi=45^o$ of first type takes place. Let's take a look at e→00 scalar interaction which is characterized by nonlinear coefficient and is 24.94 pm/V [11-12].

$$\frac{dA_i}{dz} + \delta_i A_i = -i\gamma_i A_p A_s^* \exp(i\Delta z)$$

$$\frac{dA_s}{dz} + \delta_s A_s = -i\gamma_s A_p A_i^* \exp(i\Delta z) \qquad (1)$$

$$\frac{dA_p}{dz} + \delta_p A_{pi} = -i\gamma_p A_i A_s \exp(-i\Delta z)$$

When we solve this system using the constant intensity approximation at the exit of crystal, we get the following

$$I_i(\ell_1) = I_{io} \exp(-2\delta_i \ell_1)\left[\cosh^2 q_3\ell_1 + \left(\frac{\Delta}{2} + \frac{\gamma_i A_{so}^* A_{po}}{A_{io}}\right)^2 \frac{\sinh^2 q_3\ell_1}{q_3^2}\right] \quad (2)$$

expression for idler wave intensity [9]:
where

$$q_3^2 = \Gamma_p^2 - \Gamma_s^2 - \frac{\Delta^2}{4}$$

$$\delta = \delta_s + \delta_i + \delta_p, \quad p = \delta - i\Delta,$$

$$q_1^2 = p^2/4 - q, \quad q = \Gamma_s^2 - (\Gamma_p)^2 + \delta_i\left(\delta_s + \delta_p - i\Delta\right),$$

$$\Gamma_s^2 = \gamma_i\gamma_p I_{so}, \quad \Gamma_p^2 = \gamma_s\gamma_i I_{p0}, \quad q_2^2 = q - p^2/4,$$

$$P = \left(\delta_i - \delta_s - \delta_p + i\Delta\right)/2.$$

Here $A_{so,io,po}$ are initial values for complex amplitude of signal, idler and pump waves at respective frequencies along the z-axis (at the left entry of the crystal). For j –th wave (j=s, i, p) the nonlinear and linear absorption coefficients are shown by γ_j and δ_j, and $\Delta = k_p - k_s - k_i$ is the phase mismatching between interacting waves.

The values of amplitudes of pump and signal waves are calculated at the input by upcoming considerations in single resonator while the parametric amplification of idler wave is considered. The standard technique [19] is used to theoretically investigate the parametrical three-wave interaction for two pass of optical resonator by pump and signal waves. For this purpose the reduced system of equations have been solved in the constant intensity approximation for each pass of resonator with corresponding boundary conditions.
The sides of the sample were made transparent in the experiment but the value of Fresnel dissipation is not diminished even when these waves are perpendicular to the crystal. For interacting waves in [11] the absorption coefficients are taken from experimental measurements and they are equal to 0.2 cm^{-1} for pumping waves, 0.3 cm^{-1} for signal wave and 0.4 cm^{-1} for idler wave.

It should be noted that at the analysis in constant intensity approximation not only the phases and losses of interacting waves are considered but also partial reduction of pumping and signal waves is taken into account which is the result of energy transfer from excited waves to exciting one. So the constant intensity approximation is used for each of two transitions of a crystal.

It follows from formula (2) that, in the presence of a wave mismatching and with a nonzero amplitude of the idler wave at the boundary of the nonlinear medium, the phase of the amplified wave depends on the pump intensity. at large pump intensity ($\Gamma > \delta$, Δ) and large interaction lengths ($q_i z > l$), one can find an expression for the threshold pump amplitude ($\delta_i = \delta_p + \delta_s$) [19]. An analysis in the contant intensity approximation gives the following expression for the threshold value of the wave amplitude. [19]

$$\left|\exp\left(-pz/2 + q_i z\right)\right| = 1$$

$$\exp\left(-\delta_i + q_i\right) = 1$$

$$q_i^2 = \frac{(2\delta_i - i\Delta)^2}{4} - \left[\Gamma_s^2 - \Gamma_p^2 + \delta_i\left(\delta_i - i\Delta\right)\right] = \delta_i^2$$

$$A_{po,thresh}(\ell) = \sqrt{\frac{\Gamma_s^2 + \delta_i^2 + \Delta^2/4}{\gamma_i\gamma_s}} \qquad (3)$$

If the pump amplitude is less than the threshold, then parametric amplification is generally impossible.
Under conditions of synchronism, but with various losses, the threshold pump amplitude

$$A_{po,thresh}(\ell) = \sqrt{\frac{\Gamma_s^2 + \delta_i(\delta_s + \delta_p)}{\gamma_i \gamma_s}} \qquad (4)$$

It follows from (3) and (4) that the threshold pump amplitude increases with mismatch and dissipative losses in the medium. In addition to these parameters, the threshold amplitude of the pump is influenced by a factor that takes into account the inverse effect of the excited waves on the phase of the pump wave ($\gamma z \neq 0$). The larger the parameter $\Gamma_s = \gamma_i \gamma_p I_{so}$, the higher the threshold amplitude of the pump.

As we know, $Hg_{1-x}Cd_xGa_2S_4$ in mixed structure is affected by cadmium composition. Let's identify the wavelength of idler and signal waves in $Hg_{1-x}Cd_xGa_2S_4$ crystal at the wavelength of 1.064 mcm at 90° synchronism. By choosing x=0.25 for cadmium concentration, the experimental value of wavelength of signal and idler waves are specified for this case which are presented in Refs. [12, 15]. Here the equation $\frac{1}{\lambda_p^e} = \frac{1}{\lambda_i^e} + \frac{1}{\lambda_s^o}$ of should be established for the sake of parametric generation of the radiations at pumping wavelength of 1.064 mcm and 3.274 mcm. From here we can get the proper value of 1.5772 mcm for wavelength of signal wave. The main values of refraction indices for wavelength of waves under study are derived from Sellmeier equation [12, 15], and $n_p^{o,e}$, $n_s^{o,e}$, $n_i^{o,e}$ are taken from tables 1

$$n^2(\lambda) = A_1 + A_3/A_2 - \lambda^2 + A_5/A_4 - \lambda^2$$

Table 1

n	A_1	A_2	A_3	A_4	A_5
n_o	7,62356	836,474	-1642,64	0,0717384	-0,220695
n_e	7,41107	805,268	-1512,04	0,0714881	-0,207339

In the experiment for real frequency converters, it is impossible to ensure a condition of phase agreement (phase matching $\Delta = 0$). An error in following the condition of phase matching determines the width of phase matching. Spectral width of pump radiation line, deviation from phase matching angle due to divergence of laser radiation, and instability of temperature for a crystal converter all contribute to mismatch. Hence received information, in particular, on angular width of phase matching, will permit to calculate the maximum divergence of light beam for pumping.

Let us estimate deviation angle from the direction of phase matching $\Delta\theta$ for the negative single-axis $Hg_{0.7}Cd_{0.3}Ga_2S_4$ crystal in case of parametric generation radiation at wavelength of 3.03 mcm (phase matching

of the first type, ee→o interaction). The calculation was carried out using the coefficients in the Sellmeier relation for the main values of refractive indices [12]. To determine the angular width of phase matching we will calculate the angular disperse coefficient according to Ref. 20.

In case of 90-degree phase matching the angular dispersion coefficient of the second order in our case (e→oo scalar interaction at parametrical generation) looks like

$$\frac{\partial^2 \Delta k}{\partial \theta^2} = \left(2\pi \cos\theta \sin\theta \left[\frac{n_o^p\left((n_e^p)^2 - (n_o^p)^2\right)}{\lambda_p\left(\sqrt{(n_o^p)^2 + ((n_e^p)^2 - (n_o^p)^2 \cos^2\theta)}\right)^3} \right] \right)'$$

$$\frac{\partial^2 \Delta}{\partial \theta^2} = -\frac{2\pi\left[(n_p^e)^2 - (n_p^o)^2\right]}{\lambda_p(n_p^o)^2}$$

$$\Delta k(\theta) = \frac{1}{2}\gamma_2(\theta - \theta_s)^2 \qquad (5)$$

In the Table below, the values of refractive indices, the angle of phase matching and angular dispersion coefficient of the second-order are provided for $Hg_{0.7}Cd_{0.3}Ga_2S_4$

Table 2

λ, mcm	n_o^ω	n_e^ω	Phase matching type	deff, pm/V	θs, degree	Angular dispersion coefficient of the second order, cm $^{-1}$ ang. min. $^{-2}$
1.064 (pump)	2.430288	2.39899	e→oo			
1.5772 (signal)	2.405065	2.367763	e→oo	24.94	90	0,0000634955
3.27 (idler)	2.386262	2.35255	e→oo			

3. RESULTS AND DISCUSSION

To study the parametrical frequency conversion in middle IR-range, we will make the numerical calculation of the analytical expression (2), which is received in the constant-intensity approximation. The parameters of the task are chosen according to conditions of existing experiments for the given $Hg_{1-x}Cd_xGa_2S_4$ crystal [11-15].

In Fig. 1 the dynamic process of parametrical amplification of idler wave $I_i(\ell)$ is shown on cited pumping intensity I_{po} at the condition of phase mismatching for two variants of Γ_s/Γ_p and losses. As is seen from figure, parametric gain at different losses starts at various values of pumping
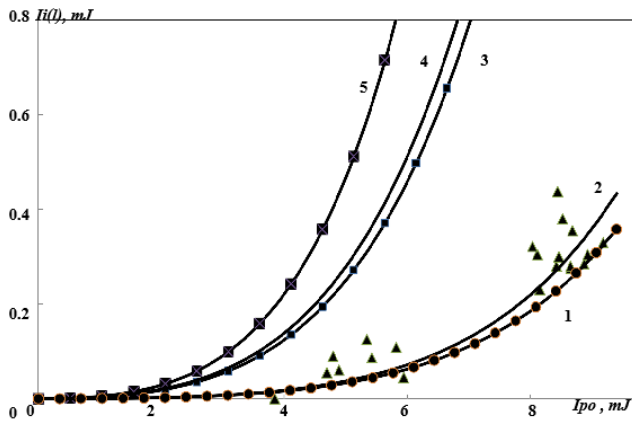
intensity

Figure 1. Dependences of gain coefficient of idler wave in Hg$_{0.75}$Cd$_{0.25}$Ga$_2$S$_4$ crystal $I_i(\ell)$ (as a function of the pump intensity I_{po} (λ=1.064 mcm) (experimental dots from Ref. 1 and curves 1-5) calculated in the constant-intensity approximation for $\delta_i= \delta_p$ =0.15 cm^{-1} (curve 5), $\delta_i= \delta_p$ = 0.2 cm^{-1} (curve 3) and δ_i= 0.15 cm^{-1}, δ_p =0.2 cm^{-1} (curve 4) at $\Delta/2\Gamma_p$=0.1 (curves 2-5), 0.3 (curve 1), crystal length of ℓ =1.1 cm [12, 13, 15]. Γ_s/Γ_p =0.0004 (curves 1-2), 0.005 (curves 3-5).

(curves 1–5). With an increase of pumping intensity the first horizontal section of dependence is observed, i.e. parametric reinforcement is absent. Then at the definite value of pumping intensity, i.e. at threshold amplitude of pumping, the notable raising of dependence begins. With the increase of losses, the growth of dependence takes place at greater values of threshold intensity of pumping (compare curves 3–5). So, from the numerical analysis (2) (for $\Delta/2\Gamma$p=0.1) it follows that in case of parametric interaction in Hg$_{1-x}$Cd$_x$Ga$_2$S$_4$ crystal, threshold intensity of pumping is equal to I$_{po}$=0.37 MW/cm^2 (0.25 mJ) at δ_i =0.2 cm^{-1}, δ_p = 0.2 cm^{-1} (curve 3); at δ_i =0.15 cm^{-1}, δ_p = 0.2 cm^{-1}, it is equal to I$_{po}$=0.3 MW/cm^2 (0.2 mJ) (curve 4); and at δ_i = 0.15 cm^{-1}, δ_p = 0.15 cm^{-1} reaches the value I$_{po}$=0.15 MW/cm^2 (0.1 mJ) (curve 5).

Also parametrical gain grows with increasing of parameter Γ_s/Γ_p (compare curves 2 and 5) and decreasing of phase mismatching (compare curves 1 and 2).

Here in addition to the numerical calculation of the expression (2) (curves 1-4) experimental points are used from Ref. 1. More the best agreement between theoretical and experimental results is observed at value of parameter Γ_s/Γ_p =0.0004 in the range of experimentally used values of pump intensity from 3 mJ up to 10 mJ. As is seen in Fig. 1 it is observed both

theoretically and experimentally that monotonous increase of $I_i(\ell)$ occurs when pump intensity grows.

By using the data provided in the table, dependencies of parametric conversion efficiency on angular mismatching $\Delta\theta$ are presented in Fig. 2 for Hg$_{0.75}$Cd$_{0.25}$Ga$_2$S$_4$ crystal at two values of pump intensity (Γ_s/Γ_p =0.005 and 0.0004). Just as one should expect, the dependencies are of nonmonotonous character. With the increase in pump intensity, conversion efficiency also increases (compare curves 2–3).
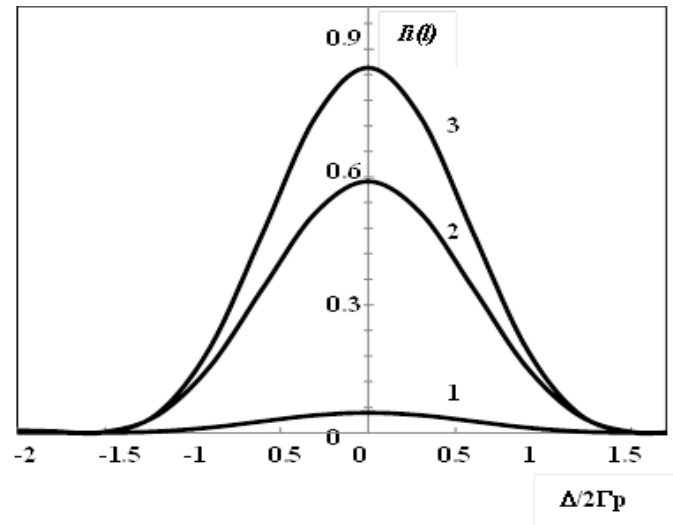
Figure 2. Dependences of gain coefficient of idler wave in Hg$_{0.75}$Cd$_{0.25}$Ga$_2$S$_4$ crystal on phase mismatching $\Delta/2\Gamma_p$ for δ_p=0.2 cm^{-1}, δ_i =0.15 cm^{-1} (curves 1-3), at pump intensity I$_{po}$=9 MW/cm^2 (curves 1-2), 11.8 MW/cm^2 (curve 3) and Γ_s/Γ_p =0.0004 (curve 1), 0.005 (curves 2-3).

From the numerical analysis of the analytical expression (2) for idler wave intensity, obtained in the constant-intensity approximation, it follows that the width of angular phase matching is being changed by pump intensity. As we see in this figure, when pump intensity increases 1.31 times, the idler intensity increases 1.45 times (curves 2 and 3) and at the same time the width of curve for phase matching $I_i(\Delta\theta)$ decreases to 9%. For comparison the curve 1 calculated for other value of relation Γ_s/Γ_p =0.0004 is given here. The increase in the given relation, i.e. intensity of signal wave, conducts to growth of parametrical gain (to compare curves 1 and 2).

As is seen from dependence of $I_i(\Delta\theta)$ on angular width of phase mismatching chosen at 1/2 of maximum efficiency (Fig. 3), angular width is equal to 7.240, when we calculate it for Hg$_{0.75}$Cd$_{0.25}$Ga$_2$S$_4$ crystal length of 11 mm and pump intensity equal to 9 MW/cm^2. To compare, in case of 3 mm long CGA crystal, angular width of phase matching makes up

4.240 [21], when pump intensity is equal to 0,0012 MW/cm^2. By comparing the behavior of curves 1 and 2 (Fig.3), it is seen that the change of $I_i(\Delta\theta)$ by 5.1 % takes place in the angular range of changes from −30 mrad to +30 mrad. The curve 1 becomes more flat in comparison with curves 2 and 3. It testifies the transition to the regime of uncritical character of crystal towards following condition of phase matching; thus, for instance, in AgGaSe$_2$ crystal the change of conversation efficiency by 0.036% takes place in the angular range of changes from −0.6 mrad to +0.6 mrad [22]. Hence the weak changes of efficiency dependence on angular mismatch from phase matching direction takes place at small values of pump intensity (compare curves 2 and 3). Similar slight changes of conversion efficiency under deviation from direction of phase matching, i.e. the uncritical regime of the considered crystals can be realized at low levels of intensity for pump and signal waves.
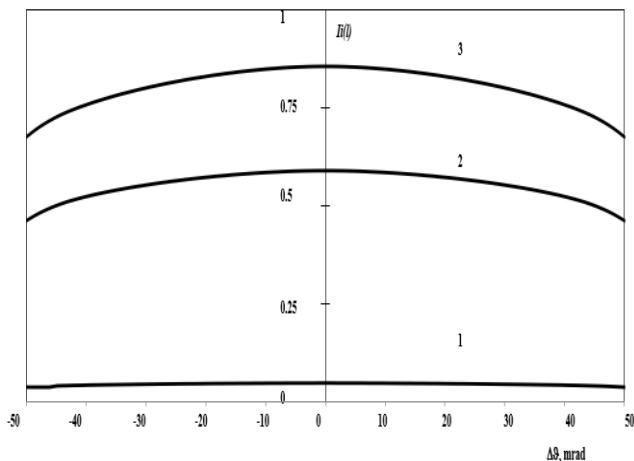

Figure 3. Dependences of gain coefficient of idler wave in Hg$_{0.75}$Cd$_{0.25}$Ga$_2$S$_4$ crystal on angular mismatching $\Delta\Theta$ for δ_p=0.2cm^{-1}, δ_i =0.15 cm^{-1} (curves1-3) at pump intensity I$_{po}$=9 MW/cm^2 (curves 1-2), 10 MW/cm^2 (curve 3) and Γ_s/Γ_p =0.0004 (curve 1), 0.005 (curves 2-3).

4. CONCLUSION

Thus, from the results of the analysis of nonlinear interaction of optical waves with account for phase effects and comparison of them with existing experimental data, it is possible to state that by the choice of optimum values of parameters (pumping intensity, linear tuning with account for impact of linear losses in a medium) an efficiency of parametric conversion in the considered crystals of middle IR range may be increased and the condition for increasing degree of uncritical angular phase matching is possible to choose. Therefore, based on these crystals we can produce parametric generation where technologically developed and popular Nd:YAG lasers could be used as pumping resource. This will draw nearer the creation of the efficient sources of coherent radiation, which is tunable by frequency in the middle-IR region of spectrum.

The developed method can be used to study other nonlinear optical processes, e.g. sum frequency and harmonic generation, etc. in other perspective crystals.

5. REFERENCES

1. Kasumova R.J./ Proceeding of Asia Pacific Conference on fundamental prob. Of Opto and microelectronics and international Work Shop on optical beam transformation Vladivostok, Russia 2001, p.65-68.
2. Das S. / Kvantovaya elektronika. 42 (2012) 228-230.
3. Qeyko P.P. / Optika atmosferi i okeana, 2003, №9, p.16
4. Schunemann P.G., Setzler S.D., Pollak T.M., J./ Cryst. Growth, 2000, 211 (1-4), p.257.
5. Shamilova Sh.A., Kasumova R.J./ Materials digest of the X International Scientific and Prac. Conf. "Trends of modern science 2014", Sheffield, 2014, v.23,58-60.
6. Shamilova Sh.A., Kasumova R.J. / International J. Of Scientific & Technology Research, 2014, 3, Issue 6, p.189-192.
7. Kasumova R.J., Shamilova Sh.A., Safarova G.A., Gadyieva L.S. /International J. of Engineering and Sciences, IJET-IJENS' , 2015, Issue 02, p.15.
8. Kasumova R.J., Mamedov H.M., Shamilova Sh.A., Mamedova V.C. /Materials of 8th International Scientific Conference «Science and Society» (SCIEURO-ISPC), UK, London, 2015, 24-29 November, p.43-46.
9. Kasumova R.J. /An Indian J: Material Science, 2014, 10, Issue 8, p.306-311
10. Kasumova R.J. /Materialy IX Miedzynarodowejnaukowi-konferencji "Europejskanauka XXI-2013" 07-15 maja 2013, 27, Matematyka, Fizyka, Budownictwo i architektura, Przemysl, Nauka I studia, p.41-44
11. Badikov V.V., Kuzmin N.V., Laptev L.B., Malinovski A.L., Mitin K.V., Nazarov G.S., Ryabov E.A., Seryogin A.M., Schebetova N.I. / A study of the optical and thermal properties of nonlinear mercury thiogallate crystals, Quantum Electronics, 2004, 34(5), p. 451-456.
12. Badikov V.V., Don A.K., Mitin K.V., Seryogin A.M., Sinaiskiy V.V., Schebetova N.I. / Optical parametric oscillator on an Hg1-

xCdxGa2S4 crystal, Quantum Electronics, 2005, 35(9), 853- 856.

13. Petrov V. /Parametric down-conversion: The coverage of the mid-infrared spectral range by solid-state laser sources, Optical Materials. 2012, 34,p.536-554.

14. Andreev S.A., Andreeva N.P., Barashkov M.S., Badikov V.V., Demkin V.K., Don A.K., Epihin V.M., Krimski M.I., Kalinnilov Yu.M., Mitin K.V., Seryogin A.M., Sinaiskiy V.V., Talalaev M.A., Chistyakov A.A., Schebetova N.I., Shetinkina T.A. / Investigation of frequency tuning methods of light parametrical oscillators of vision and IR ranges, Quantum Electronics, 2010,40(4),p.288-295.

15. Badikov V.V., Don A.K., Mitin K.V., Seryogin A.M., Sinaiskiy V.V., Schebetova N.I. / A study of the optical parametric oscillator on an Hg1-xCdxGa2S4 crystal in the spectral range from 4 to 6 mcm, Laser physics, 2004, 4, p.23-24.

16. Akhmanov S. A., Khokhlov R. V. / Problemy Nelineynoy Optiki [The Problems of Nonlinear Optics] (VINITI, Moscow, 1965).

17. Tagiev Z.H., and Chirkin A.S. / Fixed intensity approximation in the theory of nonlinear waves, Zh. Eksp. Teor. Fiz. 73, 1977, p.1271-1282.

18. Tagiev Z.H., Kasumova R.J., Salmanova R. A., and Kerimova N.V. / Constant-intensity approximation in a nonlinear wave theory, J. Opt. B: Quantum Semiclas. Opt. 3 2001, p.84-87.

19. Tagiev Z.A., Amirov Sh.Sh. /On the efficiency of the optical parametric oscillation in the prescribed intensity approximation, Soviet Journal of Quantum Electronics 16,1989,p.2243-2247.

20. Dmitriev V.G., and Tarasov L.V. / Prikladnaya Nelineynaya Optika [Applied NonlinearOptics] (Radio I Svyaz, Moscow, 1982).

21. Kasumova R.J. / Second optical harmonic generation of CO2 laser radiation in CGA crystal, J. of Nonlinear Optical Physics & Materials, 2013, 22(2), 1350023-1-13.

22. Kasumova R.J. / Second harmonic of laser radiation for IR-range in mixed AgGa0.6In0.4Se2 crystals, An Indian J: Material Science, 2014, v.10(8), p. 306-311.

INFLUENCE OF TEMPERATURE AND TIME REGIME OF CRYSTALLIZATION ON PP+ZrO$_2$ NANOCOMPOSITE STRUCTURE AND DIELECTRIC PROPERTIES

H.S. IBRAHIMOVA

Institute of Physics. Azerbaijan National Academy of Sciences, pr. H.Javid 33 AZ1143, Baku, Azerbaijan

There have been investigated dielectric properties of PP+ 3% ZrO$_2$ nanocomposite obtained within different temperature and time regimes of crystallization before and after electrothermapolarization (ETP) as well as the formation of temperature hysteresis of electric constant. The causes of dielectric constant magnitude growth due to the crystallization conditions have been revealed. It is expected that in the formation of dielectric hysteresis the charge carries resulting from thermal generation in nanoparticle and penetrating into the composite volume by injection processes are taken part. To estimate the relation of the crystalline and non-crystalline phases in the volume roentgenograms of PP+ 3% ZrO$_2$ based polymer composite materials have been obtained

1. INTRODUCTION

It is difficult to conceive of advanced receive without creating new materials of high service properties for sensor technology. Today a great attention is paid to the composite material development on the base of polymers with metallic oxide fillers. Given fillers allow electric and thermal conduction, magnetic characteristics, electric properties and other functional properties of nanomaterials over a wide range to be modified [1, 2]. They are used as pressure transducers, active material for sensors, solar battery cells, cathode material for reversible lithium current sources, ultraviolent radiation traps, etc. Investigation carried out in given work are aimed at revealing dependencies of nanocomposite dielectric properties on the base of propylene and zirconium oxide obtained within different crystallization regimes before and after electrothermapolarization (ETP).

2. EXPERIMENTAL

PP+ZrO$_2$ nanocomposites have been produced in the following way: powders of isotactic propylene of nanoparticles 0.5 – 1.0 mkm in size at T 120 C are dissolved in toluene ZrO2 – 3 mol % Y2O3 nanopowders of particles 20 – 25 nm in size have been added into initial liquid polymerization system without cooling the polymer solution at the same temperature. By method of hot pressing there have been prepared samples 70 – 100 mkm in thickness from given powders at PP melting temperature and pressure 10MPa.

In given work we use 3 regimes to control temperature and time of crystallization regime. After hot pressing the samples have been cooled at PP melting temperature and pressure 10 MPa for 10 min with different rates: from 2 to up to 2000 deg/min at slow regime with the rate (β ≈ 2 deg/min), by placing melted samples into ice-water mixture (β ≈ 20 deg/min) and liquid nitrogen medium (β ≈ 2000deg/min). The composition has been undergone the electrothemopolarization at Tm = 373 K for tp = 1 hour under the action of electric field at different voltages [3]. To produce nanocomposites the following polarization regime on usually set: samples are heated up to T = 373 K then they are kept for 1 hour approved constant electric field, then they are cooled there. The samples are interposed between the metal electrodes. AS a voltage source the high-voltage rectifier has been used (for instance, VSM – 989).

Dielectric properties have been measured in static mode of operation. Dielectric constant and dielectric loss tangent have been indicated by automatic bridge E 8 – 4 over the frequency range 100 – 10^6 Hz and at T 280 - 420 K. X-ray phase studies are carried out on diffractometer D2 Phaser at the regime of the reflection (Bragg – Bretons geometry) using Cuka – radiation (mean wavelength λ = 1, 5406 A nickel β – filter) Registration has been carried out at continuous operation on the interval of cugles 2Ө = 0.50 – 800 . Crystallographic, structural examinations, calculations have been made by using EVA and TOPAZ programs

3. RESULTSAND DISCUSSION

In Fig. (1) and (2) there have been presented dependencies of dielectric constant and dielectric loss tangent on the frequency of for PP + 3% ZrO_2 nanocompositions obtained within different crystallization regimes unexposed and exposed to ETP at electric intensity $E = 10*10^6$ V/m.
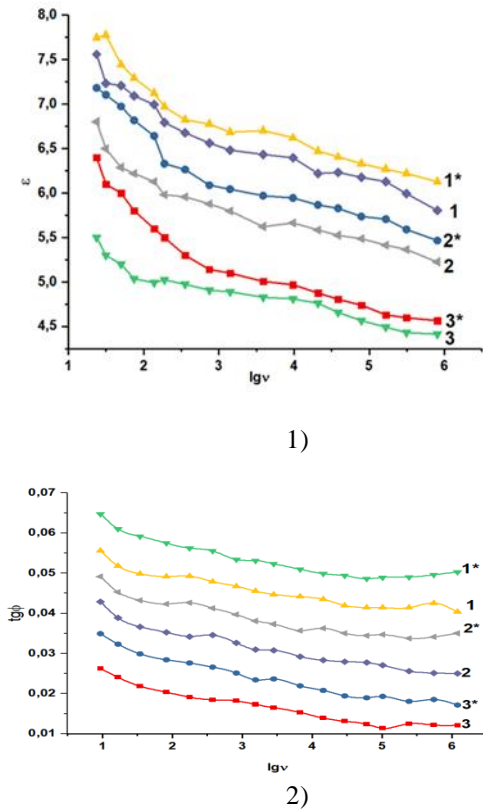

1)

2)

Figure 1. Dependencies of dielectric constant (ε) and tgδ on frequency for PP + 3% ZrO_2 obtained at different crystallization regimes unexposed and exposed to ETP at electric intensity $E = 10 * 10^6$ V/m.

1 and 1* are the samples obtained at QC regime before and after ETP

2 and 2* are the samples obtained at NQ regime before and after ETP

3and 3* are the samples obtained at SC regime before and after ETP

One can suppose from frequency dependence that loss at measured frequencies is due to free carriers. At low frequencies ε and tgδ have high values. We can conclude that the growth of ε and tgδ is related to the increase crystalline phase. It should be noted that at SC regime the samples have minimum value of given parameters that are likely related to the sample heat cleaning and high sizes of supramolecular formation in polymer matrix which bring about the decrease of relaxation processes. High values of sample parameters obtained at QC regime derive from the

fact that charge carriers move in amorphous phase which is in highly elastic state in our experimental condition. The decrease of cooling rate leads to the increase of crystallinity degree and it is one of the causes of tgδ and ε increase of samples obtained in SC regime comparing with tgδ and ε of samples obtained in QC regime. From the other hand it can be explained by a great number of carbon group forms by propylene chain oxidation in SC process.

In Fig. 3 (a, b, c) there have been presented dependences of dielectric constant on the temperature at heating and cooling regime of PP + 3% ZrO_2 nanocompositions obtained at QC regime, unexposed and exposed to ETP at electric intensity $E = 10 * 10^6$ V/m.
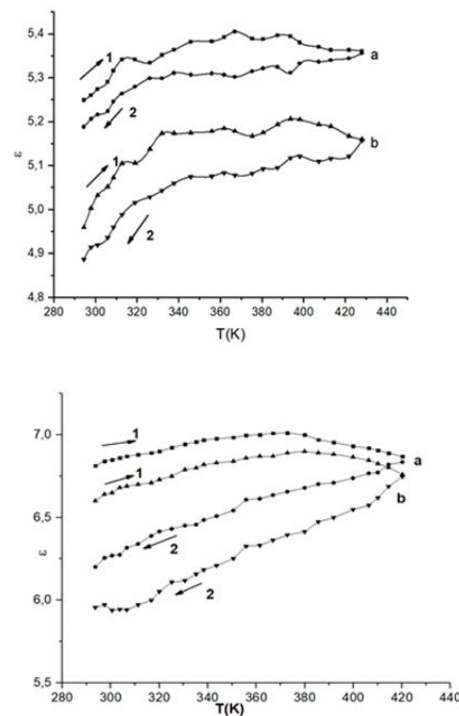
Figure 2. (a, b) Dependences of dielectric constant on the temperature at heating regime (1) and cooling (2) for PP + 3% ZrO_2 nanocompositions obtained at crystallization regimes of QC and SC unexposed (a) and exposed (b) to ETP at electric intensity $E = 10 * 10^6$ V/m.

The formation of dielectric constant temperature hysteresis is seen from the figure. It is shown that by changing the temperature within the interval 300 – 415 K the dependence as part of the subsequent cycle follows its behavior. This phenomenon has been revealed for nanocomposites obtained at QC and SC regimes. Further heating during the first cycle and transfer from above mentioned temperature range establish the stabilization of dielectric constant magnitude [4].

It is anticipated that in the formation of dielectric

16

hysteresis the charge carriers resulting from thermal generation in nanoparticle and penetrating in composite volume by injection processes are taken part. Material heating leads to the rise of carrier concentrations focused on nanoparticles and create the possibility of breaking through their potential barrier at interphase boundary. After the carrier falls within the nanocomposite volume it can be trapped by polymer molecular giving rise to its polarizability that brings about the increase of dielectric constant. Increase polarizability can keep until the filled trap liberates or the carrier can be captured by a district trap. After ETP the numbers of polarization charges are increased. It is seen from hysteresis area [5]. The effect like this can be used in creating electronics, elements of energy-indepedent memory and a number of transducers.

Increase of crystallization rate causes the formation of more complex structures. The degree of polymer crystallinity, size and form of its crystalline regions depend on the crystallization rate. By increasing the temperature to a greater degree there has been occurred the destruction of super molecular structures that result in the decrease of crystallization rate. It is established that the change behavior of super molecular structure (SMS) and properties of polymer composite depend on both the nature of filler its concentration and method of production. The influence of SMS on the kinetics of phase changers has been studied by method of reontgenography. In many case X-ray crystal analytics is the method of phase composition control. To estimate the relation of crystalline and no crystalline phases in the volume the roentgenograms of polymer composite PP + 3% ZrO_2 based materials have been obtained. In Fig.3 there have been presented roentgenograms of PP + 3% ZrO_2 compositions obtained at different crystal regimes. The view of roentgenograms can be explained by the presence of closely certain crystalline and amorphous regions. The proportion of amorphous phase varies over a wide range due to crystallization conditions.
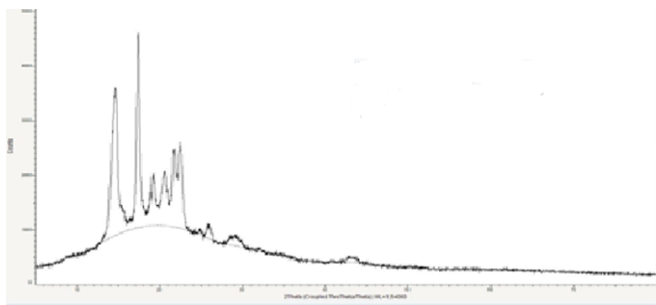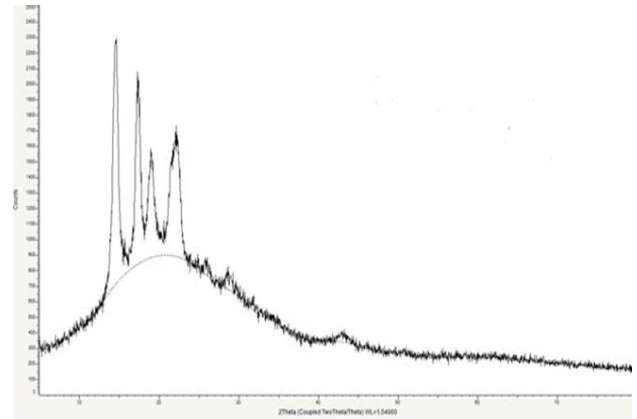
b)
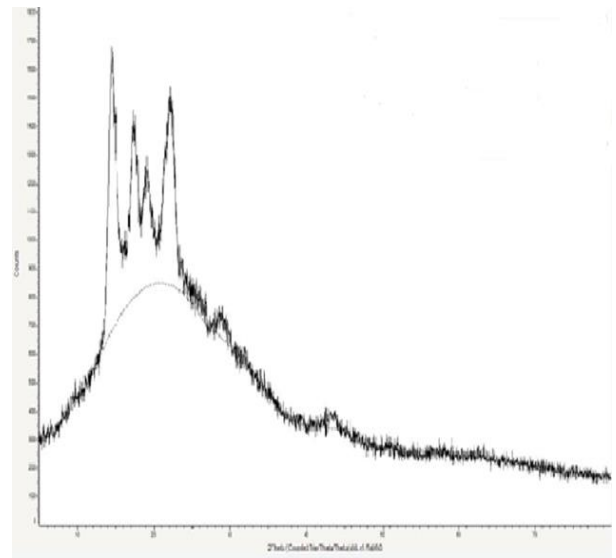
c)

Figure 3. Roentgenograms for nanocomposites obtained at SC (a), NQ (b) and QC (c)

It is seen from roentgenograms that the change of crystallization regime substantially affect the intensity and position of crystal reflections. Samples obtained at QC regime are characteristic of less intensive broadened reflections than the samples obtained at SC and NQ regimes. One can conclude that the increase of cooling rate brings about the decrease of intensity and number of reflections. Sample roentgenograms are indicative of amorphization at high cooling raters of the sample. While investigating the roentgenogram results one can draw up the following table

a)

Crystallization regime	Crystalline phase (%)	Amorphous phase (%)
Slow cooling	39,8	60,2
Quick cooling	28,3	71,7
Nitrogen quenching	30,2	69,8

4. CONCLUSION

Thus one can conclude that the changes of nanocomposite dielectric properties obtained at different crystallization conditions at measured frequencies are caused by free carriers. High values of dielectric characterizes of samples obtained at QC derive from the fact that charge carriers move in amorphous phase which is in highly elastic state in our experimental conditions. It is shown that by changing the temperature within the interval 300-415K the dependence as part of the subsequent cycle follows its behaviors. The thermal hysteresis is obtained .Besides it is seen from roentgenograms that the samples obtained at QC are characteristic of less intensive broadened reflections. Then the samples obtained at SC and NQ, i.e. the change of crystallization regime substantially affect the intensity and position of crystalline reflections.

5. REFERENCE

1. Qavrilova O.E., Nikitina L.L. / Influence of quality of plastic fittings on the quality of light industry products // Vestnik , Kazan Technological Universitety.№22,2013,p.164-166.
2. Qavrilova O.E., L.L.Nikitina,N.S. Kanayeva, O.Y.Yerkina/ Review of advanced polymer materials used in light industry production.// Vestnik , Kazan Technological Universitety 2015,p.276-278.
3. Ramazanov M.A., Ibrahimova H.S., Hajieva F.V./ Influence of electrothermopolarization conditions on strength and electret properties of PP+ZrO2 nanocompositions. Conference Modern Trends of Physics, 2019, p 76-79.
4. Magerramov A.M, Mamedova R.L., Ismailov I.M, Bagirbekov Kh.B./ Dielectric properties of nanocomposities polypropylene nanoclays of Na+ montmorillaonite at heating –cooling regime. J. TP,vol.87, is.9,2017, p.1367-1370.
5. Qriqoryev E.I, Zavyalova S.A., Chvalun S.N. / Thermal hysteresis of nanocomposite dielectric properties on the base of oxide and sulphide nanoparticles of transmition metals in high pressure polyethylene matrix Letters, JTP, vol 30, is. 8, 2004, p.40-45.

NAPHTHALENE OIL AND NANOTECHNOLOGY

M.A.RAMAZANOV, F.V.HAJIYEVA, I.N.HUSEYNOV, N.A.GOZELOVA

Baku State University, Department Chemical Physics of Nanomaterials,
Faculty of Physics, AZ1148, Baku, Azerbaijan

The article has presented a brief overview of studies on the current state of the studies of the chemical composition of oil in the Naphthalene field and identifies the main application areas of the therapeutic Naphthalene oil. It is shown that a distinctive feature of the composition of medical naphthalene oil is the presence of a significant amount of hydrated saturated cyclic hydrocarbons, including decahydronaphthalenes, in contrast to fuel oil. It has been established that the therapeutic effect of naphthalene oil causes not only one type of hydrocarbon, but a combination of various naphthenic compounds contained in the oil, which may include both steranic and triterpanic hydrocarbons, as well as bridged hydrocarbons of the articulation type. Was studied the possibility of using nanotechnology to vary the physicochemical properties, including the optical, antibacterial, antiseptic and other properties of naphthalene oil.

1. INTRODUCTION

Naphthalene oil is the onlymedical oil in the world and represents a unique balneologyfactor, which is unparalleled in the world both in physicochemical and biological characteristics and in itsmedicinalproperties. By its origin, it is younger than industrial types of oil, and is characterized by a relatively high oxygen content, high density and the presence of high molecular weight organic compounds with a cyclic structure. The special properties of naphthalene oil are due to the structure of its many hydrocarbons, their combination in separate fractions and the nature of the nitrogen and sulfur compounds of naphthenic acids [1-4]. The physicochemical and biological effects of Naphthalene oil were first investigated in the works of A.I.Karaev and Yu.G.Mamedaliev. The main goal of these studies was to study the possibility and justification of the prospects for the use of naphthalene in the treatment of a number of diseases in human medicine, as well as in veterinary practice [2,5]. These two outstanding scientists laid the foundations fora whole direction in the study of medicaloil - the allocation of individual groups of hydrocarbons from it and the subsequent testing of their physiological activity in animal experimentations. According to Yu.G.Mammadaliev, during use Naphthtalan oil, the latter supplies the body with intermediate synthesis products that promote the formation of hormones, vitamins and other substances [1]. These authors found that, at right dosages, naphthalene oil has a beneficial effect on the secretory and motor functions of the stomach in hypoacid and hyperacid conditions, has a normalizing effect on vascular tone in hypotension and the initial stages of hypertension, and with an appropriate method of use it has a normalizing effect on liver function - enhances bile formation and biliary excretion, has a peculiar hormone-like effect on the function of sex hormones, etc. [1]. It is established that naphthalene also has an estrogenic effect. In 40-50% of patients, naphthalene can have a desensitizing effect, which is very important in the treatment of infectious and allergic diseases (rheumatic and infectious, non-specific polyarthritis). The content of uric acid in the blood decreases under the influence of the course of treatment in most patients, especially in patients with gouty polyarthritis. Against this background, naphthalene has an anti-inflammatory and analgesic effect in the treatment of joint diseases.

A comprehensive study of Naphthalene oil showed that only the upper part of the geological section of the deposits of the main oil-bearing stratum of the Naphthalene field of the Maykop suite is saturated with medicaloil. In its lower part lies light industrial oil [6]. Naphthalene consists of various hydrocarbons: naphthenic (from 50 to 55%), aromatic (on average up to 15%), resins (30-35%), naphthenic acids (from 0.5 to 1%) are also present in its composition, the amount of water reaches 10-15%. A significant amount of water is easily separated from naphthalene with 1-2 days of settling and using special technical cleanings, and it becomes a thick oily substance. By specific gravity (from 0.927 to 0.970) naphthalene is classified as a heavy oil. The high specific gravity of naphthalene is explained by its fractional and chemical composition: firstly, the low content of light fractions -

gasoline, naphtha and kerosene (from 5 to 15%), as well as paraffin hydrocarbons and, a high content of resins, naphthenic and aromatic hydrocarbons. However, the therapeutic effect of naphthalene is not caused by a large specific gravity. The therapeutic effect of naphthalene is explained by the polycyclic nature of naphthenic hydrocarbons. The peculiarity of naphthenic hydrocarbons of naphthalene is that they have a polycyclic structure, they have more than five cycles in the molecule and a small number of hydrocarbon atoms in the side chains [7].

Based on numerous analyzes, the authors of [8] determined that Naphthalene medical oil and its fractions differ in both group and individual hydrocarbon composition from combustible (industrial) oils and oil fractions of various fields in Azerbaijan. The medicaloil fractions consist exclusively of naphthenic and aromatic hydrocarbons. It was also found that as the boiling temperature of the fractions of naphthalene oil increases, the content of aromatic hydrocarbons in them increases (up to 57%) while reducing the amount of naphthenic. Based on the study of the composition of the fractions 180–300; 300–350, 400–450°C of medical naphthalene oil it is concluded that naphthalene oil, unlike other oils found in Azerbaijan, does not contain paraffin hydrocarbons and gasoline fractions. Unlike similar fractions of other oils found here, the kerosene fraction of naphthalene oil contains more than two times more hexahydroaromatic hydrocarbons than aromatic ones. In the kerosene fraction of naphthalene oil, benzene derivatives are eight times higherthan bicyclic aromatic hydrocarbons.

It was noted in [9] that the oil of the Naphthalene field is heavy (ρ_4^{20} = 937,6 kg/m^3), resinous (16.7%), lies at a shallow depth (~ 400 m), contains 0.15% of the total and 0, 0695% of basic nitrogen, and also 0.21% of sulfur. Naphthalene oils are highly viscous -162.4 mm^2/s at 20°C, 21.5% of naphthenoparaffin hydrocarbons and up to 40% of tar-asphaltene substances are contained in medicaloil, low-paraffin oil, alkanes of normal structure are practically absent, characterized by a maximum content of naphthenic hydrocarbons (39%). It is characterized by a high content of bi-, three-, pentacyclic naphthenes, a low content of isoparaffin hydrocarbons and a high content of hybrid cycloalkanoarenes and the highest content of polycycloaromatic hydrocarbons.

In [10] was provided informationon the detection of saturated C_{27}-C_{29}steranesin the saturated hydrocarbon fraction 420–500°C, as well as adiantane, hopanes, α-sitostanes, the isosteranes described in [11] previous studies, indicating a high chemical transformations of naphthenic hydrocarbons of naphthalene oil. It was also noted that the thermodiffusion fractions of the same

name isolated from the temperature fractions of Naphthalene oil 420–500°C and 350–420°C possessed optical activity. In work [11] also reported the identification of 17 individual steranesin the 350–420°C fraction of naphthalene oil, starting with androstane (C_{19}) and ending with rearranged 24-ethylcholestane (C_{29}). It has been established that among the isomers of androstane and pregnane (C_{21}) thermodynamically themost stable one, having the ring articulation, prevails. A relatively high concentration of so-called overgrouped steraneswas also noted, which are usually not typical for steranesof industrial oils of Azerbaijan, but found in oils of other regions, for example, in oils of Western Siberia.

Studying the composition of Naphthalene oil (18 active wells) by the means of modern instrumental analysis methods, such as gas chromatography and mass spectrometry (GC/MS), combined thermal analysis (CTA), elemental analysis (ICP/MS), dynamic light scattering (DLC) and IR/UV spectroscopy (IR/UV), has been described in [12,13,14]. It has been shown that the density of all Naphthalene oil samples varies within the range of 927.6–975.0 kg/m^3, the freezing temperature varies from −15 to −30ºC, and the amount of coke in individual samples reaches 4.54%. For the first time, noble metals were determined by ICP/MS method in all active wells of the Naphthalene field, their content is compared with the presence in the Absheronoil and gas hardness oil fields. The Napthalan oil deposits are superior to other Absheron deposits in the content of precious metals. Using the ICP/MS method, the content of trace elements in the compositions of medicaland fuel naphthalene oils was also studied. In medicalNaphthalene oil, a quantitative predominance of trace elements is noted in comparison with fuel industrial oil. The most important properties of Naphthalene oils, which distinguish them from oils of other deposits, are clearly displayed when compared to the physicochemical properties of hydrocarbons, microelement (ME) composition and etc. Apparently, they were acquired even before migration and subsequent changes. All this is reflected in the increased content of certain trace elements (Ba, Fe, Ni, Ti, Zn, Au, Pd, Pt, Rh, Te), which is possibly associated with their generation and accumulation in rocks due to their interaction with the environment during migration, and also with the fact that the generation of this oil occurred in clayey rocks[8].

Features of the chemical composition of naphthenic hydrocarbons of naphthalene oil determine the versatility and diversity of its therapeutic effect. This action causes not onlyone type of hydrocarbon (for example, cyclopentanoperhydrophenanthrene structure, as was previously assumed), but the totality of various

naphthenic compounds contained in oil, which can include both sterane and triterpanic hydrocarbons, as well as bridging hydrocarbons [15,16].

An original assumption about the possible mechanisms of the physiological action of Naphthalene oil is expressed in the works [15,17]. Having established that the total inhibitory activity (in the content and types of natural antioxidants) of therapeutic oil is 3-4 times greater than thatofindustrial oil, the authors attribute the high biological potential of therapeutic oil to its antiradical inhibitory properties. It was also determined that with the occurrence depth of Naphthalene oil (from the upper to the lower, industrial part of the field), its inhibition indicators decrease. On this basis, the authors establish a correlation of the inhibitory activity and healing properties of naphthalene oil. However, they argue that among the studied oil components, the maximum gross-inhibitory activity occurs in asphaltenes and resins. The concentration of asphalt-resinous substances decreases in the composition of Naphthalene oil With depth along the section of the field,. It is possible that this change in composition to a greater extent affects the decrease in the inhibitory properties of naphthalene oil.

As known, oil and its products have long been used as antiseptic and antimicrobial agents. Some authors are still trying to prove that the therapeutic effect of naphthalene oil in various infectious and parasitic diseases is due to its bactericidal effect. [18]. Opinions on the antimicrobial properties of Naphthalene oil are rather mixed. In 1934, F.I.Yakubov pointed out that staphylococci seeded in crude oil and fuel oil lose their viability within a few days [19]. F.G.Rosenbaum and B.A.Poslovsky also attributed the antiseptic and antibacterial properties of Naphthalene oil [20]. However, further research by F.I.Yakubova, T.S.Asrieva, G.V.Vygodchikova, P.E.Paperno et al. have showed that naphthalene does not have a bactericidal effect on many pathogenic bacteria, and even naphthalene oil can serve as a favorable environment for the growth and reproduction of some pathogenic and saprophytic microorganisms. Studying the microflora in therapeutic baths filled with Naphthalene oil, F.I.Yakubov discovered various types of staphylococci, streptococci and other bacteria that got here from the organisms of patients. This suggests that long-term use of naphthalene baths can become a source of infection. In the 30′s of the XX century, it was established that naphthalene oil is a favorable soil for numerous microorganisms and that many bacteria conserve, losing their virulence in naphthalene, which can be restored by reseeding. N.D.Aliyev found that pure naphthalene oil, freed from drilling water and other impurities, has a bactericidal property, but

drilling water, including water that was part of naphthalene oil, serves as the best nutrient medium for microorganisms [21]. According to G.I.Meshchersky, naphthalene oil has a disinfecting property, as staphylococcus and streptococci that appear in it dry up and lose their virulence. The author is inclined to explain the essence of effect of Naphthalene oil by its bactericidal properties. [22]. N.I.Mitnik did not confirm the antiseptic effect of Naphthalene oil. In his opinion, Naphthalene oil, somewhat inhibiting the growth of cocci, has no effect on Pseudomonas aeruginosa [5]. Since the early XX century, the bactericidal and bacteriostatic effects of naphthalene oil on other types of microorganisms were studied and its direct effect on the characteristics of the course of various infectious diseases was established. Despite the crucial importance of the question of the bactericidal and bacteriostatic effect of naphthalene oil, it has still not been sufficiently studied [18].

The development and improvement of methods of synthesis and the study of nanostructured materials in the last twenty years have caused the rapid development of nanoscience and nanotechnology. Advances in synthesis have made such materials not only more accessible for research and description, but also led, in some cases, to large-scale industrial testing and applications. Nanotechnology has already led to many useful changes in the chemical industry, especially in the processes of catalysis, nanoelectronics, metallurgy, as well as medicine and etc. The authors of work [23] for the first time studied the effect of nanosized particles on the physicochemical properties of industrial oil taken from various fields of the Absheron Peninsula. It was found that aluminum and iron nanoparticles with a particle size of 20 nm have a strong catalytic activity, while splitting hydrocarbons in the wells and thereby increasing the intensity of gas evolution and pressure in the reservoirs. Thus, the authors have shown that the use of nanotechnology can lead to an increase in oil production in old already exploited oil wells.

Given the unique properties of nanosized particles, including antibacterial, antiseptic, photocatalytic, optical, luminescent and other properties, it can be assumed that nanoparticles can also affect the physicochemical properties of naphthalene oil. As noted earlier, despite a large amount of research into the composition and properties of medical naphthalene oil, interest in this issue does not dry out and therefore the use of nanotechnology in naphthalene oil will undoubtedly cause great scientific and practical interest. The authors of work [24] first have studied the effect of silver nanoparticles on the photoluminescent properties of therapeutic naphthalene oil. With the

development of nanotechnology, it has become known that many nanoparticles of metals and metal oxides possess strong antibacterial and antiseptic properties. Among these particles, silver nanoparticles are of great importance. In work [24], silver nanoparticles were synthesized and stabilized by chemical reduction method. The photoluminescent spectra of naphthalene oil wasstudied before and after the introduction of silver nanoparticles into naphthalene oil. An analysis of the photoluminescent spectra of naphthalene oil before and after the introduction of silver nanoparticles shows that after the introduction of silver nanoparticles, the intensities of the luminescence peaks belonging to the oil decrease sharply and new peaks belonging to silver nanoparticles appear.

Currently, research is ongoing in the field of the influence of nanoparticles on therapeutic naphthalene oil, including optical, antimicrobial, luminescent and other physicochemical properties. It is assumed that the introduction of metal nanoparticles, including silver, into the composition of medical naphthalene oil along with antibacterial and antiseptic properties, can give medicalnaphthalene oil additional properties.

2. CONCLUSION

The article haspresented a brief overview of studies on the current state of the study of the chemical composition of oil in the Naphthalene field and identifies the main areas of application of therapeutic Naphthalene oil. It is shown that a distinctive feature of the composition of medicalnaphthalene oil is the presence of a significant amount of hydrated saturated cyclic hydrocarbons, including decahydronaphtha-lenes, in contrast to fuel oil. It has been established that the therapeutic effect of naphthalene oil causes not onlyone type of hydrocarbon, but a combination of various naphthenic compounds contained in the oil, which can include both steranic and triterpenichydrocarbons, as well as bridged hydrocarbons of the articulation type. The possibility of using nanotechnology to vary the physicochemical properties, including the optical, antibacterial, antiseptic and other properties of naphthalene oil was studied.

3. REFERENCES

1. Adigezalova V.A., Gashimova U.F., Babaev H.F., Shukyurova P.A./ On the perspective of research of biological effects of natural medicalfactors, History of Science and Technology, №1, 2017, p.52-56

2. Mamedaliev Yu.G. / On the chemical composition of the active therapeutic Naftalan oil . Izvestiya AN Azerb. SSR, 1953, № 5, p.14–17

3. Musayev I.A., Ushakova I.B., Kurashova E.KH., Zaikin V.G., Yermakova L.S., Gelekh L.S., Mekhtiyev M.A, Gadzhiyev G.S, Sanin P.I. / About the chemical composition of naphthalenee oil. Neftekhimiya, 1980, №. 1, p. 14–20

4. Musaev I.A, Zaikin V.G, Kurashova E.Kh, Bagriy E.I, Ermakova L.S, Sanin P.I. / Tricyclic saturated hydrocarbons of Naftalan oil. Neftekhimiya, 1982, vol. 22, №. 2, p.18 .

5. Karaev A.I, Aliev R.K, Babaev A.Z /Naphthalene oil, its biological action and medicalapplication. M .: Izd-vo AN SSSR. 1959. p. 7–13.

6. Talybly A.G., Adigezalova V.A. / Research of ecosystems of medicaloil Naphthalene field as a medium for living microorganisms Chemical technologies and products, №4, 2018, p.22-26

7. Shevtsova A.S, Pogrebnyak L.V /Analysis of critical points of obtaining cream-balm with natural naphthalene oil, Health and Education Millennium, 2017, vol. 19. № 10, p.363-366

8. Babaev F.R., Martynova G.S., Maksakova O.P., Nanadzhanova R.G./ Oil fields Naftalan geology of oil and gas, № 5, 2018, p.87-93.

9. Samedova F.I/ Oil of Azerbaijan. - Baku: Elm, 2011. - 412 p.

10. Kuliyev A.M., Levshina A.M., Shepeleva T.V./ Dokl. AN Azerb. SSR. 1980, №. 10, p. 50–53

11. Kuliyev A.M., Petrov A.A., Levshina A.M. and etc.Azerbaijan Chemical Journal, 1984, №. 2, p. 48.

12. Guliyev I.S, Huseynov D.A, Martynova GS and others. Study of nanodispersity of naphthalene oil / East European Scientific Journal, 2017, № 3(19), p.90–98.

13. Babaev F.R, Martynova G.S, Maksakova O.P and others./ Features of Naftalan oil fields // Geology of oil and gas. –2017, № 2, p.71–75.

14. Babaev F.R., Martynova G.S., Mamedova S.G. et al. On the composition of the unique oil of the Naftalan field // Geology, geophysics and development of oil and gas fields. - 2015. - №. 3, p.36–42.

15. Adigezalova V.A./ Study of saturated hydrocarbons of naphthalene oil and the possibility of their use, Chemical Technologies

and Products of Oil and Gas Chemistry, p. 24-27

16. Kuliyev A.M, Buzova N.G., Muradov A.N. and etal./Study of naphthenic hydrocarbons of naphthalene oil Abstract rep. of Republican Conference "Chemistry and technology of additives to oils, fuels and cutting fluids", Baku: Institute of Chemistry of the Azerbaijan Academy of Sciences, 1978, p. 94.

17. Shakhtakhtinskiy T.N., Zeynalov E.B., Mamedova Kh.A., Aliyeva N.I./ Dokl. AN SSSR. 1991,vol. 317, №. 3, p. 658–660.

18. Adigezalova V.A. /Unique oil of naphthalene field of Azerbaijan Journal of history of science and technology, p.52-55.

19. Yakubov F.I., Asrieva T.S./ About the bactericidal properties of raw Naftalan. Baku, Broshyura Publ., 1934.

20. Rozenbaum F.G./ Protokol kavkazskogo meditsinskogo obshchestva [Minutes of Caucasian MedicalSociety]. 1987, No.2.

21. Aliev N.D. /Naftalan oil impact on antitoxic immunity development process Reports of 2nd Republican scientific session on Naftalan problems, Baku, 1955, p. 53–54.

22. Meshcherskiy G.I. /Naftalan in dermatology. Sovetskiy vestnik dermatologii, 1931, №5–6.

23. Mirzadzhanzade A.Kh., Magerramov A.M., Yusifzade H.B., Shabanov A.L., Nagiyev F.B., Mamedzade R.B., Ramazanov M.A./ Studying the influence of iron and aluminum nanoparticles the process of increasing the intensity of gas evolution and pressure for use in oil production, Izvestiya BSU, №. 1, 2005, p. 5-13.

24. Gozalova N., Ramazanov M.A, Hajiyeva F.V / The effect of silver nanoparticles on the photoluminescent properties of naphthalene oil, Proceedings of the scientific conference "Scientists of the Future" dedicated to the 97th anniversary of National Leader Heydar Aliyev, 12-13 May, 2020.

INFLUNCE OF PROTONS POLARIZATION TO CROSS-SECTION OF NEUTRALINO PRODUCTION AT COLLISION PROTONS AT HIGH ENERGIES WITH PARTICIPATION THE Z^0 BOSON AND SCALAR QUARKS

M.R.ALIZADA, A.I.AHMADOV

Baku State University, Department of Theoretical Physics, Baku, Azerbaijan

Cross-section of neutralino pair production in a proton-proton collision is study at the high energies with participation the Z^0 virtual boson, scalar quarks (t, u) and cross processes $(t - u, t - s, u - s)$. Calculation of cross-section of processes is also carried out via considering unpolarized and polarized protons. Also, the dependence cross-section of the process is defined in the polarization order of protons. Coefficient of asymmetry of processes is investigated as well.

1. INTRODUCTION

At p-p collisions with high energy in the Large Hadron Collider (LHC) are produced many particles: hadrons, heavy particle - for example, the Z boson, which then splits into two quarks, other particles with high energy - electrons, muons, and photons. The study of particle production in p-p collision is presented significant theoretical and experimental interest [1-4]. The search of supersymmetric particles is one of the main tasks of the theoretical and particles predicted by supersymmetry. The lightest neutralino is the main candidate for cold dark matter components. Thus, investigation of the production of the lightest neutralino to give information about the nature of dark matter [13-15].

At early we investigated cross-section neutralino production at p-p collision with participation γ photon [16,17]. The proton collision process will consider in the following subprocess
$q(p_1)\overline{q}(p_2) \to \tilde{\chi}_i^0(k_1)\tilde{\chi}_j^0(k_2);$ $(i, j = 1,2,3,4)$. Expressions of cross-section of process collision obtained without and with take into account polarization of protons.

2. THE CROSS-SECTION OF NEUTRALINO PRODUCTION AT P-P COLLISION AT HIGH ENERGIES
2.1 THE CROSS-SECTION OF PROCESSES WITH PARTICIPATION THE Z^0 BOSON AND SCALAR QUARKS

At early we obtained expression for cross-section of process of neutralino production at proton-proton experimental investigations, in example at hadron colliders - LHC.

The minimal supersymmetric standard model (MSSM) is one of the well-studied extensions of the standard model (SM). MSSM predicts many new particles: Sleptons, Squarks, gluinos, light/heavy neutral scalar Higgs bosons, four neutralinos, and two charginos [5-7].

Spin is one of the most fundamental properties of elementary particles. The spin-orbit interaction also affects scattering processes. [8-12].

Neutraliino is one of the hypothetical collision at high energy for following subprocess $q(p_1)\overline{q}(p_2) \to \tilde{\chi}_i^0(k_1)\tilde{\chi}_j^0(k_2)$ [16,17]:

$$\sigma_\gamma = \frac{\lambda_{ij}}{288\pi s^2}|M_\gamma|^2 \text{ where}$$

$$\lambda_{ij} = \frac{\sqrt{\left(s - m_{\tilde{\chi}_i^0}^2 - m_{\tilde{\chi}_j^0}^2\right)^2 - 4m_{\tilde{\chi}_i^0}^2 m_{\tilde{\chi}_j^0}^2}}{2}$$

The full square of the module of invariant amplitude will be found as follows:

$$\overline{|M|}^2 = (M_t + M_u + M_s)(M_t^+ + M_u^+ + M_s^+) =$$
$$= |M_t|^2 + |M_t|^2 + |M_t|^2 + 2M_t M_u^+ + 2M_t M_s^+ + 2M_u M_s^+$$

a) process with no polarized protons

The amplitude of the process with participation the Z^0 boson is recorded using Feynman's rules:

$$M_Z = \frac{ig^2}{2\cos^2\theta_w(\hat{s} - m_z^2)}\overline{u}(k_1)\gamma^\mu\left[O_Z^{ij}P_L - O_Z^{ij*}P_R\right]\times$$
$$\times \upsilon(k_2)\overline{\upsilon}(p_2)\gamma_\nu\left[a_{Z_q}^s + a_{Z_q}^L P_L\right]u(p_1) \quad (1)$$

where $P_{R,L} = \frac{(1 \pm \gamma_5)}{2}$; $a_{Z_q}^s = Q_q Sin^2\theta_w$;

$$a_{Z_q}^L = \frac{1}{2}(-1)^{T_q^3 + \frac{1}{2}}$$

The Hermitian conjugacy of the amplitude has the following form

$$M_Z^+ = \frac{-ig^2}{2\cos^2\theta_w(\hat{s}-m_z^2)}\overline{v}(k_2)\left[O_Z^{ij*}P_R - O_Z^{ij}P_L\right]\times$$
$$\times \gamma_\mu u(k_1)\overline{u}(p_1)\left[a_{Z_q}^s + a_{Z_q}^L P_R\right]\gamma_v v(p_2) \qquad (2)$$

We use the spin ratio from the Dirac equation and given that at high energies $E \gg m$ the particles can be considered massless ($m_1 = 0; m_2 = 0$), then for the square of the matrix element receive:

$$|M_Z|^2 = \frac{g^4}{16\cos^4\theta_w(\hat{s}-m_z^2)^2}\times$$
$$\times Tr\left[\gamma^\mu\left[O_Z^{ij}P_L - O_Z^{ij*}P_R\right]\left[\hat{k}_2 - m_{\tilde{\chi}_j^0}\right]\left[O_Z^{ij*}P_R - O_Z^{ij}P_L\right]\gamma_{\mu'}\left(\hat{k}_1 + m_{\tilde{\chi}_i^0}\right)\right]\times$$
$$\times Tr\left[\gamma^\mu\left[a_{Z_q}^s + a_{Z_q}^L P_L\right]\hat{p}_1\left[a_{Z_q}^s + a_{Z_q}^L P_R\right]\gamma_{\mu'}\hat{p}_2\right]$$

In the last expression, we express the particle momentum using Mandelstam invariants and constants $a_{Z_q}^s$ and

$a_{Z_q}^L$ can be expressed using vectors g_A and g_V:

$a_{Z_q}^s = g_V + g_A$, $a_{Z_q}^L = -2g_A$. As a result we get an expression for the square of the matrix element we get the following

$$|M_Z|^2 = \frac{g^4}{2\cos^4\theta_w(\hat{s}-m_z^2)^2}(g_V^2 + g_A^2)\times$$
$$\times\left[O_Z^{ij}O_Z^{ij*}\left[(m_{\tilde{\chi}_j^0}^2 - \hat{u})(m_{\tilde{\chi}_i^0}^2 - \hat{u}) + (m_{\tilde{\chi}_j^0}^2 - \hat{t})(m_{\tilde{\chi}_i^0}^2 - \hat{t})\right] - \qquad (3)$$
$$- m_{\tilde{\chi}_i^0}m_{\tilde{\chi}_j^0}\hat{s}\left(O_Z^{ij2} + O_Z^{ij*2}\right)\right]$$

b) process with polarized protons

The amplitude and its Hermitian conjugacy of the process with participation the Z^0 boson will be similar (1,2). Calculate the square of the matrix element:

$$|M_Z|^2 = M_Z M_Z^+ = \frac{g^4}{4\cos^4\theta_w(\hat{s}-m_z^2)^2}\times$$
$$\times\overline{u}(k_1)\gamma^\mu\left[O_Z^{ij}P_L - O_Z^{ij*}P_R\right]v(k_2)\overline{v}(p_2,s_2)\gamma_v\times$$
$$\times\left[a_{Z_q}^s + a_{Z_q}^L P_L\right]u(p_1,s_1)\overline{v}(k_2)\left[O_Z^{ij*}P_R - O_Z^{ij}P_L\right]\times$$
$$\times\gamma_\mu u(k_1)\overline{u}(p_1,s_1)\left[a_{Z_q}^s + a_{Z_q}^L P_R\right]\gamma_v v(p_2,s_2)$$

We use the spin ratio from the Dirac equation and simplify the expression after opening the brackets:

$$|M_Z|^2 = \frac{g^4}{2\cos^4\theta_w(\hat{s}-m_z^2)^2}(g_V^2 + g_A^2)\times$$
$$\times\left[O_Z^{ij}O_Z^{ij*}\left(\left(m_{\tilde{\chi}_j^0}^2 - \hat{u}\right)\left(m_{\tilde{\chi}_i^0}^2 - \hat{u}\right) + \right.\right.$$
$$\left.+ \left(m_{\tilde{\chi}_j^0}^2 - \hat{t}\right)\left(m_{\tilde{\chi}_i^0}^2 - \hat{t}\right)\right) - m_{\tilde{\chi}_j^0}m_{\tilde{\chi}_i^0}\hat{s}\times \qquad (4)$$
$$\times\left(O_Z^{ij} + O_Z^{ij*}\right)\right](1 - \lambda_1\lambda_2)$$

2.2 THE CROSS-SECTION OF PROCESSES WITH PARTICIPATION THE SCALAR t QUARK

a) process with no polarized protons

Let's write the amplitude of the process:

$$M_t = \frac{-2ig^2}{t - m_{\tilde{q}_k}^2}\overline{u}(k_1)\left(a_{q_{k_i}}^{L*}P_R + a_{q_{k_i}}^{R*}P_L\right)\times$$
$$\times u(p_1)\overline{v}(p_2)\left(a_{q_{k_j}}^L P_L + a_{q_{k_j}}^R P_R\right)v(k_2) \qquad (5)$$

Hermitian conjugate of the amplitude (5):

$$M_t^+ = \frac{2ig^2}{t - m_{\tilde{q}_{k'}}^2}\overline{u}(p_1)\left(a_{q_{k_i}}^L P_L + a_{q_{k_i}}^R P_R\right)\times$$
$$\times u(k_1)\overline{v}(k_2)\left(a_{q_{k_j}}^{L*}P_R + a_{q_{k_j}}^{R*}P_L\right)v(p_2) \qquad (6)$$

Using the properties of Dirac matrices, considering that for large values of proton energy, the quark masses can be neglected and expressing particle momentum using Mandelstam invariants, we obtain an expression for the square of the modulus of the invariant amplitude

$$\overline{|M_t|}^2 = \frac{g^4}{(\hat{t} - m_{\tilde{q}_k}^2)(\hat{t} - m_{\tilde{q}_{k'}}^2)}\left(a_{q_{k_i}}^{L*}a_{q_{k_i'}}^L + a_{q_{k_i}}^{R*}a_{q_{k_i'}}^R\right)\times$$
$$\times\left(a_{q_{k_j}}^L a_{q_{k_j'}}^{L*} + a_{q_{k_j}}^R a_{q_{k_j'}}^{R*}\right)\left(m_{\tilde{\chi}_i^0}^2 - \hat{t}\right)\left(m_{\tilde{\chi}_j^0}^2 - \hat{t}\right) \qquad (7)$$

b) process with polarized protons

The amplitude and its Hermitian conjugate of the process will be similar to (5) and (6), respectively. The squared modulus of the invariant amplitude:

$$\overline{\left|M_t\right|}^2 = M_t M_t^+ = \frac{4g^4}{\left(\hat{t}-m_{\tilde{q}_k}^2\right)\left(\hat{t}-m_{\tilde{q}_{k'}}^2\right)}\left[\bar{u}(k_1)\times\right.$$

$$\times\left(a_{q_{k_i}}^{L*}P_R + a_{q_{k_i}}^{R*}P_L\right)u(p_1)\bar{\upsilon}(p_2)\left(a_{q_{k_j}}^{L}P_L + a_{q_{k_j}}^{R}P_R\right)\upsilon(k_2)\right]\times$$

$$\times\left[\bar{u}(p_1)\left(a_{q_{k_i'}}^{L}P_L + a_{q_{k_i'}}^{R}P_R\right)u(k_1)\bar{\upsilon}(k_2)\times\right.$$

$$\times\left.\left(a_{q_{k_j'}}^{L*}P_R + a_{q_{k_j'}}^{R*}P_L\right)\upsilon(p_2)\right]$$

Dirac matrices properties is used, considering that, for large values of proton energy, the masses of quarks can be neglected and express the particle momentum using Mandelstam invariants we get an expression for the square of the modulus of the invariant amplitula:

$$\overline{\left|M_t\right|}^2 = \frac{g^4}{\left(\hat{t}-m_{\tilde{q}_k}^2\right)\left(\hat{t}-m_{\tilde{q}_{k'}}^2\right)}\left[a_{q_{k_i}}^{L*}a_{q_{k_i}}^{L}\left(1-\lambda_1\right)+a_{q_{k_i}}^{R*}a_{q_{k_i}}^{R}\left(1+\lambda_1\right)\right]\times$$

$$\times\left[a_{q_{k_j}}^{L}a_{q_{k_j}}^{L*}\left(1+\lambda_2\right)+a_{q_{k_j}}^{R}a_{q_{k_j}}^{R*}\left(1-\lambda_2\right)\right]\left(m_{\tilde{\chi}_i^0}^2-\hat{t}\right)\left(m_{\tilde{\chi}_j^0}^2-\hat{t}\right) \qquad (8)$$

The last formula for $\lambda_1 = \lambda_2 = 0$ coincides with the formula obtained without taking into account the polarization.

2.3 THE CROSS-SECTION OF PROCESSES WITH PARTICIPATION THE SCALAR u QUARK

a) process with no polarized protons

Matrix element of the process

$$M_u = (-1)^{\delta_{ij}}\frac{-2ig^2}{\hat{u}-m_{\tilde{q}_e}^2}\bar{u}(k_2)\left(a_{q_{e_j}}^{L*}P_R + a_{q_{e_j}}^{R*}P_L\right)\times$$

$$\times u(p_1)\bar{\upsilon}(p_2)\left(a_{q_{e_i}}^{L}P_L + a_{q_{e_i}}^{R}P_R\right)\upsilon(k_1) \qquad (9)$$

Hermitian conjugate of a matrix element (9):

$$M_u^+ = (-1)^{\delta_{ij}}\frac{2ig^2}{\hat{u}-m_{\tilde{q}_e}^2}\bar{u}(p_1)\left(a_{q_{e'_j}}^{L}P_L + a_{q_{e'_j}}^{R}P_R\right)\times$$

$$\times u(k_2)\bar{\upsilon}(k_1)\left(a_{q_{e'_i}}^{L*}P_R + a_{q_{e'_i}}^{R*}P_L\right)\upsilon(p_2) \qquad (10)$$

Using the properties of Dirac matrices, taking into account that for large values of proton energy, the masses of quarks can be ignored, express the particle momentum in terms of the Mandelstam invariants and obtain expression for the square of the modulus of the invariant amplitude:

$$\overline{\left|M_u\right|}^2 = \frac{g^4}{\left(\hat{u}-m_{\tilde{q}_e}^2\right)\left(\hat{u}-m_{\tilde{q}_{e'}}^2\right)}\left(a_{q_{e_j}}^{L*}a_{q_{e'_j}}^{L} + a_{q_{e_j}}^{R*}a_{q_{e'_j}}^{R}\right)\times$$

$$\times\left(a_{q_{e_i}}^{L}a_{q_{e'_i}}^{L*} + a_{q_{e_i}}^{R}a_{q_{e'_i}}^{R*}\right)\left(m_{\tilde{\chi}_i^0}^2-\hat{u}\right)\left(m_{\tilde{\chi}_j^0}^2-\hat{u}\right) \qquad (11)$$

b) process with polarized protons

We use the expression of the matrix element and the Hermitian conjugate process.

$$\overline{\left|M_u\right|}^2 = M_u M_u^+ = (-1)^{\delta_{ij}}\frac{-2ig^2}{\hat{u}-m_{\tilde{q}_e}^2}\bar{u}(k_2)\left(a_{q_{e_j}}^{L*}P_R + a_{q_{e_j}}^{R*}P_L\right)\times$$

$$\times u(p_1)\bar{\upsilon}(p_2)\left(a_{q_{e_i}}^{L}P_L + a_{q_{e_i}}^{R}P_R\right)\upsilon(k_1)(-1)^{\delta_{ij}}\frac{2ig^2}{\hat{u}-m_{\tilde{q}_{e'}}^2}\bar{u}(p_1)\times$$

$$\times\left(a_{q_{e'_j}}^{L}P_L + a_{q_{e'_j}}^{R}P_R\right)u(k_2)\bar{\upsilon}(k_1)\left(a_{q_{e'_i}}^{L*}P_R + a_{q_{e'_i}}^{R*}P_L\right)\upsilon(p_2)$$

Using the properties of Dirac matrices, taking into account that for large values of proton energy, the masses of quarks can be ignored, express the particle momentum in terms of the Mandelstam invariants and obtain expression for the square of the modulus of the invariant amplitude:

$$\overline{\left|M_u\right|}^2 = \frac{g^4}{\left(\hat{u}-m_{\tilde{q}_e}^2\right)\left(\hat{u}-m_{\tilde{q}_{e'}}^2\right)}\left(a_{q_{e_j}}^{L*}a_{q_{e'_j}}^{L}\left(1-\lambda_1\right)+\right.$$

$$+a_{q_{e_j}}^{R*}a_{q_{e'_j}}^{R}\left(1+\lambda_1\right)\left(a_{q_{e_i}}^{L}a_{q_{e'_i}}^{L*}\left(1+\lambda_2\right)+\right.$$

$$\left.+a_{q_{e_i}}^{R}a_{q_{e'_i}}^{R*}\left(1-\lambda_2\right)\right)\left(m_{\tilde{\chi}_i^0}^2-\hat{u}\right)\left(m_{\tilde{\chi}_j^0}^2-\hat{u}\right) \qquad (12)$$

The last formula for $\lambda_1 = \lambda_2 = 0$ coincides with the formula obtained without taking into account the polarization.

2.4 THE CROSS-SECTION OF t-s CROSS-PROCESS

a) process with no polarized protons

Using the expressions (2) and (5) for the square of the modulus of invariant amplitude, we have:

$$M_t M_s^+ = \frac{-2ig^2}{t-m_{\tilde{q}_k}^2}\bar{u}(k_1)\left(a_{q_{k_i}}^{L*}P_R + a_{q_{k_i}}^{R*}P_L\right)u(p_1)\bar{\upsilon}(p_2)\times$$

$$\times\left(a_{q_{k_j}}^{L}P_L + a_{q_{k_j}}^{R}P_R\right)\upsilon(k_2)\frac{-ig^2}{2\cos^2\theta_w\left(\hat{s}-m_z^2\right)}\times$$

$$\times\bar{\upsilon}(k_2)\left[O_Z^{ij*}P_R - O_Z^{ij}P_L\right]\gamma^\mu u(k_1)\bar{u}(p_1)\times$$

$$\times\left[a_{Z_q}^{s} + a_{Z_q}^{L}P_R\right]\gamma_\nu\upsilon(p_2)g_{\mu\nu}$$

Using the relations of the destruction and birth operators from the Dirac equation: calculate the trace of the matrix and replace the particle momentum using the Mandelstam invariants. we obtain an expression for the square of the modulus of the invariant amplitude:

$$M_t M_s^+ = \frac{-g^4}{2\cos^2\theta_w\left(t-m_{\tilde{q}_k}^2\right)\left(\hat{s}-m_z^2\right)}\left\{\left(a_{Z_q}^{s}a_{q_{k_i}}^{L}a_{q_{k_j}}^{L*}O_Z^{ij}+\right.\right.$$

$$+\left(a_{Z_q}^{s} + a_{Z_q}^{L}\right)a_{q_{k_i}}^{R}a_{q_{k_j}}^{R*}O_Z^{ij*}\left(m_{\tilde{\chi}_i^0}^2-\hat{t}\right)\left(m_{\tilde{\chi}_j^0}^2-\hat{t}\right)+ \qquad (13)$$

$$+\left.\left(\left(a_{Z_q}^{s} + a_{Z_q}^{L}\right)a_{q_{k_i}}^{R}a_{q_{k_j}}^{R*}O_Z^{ij} - a_{Z_q}^{s}a_{q_{k_i}}^{L}a_{q_{k_j}}^{L*}O_Z^{ij*}\right)m_{\tilde{\chi}_i^0}m_{\tilde{\chi}_j^0}\hat{s}\right\}$$

b) process with polarized protons

Using the expressions (2) and (5) for the square of the modulus of invariant amplitude, we obtained:

$$M_t M_s^+ = \frac{-2ig^2}{t - m_{\tilde{q}_k}^2} \bar{u}(k_1)\left(a_{q_{k_i}}^{L*} P_R + a_{q_{k_i}}^{R*} P_L\right)u(p_1)\times$$

$$\times \bar{\upsilon}(p_2)\left(a_{q_{k_j}}^L P_L + a_{q_{k_j}}^R P_R\right)\upsilon(k_2)\frac{-ig^2}{2\cos^2\theta_w\left(\hat{s}-m_z^2\right)}\times$$

$$\times \bar{\upsilon}(k_2)\left[O_Z^{ij*} P_R - O_Z^{ij} P_L\right]\gamma^\mu u(k_1)\bar{u}(p_1)\times$$

$$\times\left[a_{Z_q}^s + a_{Z_q}^L P_R\right]\gamma_\nu \upsilon(p_2)g_{\mu\nu}$$

We used the relations of the destruction and birth operators from the Dirac equation: Calculate the trace of the matrix and replace the particle momentum using the Mandelstam invariants, simplify the expression and for the square of the modulus of invariant amplitude, we get:

$$M_t M_s^+ = \frac{-g^4}{2Cos^2\theta_w\left(\hat{t}-m_{\tilde{q}_k}^2\right)\left(\hat{s}-m_Z^2\right)}\left\{\left(a_{Z_q}^s a_{q_{k_i}}^L a_{q_{k_j}}^{L*} O_Z^{ij} + \left(a_{Z_q}^s + a_{Z_q}^L\right)\times\right.\right.$$

$$\times a_{q_{k_i}}^R a_{q_{k_j}}^{R*} O_Z^{ij*} + \lambda_1\left(a_{q_{k_j}}^R a_{q_{k_i}}^{L*} a_{Z_q}^s O_Z^{ij*} + a_{q_{k_j}}^L a_{q_{k_i}}^{R*} a_{Z_q}^s O_Z^{ij} + a_{q_{k_j}}^L a_{q_{k_i}}^{R*} a_{Z_q}^L O_Z^{ij}\right)+$$

$$+\lambda_2\left(a_{q_{k_j}}^R a_{q_{k_i}}^{R*} a_{Z_q}^s O_Z^{ij*} + a_{q_{k_j}}^R a_{q_{k_i}}^{R*} a_{Z_q}^L O_Z^{ij*} + a_{q_{k_i}}^{L*} a_{Z_q}^s a_{q_{k_j}}^L O_Z^{ij}\right)+$$

$$+\lambda_1\lambda_2\left(a_{q_{k_j}}^{R*} a_{q_{k_i}}^L a_{Z_q}^s O_Z^{ij} - a_{q_{k_j}}^R a_{q_{k_i}}^{L*} a_{Z_q}^s O_Z^{ij*} + a_{q_{k_j}}^L a_{q_{k_i}}^{R*} a_{Z_q}^L O_Z^{ij}\right)\right)\times$$

$$\times\left(m_{\tilde{\chi}_i^0}^2 - \hat{t}\right)\left(m_{\tilde{\chi}_j^0}^2 - \hat{t}\right) + \left(\left(a_{Z_q}^s + a_{Z_q}^L\right)a_{q_{k_i}}^R a_{q_{k_j}}^{R*} O_Z^{ij} - a_{Z_q}^s a_{q_{k_i}}^L a_{q_{k_j}}^{L*} O_Z^{ij*} +\right.$$

$$+\lambda_1\left(a_{q_{k_i}}^R a_{q_{k_j}}^{L*} a_{Z_q}^s O_Z^{ij*} + a_{q_{k_j}}^L a_{q_{k_i}}^{R*} a_{Z_q}^s O_Z^{ij} - a_{q_{k_i}}^{R*} a_{Z_q}^L a_{q_{k_j}}^L O_Z^{ij}\right)+$$

$$+\lambda_2\left(a_{q_{k_j}}^R a_{q_{k_i}}^{R*} a_{Z_q}^L O_Z^{ij} - a_{q_{k_j}}^R a_{q_{k_i}}^{R*} a_{Z_q}^s O_Z^{ij} + a_{q_{k_j}}^L a_{q_{k_i}}^{L*} a_{Z_q}^s O_Z^{ij}\right)+$$

$$+\lambda_1\lambda_2\left(a_{q_{k_j}}^L a_{q_{k_i}}^{R*} a_{Z_q}^s O_Z^{ij} - a_{q_{k_j}}^R a_{q_{k_i}}^{L*} a_{Z_q}^s O_Z^{ij*} + a_{q_{k_j}}^L a_{q_{k_i}}^{R*} a_{Z_q}^L O_Z^{ij}\right)\right)m_{\tilde{\chi}_i^0}m_{\tilde{\chi}_j^0}\hat{s}\right\}$$ (14)

As can be seen, the formula obtained by taking into account the polarization of colliding protons at $\lambda_1 = \lambda_2 = 0$ coincides with the formula obtained without taking into account the polarization.

2.5 THE CROSS-SECTION OF t-u CROSS-PROCESS

a) process with no polarized protons

Using the expressions (5) and (10) for the square of the modulus of invariant amplitude, we have:

$$M_t M_u^+ = \frac{-2ig^2}{\hat{t} - m_{\tilde{q}_k}^2}\bar{u}(k_1)\left(a_{q_{k_i}}^{L*} P_R + a_{q_{k_i}}^{R*} P_L\right)u(p_1)\times$$

$$\times \bar{\upsilon}(p_2)\left(a_{q_{k_j}}^L P_L + a_{q_{k_j}}^R P_R\right)\upsilon(k_2)(-1)^{\delta_{ij}}\frac{2ig^2}{\hat{u} - m_{\tilde{q}_e}^2}\times$$

$$\times \bar{u}(p_1)\left(a_{q_{e'j}}^L P_L + a_{q_{e'j}}^R P_R\right)u(k_2)\bar{\upsilon}(k_1)\times$$

$$\times\left(a_{q_{e'i}}^{L*} P_R + a_{q_{e'i}}^{R*} P_L\right)\upsilon(p_2)$$

Using the relations of the destruction and birth operators from the Dirac equation: in the last expression, express the particle momentum using Mandelstam invariants and get an expression for the square of the modulus of the invariant amplituda:

$$M_t M_u^+ = \frac{g^4}{\left(\hat{t}-m_{\tilde{q}_k}^2\right)\left(\hat{u}-m_{\tilde{q}_e}^2\right)}\left\{\frac{1}{2}\left[a_{q_{k_i}}^{L*} a_{q_{k_j}}^L a_{q_{e'j}}^R a_{q_{e'i}}^{R*} +\right.\right.$$

$$+ a_{q_{k_i}}^{R*} a_{q_{k_j}}^R a_{q_{e'j}}^L a_{q_{e'i}}^{L*}\right]\left(\left(m_{\tilde{\chi}_i^0}^2 - \hat{u}\right)\left(m_{\tilde{\chi}_i^0}^2 - \hat{u}\right)+\right.$$

$$+\left(m_{\tilde{\chi}_j^0}^2 - \hat{t}\right)\left(m_{\tilde{\chi}_i^0}^2 - \hat{t}\right) - \hat{s}\left(\hat{s} - m_{\tilde{\chi}_i^0}^2 - m_{\tilde{\chi}_j^0}^2\right)\right)+$$

$$+ m_{\tilde{\chi}_j^0}m_{\tilde{\chi}_i^0}\hat{s}\left[a_{q_{k_i}}^{L*} a_{q_{k_j}}^L a_{q_{e'j}}^L a_{q_{e'i}}^{L*} + a_{q_{k_i}}^{R*} a_{q_{k_j}}^R a_{q_{e'j}}^R a_{q_{e'i}}^{R*}\right]\right\}$$ (15)

b) process with polarized protons

Using the expressions (5) and (10) for the square of the modulus of invariant amplitude, we have

$$M_t M_u^+ = \frac{-2ig^2}{\hat{t} - m_{\tilde{q}_k}^2}\bar{u}(k_1)\left(a_{q_{k_i}}^{L*} P_R + a_{q_{k_i}}^{R*} P_L\right)u(p_1)$$

$$\times \bar{\upsilon}(p_2)\left(a_{q_{k_j}}^L P_L + a_{q_{k_j}}^R P_R\right)\upsilon(k_2)(-1)^{\delta_{ij}}\frac{2ig^2}{\hat{u} - m_{\tilde{q}_e}^2}\times$$

$$\times \bar{u}(p_1)\left(a_{q_{e_j}}^L P_L + a_{q_{e_j}}^R P_R\right)u(k_2)\bar{\upsilon}(k_1)\left(a_{q_{e_i}}^{L*} P_R + a_{q_{e_i}}^{R*} P_L\right)\upsilon(p_2)$$

Using the relations of the destruction and birth operators from the Dirac equation in the last expression, express the particle momentum using Mandelstam invariants and simplify it to obtain an following expression for the square of the modulus of the invariant amplituda:

$$M_t M_u^+ = \frac{g^4}{\left(\hat{t}-m_{\tilde{q}_k}^2\right)\left(\hat{u}-m_{\tilde{q}_e}^2\right)}\left\{\frac{1}{2}\left[a_{q_{k_i}}^{R*} a_{q_{k_j}}^R a_{q_{e_j}}^L a_{q_{e_i}}^{L*} + a_{q_{k_i}}^{L*} a_{q_{k_j}}^L a_{q_{e_j}}^R a_{q_{e_i}}^{R*} +\right.\right.$$

$$+\lambda_1\left(a_{q_{k_i}}^{R*} a_{q_{k_j}}^R a_{q_{e_j}}^R a_{q_{e_i}}^{R*} - a_{q_{k_i}}^L a_{q_{k_j}}^L a_{q_{e_j}}^L a_{q_{e_i}}^{L*}\right)+$$

$$+\lambda_2\left(a_{q_{k_i}}^{L*} a_{q_{k_j}}^L a_{q_{e_j}}^R a_{q_{e_i}}^{R*} - a_{q_{k_i}}^{R*} a_{q_{k_j}}^R a_{q_{e_j}}^L a_{q_{e_i}}^{L*}\right)-$$

$$-\lambda_1\lambda_2\left(a_{q_{k_i}}^{R*} a_{q_{k_j}}^R a_{q_{e_j}}^R a_{q_{e_i}}^{R*} - a_{q_{k_i}}^{L*} a_{q_{k_j}}^L a_{q_{e_j}}^L a_{q_{e_i}}^{L*}\right)\right]\times$$

$$\times\left(\left(m_{\tilde{\chi}_j^0}^2 - \hat{u}\right)\left(m_{\tilde{\chi}_i^0}^2 - \hat{u}\right)+\left(m_{\tilde{\chi}_i^0}^2 - \hat{t}\right)\left(m_{\tilde{\chi}_j^0}^2 - \hat{t}\right) - \hat{s}\left(\hat{s} - m_{\tilde{\chi}_i^0}^2 - m_{\tilde{\chi}_j^0}^2\right)\right)+$$

$$+ m_{\tilde{\chi}_i^0}m_{\tilde{\chi}_j^0}\hat{s}\left[a_{q_{k_i}}^{L*} a_{q_{k_j}}^L a_{q_{e_j}}^L a_{q_{e_i}}^{L*} + a_{q_{k_i}}^{R*} a_{q_{k_j}}^R a_{q_{e_j}}^R a_{q_{e_i}}^{R*} -\right.$$

$$-\lambda_1\left(a_{q_{k_i}}^{L*} a_{q_{k_j}}^L a_{q_{e_j}}^R a_{q_{e_i}}^{R*} + a_{q_{k_i}}^{R*} a_{q_{k_j}}^R a_{q_{e_j}}^L a_{q_{e_i}}^{L*}\right)-$$

$$-\lambda_2\left(a_{q_{k_i}}^{L*} a_{q_{k_j}}^L a_{q_{e_j}}^L a_{q_{e_i}}^{L*} + a_{q_{k_i}}^{R*} a_{q_{k_j}}^R a_{q_{e_j}}^R a_{q_{e_i}}^{R*}\right)-$$

$$-\lambda_1\lambda_2\left(a_{q_{k_i}}^{L*} a_{q_{k_j}}^L a_{q_{e_j}}^L a_{q_{e_i}}^{L*} - a_{q_{k_i}}^{L*} a_{q_{k_j}}^L a_{q_{e_j}}^R a_{q_{e_i}}^{R*}\right)\right]\right\}$$ (16)

The last formula for $\lambda_1 = \lambda_2 = 0$ coincides with the formula obtained without taking into account the polarization of colliding protons.

2.6 THE CROSS-SECTION OF s-u CROSS-PROCESS

a) process with no polarized protons

Using the expressions (2) and (9) for the square of the modulus of invariant amplitude, we have:

$$M_u M_s^+ = (-1)^{\delta_{ij}} \frac{-2ig^2}{\hat{u} - m_{\tilde{q}_e}^2} \bar{u}(k_2)\left(a_{q_{e_j}}^{L*} P_R + a_{q_{e_j}}^{R*} P_L\right) \times$$

$$u(p_1)\bar{\upsilon}(p_2)\left(a_{q_{e_i}}^L P_L + a_{q_{e_i}}^R P_R\right)\upsilon(k_1) \frac{-ig^2}{2\cos^2\theta_w(\hat{s} - m_z^2)} \times$$

$$\times \bar{\upsilon}(k_2)\left[O_Z^{ij*} P_R - O_Z^{ij} P_L\right]\gamma^\mu u(k_1)\bar{u}(p_1) \times$$

$$\times \left[a_{Z_q}^s + a_{Z_q}^L P_R\right]\gamma_\nu \upsilon(p_2)$$

Using the relations of the destruction and birth operators from the Dirac equation, calculate the trace of the square of the modulus of invariant amplitude:

$$M_u M_s^+ = \frac{-g^4}{2\cos^2\theta_w(\hat{s} - m_z^2)(\hat{u} - m_{\tilde{q}_e}^2)}\Big\{\Big(a_{Z_q}^s + a_{Z_q}^L\Big)a_{q_{e_j}}^{R*} a_{q_{e_i}}^R O_Z^{ij} -$$

$$- a_{q_{e_j}}^{L*} a_{q_{e_i}}^L a_{Z_q}^s O_Z^{ij*}\Big)\Big(m_{\tilde{\chi}_i^0}^2 - \hat{u}\Big)\Big(m_{\tilde{\chi}_j^0}^2 - \hat{u}\Big) + \qquad (17)$$

$$+ \Big(a_{Z_q}^s a_{q_{e_i}}^L a_{q_{e_j}}^{L*} O_Z^{ij} - \Big(a_{Z_q}^s + a_{Z_q}^L\Big)a_{q_{e_j}}^{R*} a_{q_{e_i}}^R O_Z^{ij*}\Big)m_{\tilde{\chi}_i^0} m_{\tilde{\chi}_j^0}\hat{s}\Big\}$$

b) process with polarized protons

Using the expressions (2) and (9) for the square of the modulus of invariant amplitude, obtained:

$$M_u M_s^+ = (-1)^{\delta_{ij}} \frac{-2ig^2}{\hat{u} - m_{\tilde{q}_e}^2} \bar{u}(k_2)\left(a_{q_{e_j}}^{L*} P_R + a_{q_{e_j}}^{R*} P_L\right) \times$$

$$\times u(p_1)\bar{\upsilon}(p_2)\left(a_{q_{e_i}}^L P_L + a_{q_{e_i}}^R P_R\right)\upsilon(k_1) \frac{-ig^2}{2\cos^2\theta_w(\hat{s} - m_z^2)} \times$$

$$\bar{\upsilon}(k_2)\left[O_Z^{ij*} P_R - O_Z^{ij} P_L\right]\gamma^\mu u(k_1)\bar{u}(p_1) \times$$

$$\times \left[a_{Z_q}^s + a_{Z_q}^L P_R\right]\gamma_\nu \upsilon(p_2)$$

Using the relations of the destruction and birth operators from the Dirac equation, calculate the trace of the square of the modulus of invariant amplitude, express the particle in momentum using Mandelstam invariants and take the general multipliers out of brackets

$$M_u M_s^+ = \frac{-g^4}{2Cos^2\theta_w(\hat{s} - m_Z^2)(\hat{u} - m_{\tilde{q}_e}^2)}\Big[\Big(\Big(a_{Z_q}^s + a_{Z_q}^L\Big)a_{q_{e_j}}^{R*} a_{q_{e_i}}^R O_Z^{ij} - a_{q_{e_j}}^{L*} a_{q_{e_i}}^L \times$$

$$\times a_{Z_q}^s O_Z^{ij*} + \lambda_1\Big(a_{q_{e_j}}^{R*} a_{q_{e_i}}^R a_{Z_q}^s O_Z^{ij*} + a_{q_{e_j}}^{R*} a_{q_{e_i}}^R a_{Z_q}^L O_Z^{ij*} + a_{q_{e_j}}^{L*} a_{q_{e_i}}^L a_{Z_q}^s O_Z^{ij}\Big) +$$

$$+ \lambda_2\Big(a_{q_{e_j}}^{L*} a_{q_{e_i}}^L a_{Z_q}^s O_Z^{ij*} + a_{q_{e_j}}^{R*} a_{q_{e_i}}^R a_{Z_q}^s O_Z^{ij} + a_{q_{e_j}}^{R*} a_{q_{e_i}}^R a_{Z_q}^L O_Z^{ij}\Big) +$$

$$+ \lambda_1\lambda_2\Big(a_{q_{e_j}}^{R*} a_{q_{e_i}}^R a_{Z_q}^s O_Z^{ij*} + a_{q_{e_j}}^{R*} a_{q_{e_i}}^R a_{Z_q}^L O_Z^{ij} + a_{q_{e_j}}^{L*} a_{q_{e_i}}^L a_{Z_q}^s O_Z^{ij}\Big)\Big) \times$$

$$\Big(m_{\tilde{\chi}_i^0}^2 - \hat{u}\Big)\Big(m_{\tilde{\chi}_j^0}^2 - \hat{u}\Big) + \Big\{a_{Z_q}^s a_{q_{e_i}}^L a_{q_{e_j}}^{L*} O_Z^{ij} - \Big(a_{Z_q}^s + a_{Z_q}^L\Big)a_{q_{e_j}}^{R*} a_{q_{e_i}}^R O_Z^{ij*} - \qquad (18)$$

$$- \lambda_1\Big(a_{q_{e_j}}^{L*} a_{q_{e_i}}^L a_{Z_q}^s O_Z^{ij*} + a_{q_{e_j}}^{R*} a_{q_{e_i}}^R a_{Z_q}^s O_Z^{ij} + a_{q_{e_j}}^{R*} a_{q_{e_i}}^R a_{Z_q}^L O_Z^{ij}\Big) -$$

$$- \lambda_2\Big(a_{q_{e_j}}^{R*} a_{q_{e_i}}^R a_{Z_q}^s O_Z^{ij*} + a_{q_{e_j}}^{R*} a_{q_{e_i}}^R a_{Z_q}^L O_Z^{ij*} + a_{q_{e_j}}^{L*} a_{q_{e_i}}^L a_{Z_q}^s O_Z^{ij}\Big) +$$

$$+ \lambda_1\lambda_2\Big(a_{q_{e_j}}^{L*} a_{q_{e_i}}^L a_{Z_q}^s O_Z^{ij*} - a_{q_{e_j}}^{R*} a_{q_{e_i}}^R a_{Z_q}^s O_Z^{ij} - a_{q_{e_j}}^{R*} a_{q_{e_i}}^R a_{Z_q}^L O\Big)_Z^{ij}\Big\} \times$$

$$\times m_{\tilde{\chi}_i^0} m_{\tilde{\chi}_j^0}\hat{s}\Big]$$

As can be seen from the last formula for $\lambda_1 = \lambda_2 = 0$ it coincides with the formula obtained without taking into account the polarization.

Thus as show obtained formulas, the effective cross-section of the collision process with polarized protons with the with participation of γ photon and the Z^0 boson depends on the product of the polarization degrees $(\lambda_1\lambda_2)$, and with the with participation scalar quarks it depends on the polarization degree of individual proton beams (λ_1 and λ_2) and their product $(\lambda_1\lambda_2)$.

3. THE COEFFICIENT ASYMMETRY OF CROSS PROCESSES OF NEUTRALINO PRODUCTION AT P-P COLLISION AT HIGH ENERGIES

3.1 THE COEFFICIENT ASYMMETRY OF t - s CROSS PROCESS

To simplify the expression (14), enter the following notation:

$$A = \frac{-g^4}{2Cos^2\theta_w(\hat{t} - m_{\tilde{q}_k}^2)(\hat{s} - m_Z^2)},$$

$$B_1 = a_{Z_q}^s a_{q_{k_i}}^L a_{q_{k_j}}^{L*} O_Z^{ij} + \Big(a_{Z_q}^s + a_{Z_q}^L\Big)a_{q_{k_i}}^R a_{q_{k_j}}^{R*} O_Z^{ij*},$$

$$C_1 = a_{q_{k_j}}^R a_{q_{k_i}}^{L*} a_{Z_q}^s O_Z^{ij*} + a_{q_{k_j}}^L a_{q_{k_i}}^{R*} a_{Z_q}^s O_Z^{ij} + a_{q_{k_j}}^L a_{q_{k_i}}^{R*} a_{Z_q}^L O_Z^{ij},$$

$$D_1 = a_{q_{k_j}}^R a_{q_{k_i}}^{R*} a_{Z_q}^s O_Z^{ij*} + a_{q_{k_j}}^R a_{q_{k_i}}^{R*} a_{Z_q}^L O_Z^{ij*} + a_{q_{k_i}}^{L*} a_{Z_q}^s a_{q_{k_j}}^L O_Z^{ij},$$

$$E_1 = a_{q_{k_i}}^{R*} a_{q_{k_i}}^L a_{Z_q}^s O_Z^{ij} - a_{q_{k_i}}^R a_{q_{k_i}}^{L*} a_{Z_q}^s O_Z^{ij*} + a_{q_{k_j}}^L a_{q_{k_i}}^{R*} a_{Z_q}^L O_Z^{ij},$$

$$F_1 = \Big(m_{\tilde{\chi}_i^0}^2 - \hat{t}\Big)\Big(m_{\tilde{\chi}_j^0}^2 - \hat{t}\Big),$$

$$B_2 = \Big(a_{Z_q}^s + a_{Z_q}^L\Big)a_{q_{k_i}}^R a_{q_{k_j}}^{R*} O_Z^{ij} - a_{Z_q}^s a_{q_{k_i}}^L a_{q_{k_j}}^{L*} O_Z^{ij*},$$

$$C_2 = a_{q_{k_j}}^R a_{q_{k_i}}^{L*} a_{Z_q}^s O_Z^{ij*} + a_{q_{k_j}}^L a_{q_{k_i}}^{R*} a_{Z_q}^s O_Z^{ij} - a_{q_{k_j}}^{R*} a_{Z_q}^L a_{q_{k_i}}^L O_Z^{ij},$$

$$D_2 = a_{q_{k_j}}^R a_{q_{k_i}}^{R*} a_{Z_q}^L O_Z^{ij} - a_{q_{k_j}}^R a_{q_{k_i}}^{R*} a_{Z_q}^s O_Z^{ij} + a_{q_{k_j}}^L a_{q_{k_i}}^{L*} a_{Z_q}^s O_Z^{ij},$$

$$E_2 = a_{q_{k_j}}^L a_{q_{k_i}}^{R*} a_{Z_q}^s O_Z^{ij} - a_{q_{k_j}}^R a_{q_{k_i}}^{L*} a_{Z_q}^s O_Z^{ij*} + a_{q_{k_j}}^L a_{q_{k_i}}^{R*} a_{Z_q}^L O_Z^{ij},$$

$$F_2 = m_{\tilde{\chi}_i^0} m_{\tilde{\chi}_j^0}\hat{s}$$

We use these notations and for the square of the modulus of the invariant amplitude of the cross process t - s we get the following expression

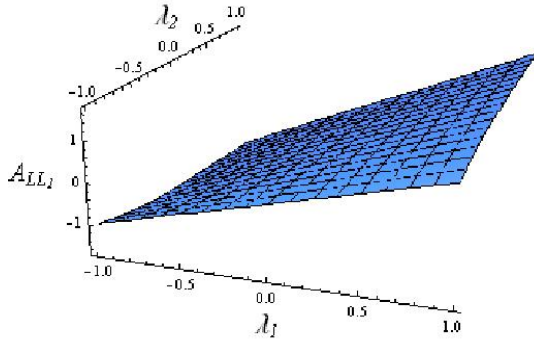$$M_t M_s^+ = A\big[(B_1 + C_1\lambda_1 + D_1\lambda_2 + E_1\lambda_1\lambda_2)F_1$$

$$+ (B_2 + C_2\lambda_1 + D_2\lambda_2 + E_2\lambda_1\lambda_2)F_2\big]$$

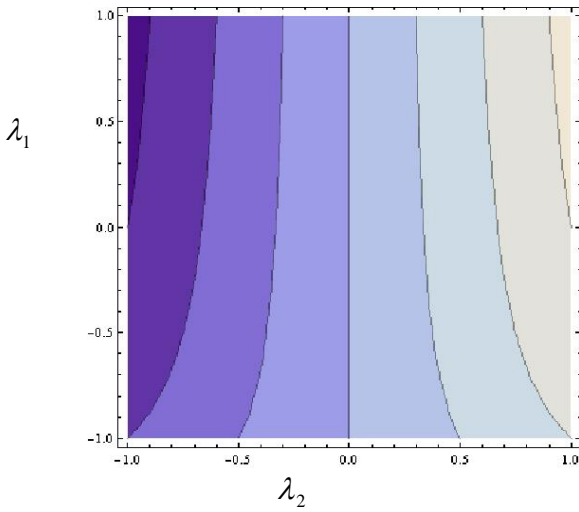Accordingly the coefficients of asymmetry in these notations will be written as follows:

$$A_{LL}(-\lambda_1, \lambda_2) = \frac{\lambda_1(C_1F_1 + D_1F_1 + C_2F_2 + E_1F_1\lambda_2 + E_2F_2\lambda_2)}{B_1F_1 + F_2(B_2 + D_2\lambda_2)}$$

$$A_{LL}(\lambda_1, -\lambda_2) = \frac{(D_2F_2 + E_1F_1\lambda_1 + E_2F_2\lambda_1)\lambda_2}{B_1F_1 + (C_1 + D_1)F_1\lambda_1 + F_2(B_2 + C_2\lambda_1)}$$

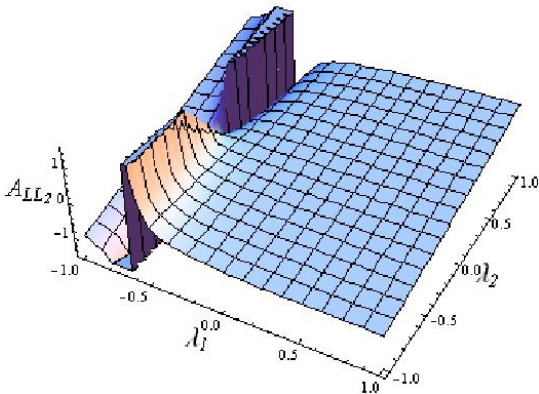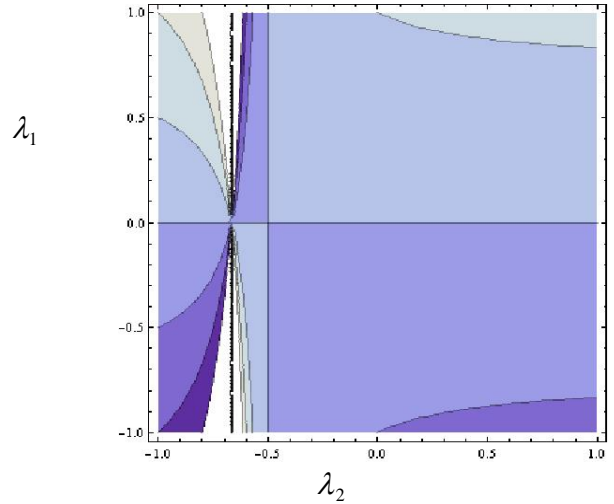Fig.1 shows the dependence $A_{LL}(-\lambda_1, \lambda_2)$ and its counter-dependency.

a

b

Figure 1. The dependence $A_{LL}(-\lambda_1, \lambda_2)$ (a) and its counter-plot dependence (b)

Fig.2 shows the dependence $A_{LL}(\lambda_1, -\lambda_2)$ and its counter-dependency.

a

b

Figure 2. The dependence $A_{LL}(\lambda_1, -\lambda_2)$ (*a*) and its counter plot-dependency (*b*)

3.2 THE COEFFICIENT ASYMMETRY OF t - u CROSS PROCESS

To simplify the expression (16), enter the following notation:

$$A = \frac{g^4}{\left(\hat{t} - m_{\tilde{q}_k}^2\right)\left(\hat{u} - m_{\tilde{q}_e}^2\right)},$$

$$B_1 = a_{q_{k_i}}^{R*} a_{q_{k_j}}^{R} a_{q_{e_j}}^{L} a_{q_{e_i}}^{L*} + a_{q_{k_i}}^{L*} a_{q_{k_j}}^{L} a_{q_{e_j}}^{R} a_{q_{e_i}}^{R*},$$

$$C_1 = a_{q_{k_i}}^{R*} a_{q_{k_j}}^{R} a_{q_{e_j}}^{R} a_{q_{e_i}}^{R*} - a_{q_{k_i}}^{L*} a_{q_{k_j}}^{L} a_{q_{e_j}}^{L} a_{q_{e_i}}^{L*}$$

$$D_1 = a_{q_{k_i}}^{L*} a_{q_{k_j}}^{L} a_{q_{e_j}}^{R} a_{q_{e_i}}^{R*} - a_{q_{k_i}}^{R*} a_{q_{k_j}}^{R} a_{q_{e_j}}^{L} a_{q_{e_i}}^{L*}$$

$$E_1 = a_{q_{k_i}}^{R*} a_{q_{k_j}}^{R} a_{q_{e_j}}^{R} a_{q_{e_i}}^{R*} - a_{q_{k_i}}^{L*} a_{q_{k_j}}^{L} a_{q_{e_j}}^{L} a_{q_{e_i}}^{L*}$$

$$C_2 = a_{q_{k_i}}^{L*} a_{q_{k_j}}^{L} a_{q_{e_j}}^{R} a_{q_{e_i}}^{R*} + a_{q_{k_i}}^{R*} a_{q_{k_j}}^{R} a_{q_{e_j}}^{L} a_{q_{e_i}}^{L*},$$

$$D_2 = a_{q_{k_i}}^{L*} a_{q_{k_j}}^{L} a_{q_{e_j}}^{L} a_{q_{e_i}}^{L*} + a_{q_{k_i}}^{R*} a_{q_{k_j}}^{R} a_{q_{e_j}}^{R} a_{q_{e_i}}^{R*},$$

$$E_2 = a_{q_{k_i}}^{L*} a_{q_{k_j}}^{L} a_{q_{e_j}}^{L} a_{q_{e_i}}^{L*} - a_{q_{k_i}}^{L*} a_{q_{k_j}}^{L} a_{q_{e_j}}^{R} a_{q_{e_i}}^{R*},$$

$$F_1 = 0.5 \cdot \left(m_{\tilde{\chi}_j^0}^2 - \hat{u}\right)\left(m_{\tilde{\chi}_i^0}^2 - \hat{u}\right) + \left(m_{\tilde{\chi}_i^0}^2 - \hat{t}\right)\left(m_{\tilde{\chi}_j^0}^2 - \hat{t}\right) - \hat{s}\left(\hat{s} - m_{\tilde{\chi}_i^0}^2 - m_{\tilde{\chi}_j^0}^2\right)$$
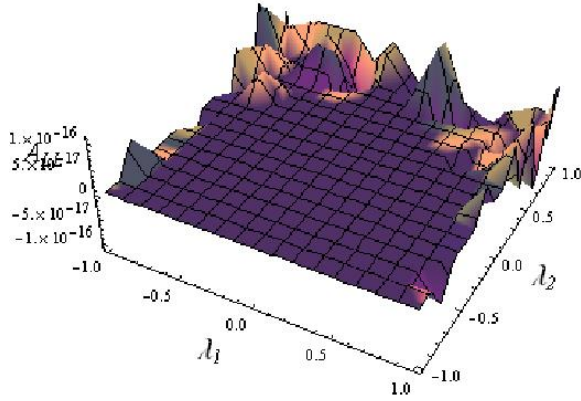
$$F_2 = m_{\tilde{\chi}_i^0} m_{\tilde{\chi}_j^0} \hat{s}$$

Coefficients of asymmetry in these notations will be written as follows:

$$A_{LL}(-\lambda_1, \lambda_2) = \frac{\lambda_1(C_1 F_1 + D_1 F_1 + C_2 F_2 \lambda_2 + E_1 F_1 \lambda_1 + E_2 F_2 \lambda_2)}{B_1 F_1 + F_2\{B_2 + D_2 \lambda_2)}$$

$$A_{LL}(\lambda_1, -\lambda_2) = \frac{\lambda_2(D_1 F_1 + E_1 F_1 \lambda_1 - F_2(D_2 + E_2 \lambda_1))}{B_1 F_1 + B_2 F_2 + C_1 F_1 \lambda_1 - C_2 F_2 \lambda_1}$$

Fig.3 shows the dependence $A_{LL}(\lambda_1, -\lambda_2)$.

29

Figure 3. The dependence $A_{LL}(-\lambda_1, \lambda_2)$

3.3 THE COEFFICIENT ASYMMETRY OF u - s CROSS PROCESS

To simplify the expression (18), enter the following notation:

$$A = \frac{-g^4}{2Cos^2\theta_w\left(\hat{s} - m_Z^2\right)\left(\hat{u} - m_{\tilde{q}_e}^2\right)},$$

$$B_1 = \left(a_{Z_q}^s + a_{Z_q}^L\right)a_{q_{e_j}}^{R*} a_{q_{e_i}}^R O_Z^{ij} - a_{q_{e_j}}^{L*} a_{q_{e_i}}^L a_{Z_q}^s O_Z^{ij*},$$

$$C_1 = a_{q_{e_j}}^{R*} a_{q_{e_i}}^R a_{Z_q}^s O_Z^{ij*} + a_{q_{e_j}}^{R*} a_{q_{e_i}}^R a_{Z_q}^L O_Z^{ij*} + a_{q_{e_j}}^{L*} a_{q_{e_i}}^L a_{Z_q}^s O_Z^{ij},$$

$$D_1 = a_{q_{e_j}}^{L*} a_{q_{e_i}}^L a_{Z_q}^s O_Z^{ij*} + a_{q_{e_j}}^{R*} a_{q_{e_i}}^R a_{Z_q}^s O_Z^{ij} + a_{q_{e_j}}^{R*} a_{q_{e_i}}^R a_{Z_q}^L O_Z^{ij},$$

$$E_1 = a_{q_{e_j}}^{R*} a_{q_{e_i}}^R a_{Z_q}^s O_Z^{ij*} + a_{q_{e_j}}^{R*} a_{q_{e_i}}^R a_{Z_q}^L O_Z^{ij*} + a_{q_{e_j}}^{L*} a_{q_{e_i}}^L a_{Z_q}^s O_Z^{ij},$$

$$F_2 = \left(m_{\tilde{\chi}_i^0}^2 - \hat{u}\right)\left(m_{\tilde{\chi}_j^0}^2 - \hat{u}\right),$$

$$B_2 = a_{Z_q}^s a_{q_{e_i}}^L a_{q_{e_j}}^{L*} O_Z^{ij} - \left(a_{Z_q}^s + a_{Z_q}^L\right)a_{q_{e_j}}^{R*} a_{q_{e_i}}^R O_Z^{ij*}$$

$$C_2 = a_{q_{e_j}}^{L*} a_{q_{e_i}}^L a_{Z_q}^s O_Z^{ij*} + a_{q_{e_j}}^{R*} a_{q_{e_i}}^R a_{Z_q}^s O_Z^{ij} + a_{q_{e_j}}^{R*} a_{q_{e_i}}^R a_{Z_q}^L O_Z^{ij},$$

$$D_2 = a_{q_{e_j}}^{R*} a_{q_{e_i}}^R a_{Z_q}^s O_Z^{ij*} + a_{q_{e_j}}^{R*} a_{q_{e_i}}^R a_{Z_q}^L O_Z^{ij*} + a_{q_{e_j}}^{L*} a_{q_{e_i}}^L a_{Z_q}^s O_Z^{ij},$$

$$E_2 = a_{q_{e_j}}^{L*} a_{q_{e_i}}^L a_{Z_q}^s O_Z^{ij*} - a_{q_{e_j}}^{R*} a_{q_{e_i}}^R a_{Z_q}^s O_Z^{ij} - a_{q_{e_j}}^{R*} a_{q_{e_i}}^R a_{Z_q}^L O_Z^{ij},$$

$$F_1 = m_{\tilde{\chi}_i^0} m_{\tilde{\chi}_j^0} \hat{s}$$

We use these notations and for the square of the modulus of the invariant amplitude of the cross process t-s we get the following expression:

$$M_u M_s^+ = A\left(\left(B_1 + C_1\lambda_1 + D_1\lambda_1 + E_1\lambda_1\lambda_2\right) \cdot F_1 + \right.$$
$$\left. + \left(B_2 - C_2\lambda_1 - D_2\lambda_1 + E_2\lambda_1\lambda_2\right) \cdot F_2\right)$$
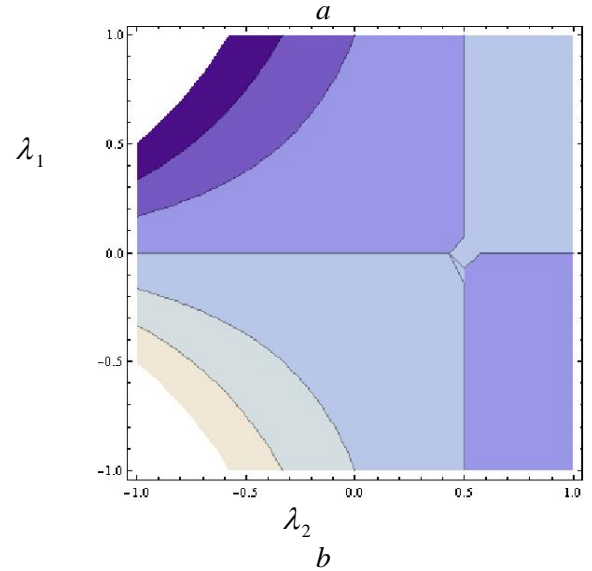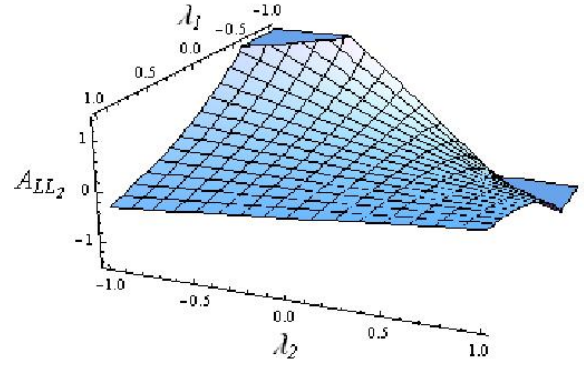
Accordingly the coefficients of asymmetry in these notations will be written as follows:

$$A_{LL}(-\lambda_1, \lambda_2) = \frac{\lambda_1(C_1F_1 + D_1F_1 + C_2F_2 + E_1F_1\lambda_2 + E_2F_2\lambda_2)}{B_1F_1 + F_2(B_2 + D_2\lambda_2)}$$

$$A_{LL}(-\lambda_1, \lambda_2) = \frac{\lambda_1(C_1F_1 + D_1F_1 + C_2F_2 + E_1F_1\lambda_2 + E_2F_2\lambda_2)}{B_1F_1 + F_2(B_2 + D_2\lambda_2)}$$

$$A_{LL}(\lambda_1, -\lambda_2) = \frac{\lambda_1(C_1F_1 + D_1F_1 + C_2F_2 + E_1F_1\lambda_2 + E_2F_2\lambda_2)}{B_1F_1 + F_2(B_2 + D_2\lambda_2)}$$

Fig.4 shows the dependence $A_{LL}(-\lambda_1, \lambda_2)$ and its counter-dependency.

a

b

Figure 4. The dependence $A_{LL}(-\lambda_1, \lambda_2)$ (*a*) and its counter-plot dependence (*b*)

The coefficient asymmetry of cross-channel of the proton-proton collision process at high energies has a more complex dependence on the degree of polarization λ_1 and λ_2. As can be seen, the coefficient of asymmetry of the u - s cross process is symmetrically relative to the change of the signs λ_1 and λ_2, i.e. $A(-\lambda_1, \lambda_2) = -A(\lambda_1, -\lambda_2)$. In the region close to the values of the parameters λ_1 and λ_2 to (-1, 1) and (1, -1) gets the maximum value and practically remains constant. The value of the coefficient asymmetry t - u cross-process is zero. The effective cross-section of the t-u cross-process does not depend on the relative direction of proton polarization. The coefficient of asymmetry of the

cross-process s - t at $\lambda_1 = -1$ and $\lambda_2 = -1$ has a minimum value, and $\lambda_1 = 1$ and $\lambda_2 = 1$ has a maximum value.

The table shows the values of the coefficient of linear dependence asymmetry coefficient on the polarization degree of one of the colliding proton beams in the absence of polarization of the other proton beam.

linear coeff.	t - s	t - u	s - u
$K\left(A_{LL_1}(\lambda_1,0)\right)$	2/3	0	1/2
$K\left(A_{LL_1}(0,\lambda_{12})\right)$	0	0	0
$K\left(A_{LL_2}(\lambda_1,0)\right)$	0	0	0
$K\left(A_{LL_2}(0,\lambda_1)\right)$	1/2	0	-1/2

4. CONCLUSION

1. The cross-section of a proton collision at high energies depends on the energy of the colliding protons and increases with increasing proton energy.
2. The polarization of protons affects their effective colliding cross-section. The cross-section can increase or decrease depending on the mutual direction of polarization and the collision axis of protons. The effective collision cross-section is maximal when the polarizing directions of the colliding protons are opposite.
3. The coefficient of asymmetry of the process with participation a Z^0 photon is proportional to the product $-(\lambda_1\lambda_2)$ and with participation the scalar quarks (t and u channels) is proportional to λ_1 or λ_2. The overall asymmetry coefficient of the process is determined by $\lambda_1(1-\lambda_2)$.

All calculations were performed using the program package "Mathematica-10" and programs compiled in the algorithmic language "Visual Fortran -6.5". The graphics were built using the "Origin-9.5 "software package and edited using" Adobe Photoshop"

5. REFERENCES

1. The ATLAS Experiment at the CERN Large Hadron Collider, ATLAS Collaboration, JINST 3, 2008, S08003
2. The ALIICE Collaboration K_0s K_0s correlations in pp collisions at √s = 7 TeV / 2012, arXiv:1206.2056v1 [hep-ex]
3. Smirnova L.N. / Letters in ECHAI. 2014, 11(185), p.9-3.
4. Howard E. Haber / Nuclear Physics B (Proc. Suppl.) 2001, v.101, p.217-236
5. Haber H.E., Kane G.L. / Physics Reports (Review Section of Physics Letters) 1985, v. 117, Issues 2–4, p.75-263 https://doi.org/10.1016/0370-1573(85)90051-1
6. Chatrchyan S.et al. CMS Collaboration / Phys. Lett. B 2012, v. 716, 30-6 DOI: 10.1016/j.physletb.2012.08.021 e-Print: 1207.7235 [hep-ex]
7. Aad G., Freiburg U et al. ATLAS Collaboration / Phys. Lett. B 716, 1 v. 2012, p.1-29, DOI: 10.1016/j.physletb.2012.08.020, e-Print: 1207.7214 [hep-ex] CERN-PH-EP-2012-218
8. Debovea J., Fuksb Bn., Klasena M. / arXiv:0804.0423v2 [hep-ph] 10 Oct 2008
9. Ahmadov A.I., Demirci1 M. / ArXiv: 1307.3777v1 [hep-ph] 14 Jul 2013
10. Demirci M., Ahmadov A.I./ Physical Review 2014, D 89, p.075015
11. Ahmadov A.I., Boztosun I., Muradov R.Kh., Soylu A., Dadashov E.A. / International Journal of Modern Physics E, 2006, v.15, No, 6, p.1183-1208
12. Bunce G. et al. RHIC Spin Group, 4-Year Research Plan, 2007 http://www.phy.bnl.gov/rhicspin/ documents/ 4year.pdf
13. ATLAS Collaboration, Report No. ATLAS-CONF-2013- 062
14. http://www.dslib.net/atom-jadro/issledovanie-spektra-jeffektivnyh-mass-dvuh-protonov-iz-reakcii-p-np-p.html
15. ATLAS Collaboration, Report No. ATLAS-CONF-2013- 047
16. Alizada M.R., Ahmadov A.I. / Bitlis Eren University Journal of Science, 2019, v. 8, p.16-24
17. Alizade M.R., Akhmedov A.I./ News of Azerbaijan National Academy of Sciences, Physical-technical and mathematical sciences series, physics and astronomy, 2020, v.2, p.135-143, (in English Transactions of National Academy of Sciences of Azerbaijan. Series of Physical-Technical and Mathematical Sciences).

CHANGE MECHANISMS OF ELECTRICAL CONDUCTIVITY OF NANO-SILICON UNDER THE INFLUENCE OF NEUTRONS

A.A. GARIBLI

National Nuclear Research Center, AZ 1073, Inshaatchilar pr. 4, Baku, Azerbaijan
Baku State University, AZ 1148, Z.Khalilov str.23, Baku, Azerbaijan

The role of recombination processes in n-Si was assessed by comparing the natural isotopes of Silicon in n-Si and the concentration of the charge carriers formed in n-Si under the influence of elastic scattering, radiation capture and radioactive decay rays in mixed nuclei under the influence of epithermal neutrons with the concentration of the charge carriers involved in electrical conductivity.

1. INTRODUCTION

Nano-silicon is of great importance in science, technology and new technological fields as a promising material due to its physical, superficial physicochemical properties. Based on silicon and nano-sized form, it is exposed to various types of rays, including neutrons, during application in solar converters, detectors, microelectronics and other fields. The effect of neutrons is the most common and practical significance [1-8]. This article attempts to explain the change mechanisms in the electrical conductivity of nano-silicon under the influence of epithermal neutrons. This article discusses the mechanism of the process by comparing the calculated concentrations of unbalanced carriers under the influence of unstable radioactive nuclei with nano-silicon nuclear transitions and radiation capture products under the influence of epithermal neutrons and the approximate concentrations of carriers involved in electrical conductivity.

2. EXPERIMENTAL

Nano-silicon purchased from ADS SCY Spring Nanomaterials Inc. Houston, with particle-size $d \approx 100 \, nm$, specific surface area $S_x = 80 \, m^2$/g, density $d = 0.08 \, qr/sm^3$, containing 1% of impurities was selected as a research object.

Nano-silicon samples were thermally-annealed for 6 hours at the 400-450 ° -C temperature using argon inert gas environment and then a certain amount of the samples were placed in the specific ampoule to undergo vacuum-assisted thermal annealing at T=400°C and $P \approx 1 \cdot 10^{-4}$ mm. Hg. pressure-for purification from water and other impurities in the

contact media. The silicon content in the used nano-silicon contains $92.2\%^{28}_{14}Si, 4.7\%^{29}_{14}Si, 3.1\%^{30}_{14}Si$ natural isotopes.

The samples were irradiated by neutron flux in the special aluminium ampoule. Neutron irradiation was carried out at the TRIGGA MARK type II nuclear reactor under a contract concluded between the Joseph Stefan Institute of Slovenia and the Azerbaijan National Nuclear Research Center [1-6]. The reactor is a pool type and operates with light water. The maximum power of the reactor was 250 kW neutrons with a flood density $\phi = 1.92 \cdot \frac{10^{13}n}{cm^2} \cdot sec$, and energy $E_n \approx 625 \div 10^5 \, eV$. The irradiation was carried out on the central A1 channel of the reactor. After irradiation, the samples were stored in the storage chamber during the 400-hours to stabilize isotopes with high activity and short half-life. After irradiation with different doses ($\tau = 0 \div 20$ hours, $\Phi=6{,}91 \cdot 10^{16} \div 1{,}38 \cdot 10^{18}$ n/cm^2), the electrical conductivity and dielectric permittivity of nano-silicon were investigated in T = $100 \div 400$K temperature and $\nu = 0 \div 1$MHz field-frequency ranges to obtain information about the formation of additional charge carriers and other types of defects under the influence of epithermal neutrons [3,5,7,8].

3. RESULTS AND DISCUSSION

The effect of epithermal neutrons on electrical conductivity in ϕ, ν, T intervals on the values of characteristic parameters of Nano-Silicon was investigated by the above methodology and the experimental results were interpreted in [1.8]. In these articles, the changes in the electrophysical properties under the influence of epithermal neutrons were qualitatively explained by the defect formation

processes of gamma and beta rays emitted into the environment as a result of radiation capture processes in nano-silicon under the influence of neutrons.

Nano-silicon undergoes more probable elastic scattering and radiation capture processes under the influence of epitermal neutrons. When neutrons interacting with $^{28}_{14}Si$, $^{29}_{14}Si$ nuclei, stable $^{29}_{14}Si$ and $^{30}_{14}Si$ nuclei, and when interacting with $^{30}_{14}Si$ nuclei, unstable $^{31}_{14}Si$ nuclei are obtained. This process is expressed in the following scheme.

$$^{30}_{14}Si(n, \gamma)^{31}_{14}Si \qquad (1)$$
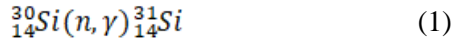
The gamma quantum released by this process interacts with the electron shell of the nano-silicon to provide a certain amount of energy to the n.Si structure. The maximum irradiation time with neutrons in experimental conditions is $\tau=20$ hours. $\Sigma E_\gamma = 9.85 \cdot 10^{18} eV/cm^3$ energy is given to n-Si by gamma rays emitted by $^{31}_{14}Si$ unstable nuclei during interaction with neutrons in the specified time interval (1). The radioactive $^{31}_{14}Si$ nucleus obtained by a nuclear reaction decomposes into beta according to the following scheme.

$$^{31}_{14}Si \xrightarrow{T_{1/2}=2.62\ saat} {}^{31}_{15}P + \beta + \bar{v} \qquad (2)$$
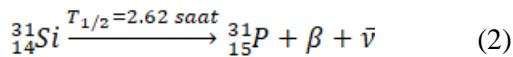
Where β^- beta particle with energy $E_\beta \approx 0.595\ MeV$, $\bar{v}$- antineutrons.

Radioactive $^{31}_{14}Si$ nuclei formed as a result of radiation with neutrons $\tau = 20$ hours

$$\Sigma E_\beta = 4.63 \cdot 10^{18} eV/sm^3 \qquad (3)$$

amount of energy is consumed to ionization processes in the environment by beta particles, which are the products of β^- - decay [1,2]

The n-Si sample, which is the object of study, is described in detail by gamma-spectrometry identification of basic and mixed nuclei under the influence of epitermal neutrons, the energy of emitted rays and kinetics of radioactive decay processes [4].

The amount of energy given off to the environment by gamma-rays as a result of the

$$^y_x A(n, \gamma)^{y+1}_x A \qquad (4)$$

process of nuclei in the mixed form in the observed neutron-activated n-Si was estimated approximately.

$$\sum_{mix} E_\gamma = 3.29 \cdot 10^{18} eV/sm^3$$

In general, the following amounts of energy can be transferred to n-Si as a result of elastic scattering and radiation capture processes during the action of epitermal neutrons on the studied n-Si samples.

$$\sum_i E_i = \sum_s E_S + \sum_\gamma E_\gamma + \sum_\beta E_\beta + \sum_\gamma E_{mix} \qquad (5)$$

Where $\sum_s E_s$ is the shear energy during scattering, $\sum_\gamma E_\gamma$ -$^{31}_{14}Si(n, \gamma)^{31}_{14}Si^*$ by nuclear reaction, $\sum_\beta E_\beta - {}^{31}_{14}Si - {}^{31}_{15}P$ beta released during radioactive decay, $\sum_\gamma E_{mix}$ are the energies released into the environment as a result of neutron activation processes by mixed nuclei in n-Si. Substituting their set values in (4), we can estimate the total energy given to n-Si when it is irradiated for 20 hours.

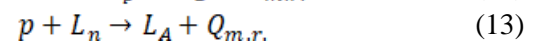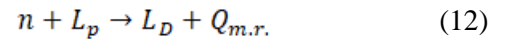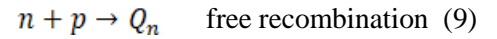$$\sum_i E_i = 1.78 \cdot 10^{19}\ eV/cm^3 \qquad (6)$$

Limit energies of electron-hole pairs in semiconductors are determined by the formula [9].

$$E_h = 3 \cdot E_g \qquad (7)$$

Given that the bandgap for nano-silicon samples is $E_g =$ 1.55 eV, it is possible to estimate the amount of electro-hole pairs that can occur when n-Si is irradiated with neutrons for $\tau = 20$ hours.

$$N_{pair} = \frac{\sum_i E_2}{E_h} = 3.8 \cdot 10^{18}\ pair/cm^3 \qquad (8)$$

The resulting unbalanced charge carriers undergo the processes of free recombination, localization, recombination in the centre within the n-Si particle according to the following schemes.

$$n + p \to Q_n \quad \text{free recombination} \quad (9)$$
$$n + L_A \to L_n \qquad (10)$$
$$p + L_D = L_p \qquad (11)$$
$$n + L_p \to L_D + Q_{m.r.} \qquad (12)$$
$$p + L_n \to L_A + Q_{m.r.} \qquad (13)$$

In neutron-irradiated samples, the study of physical properties is usually performed $\tau = 400$ hours after irradiation to ensure rapid radioactive decay and fall within the safety range of radioactivity. Therefore, in these samples, the carriers trapped in the $L_n L_p$ centres formed by the processes (10), (11) under the conditions of experimental observations are involved. Depending on the energy levels of these centres in the restricted zone, the transition of carriers from there to the conduction zone occurs at certain temperatures and electric field frequencies. The frequency and temperature dependences of the electrical conductivity of nano-silicon at different radiation doses with neutrons are given in [4,5,6]. Figure 1 shows the frequency dependence of the electrical conductivity of n-Si irradiated at different times. From these and other experimental results [4,5,6] it is possible to obtain estimates of the true part of the final electrical conductivity of n-Si before irradiation and at different doses. Based on the experimentally determined values of electrical conductivity, the concentrations of the

carriers can be generally determined by the following formula.

$$\sigma = q \cdot n \cdot \mu \tag{14}$$

Where σ- electrical conductivity, the units are S / m, 1 / Ohm · m, q-charge of carriers, if electrons are taken $1.602/765 \cdot 10^{-19}$ A · sec, n- charge carriers density - $1/cm^3$, μ mobility of–charge carriers -$cm^2 /$ (V · sec).

Information on the mobility of carriers for nano-silicon is very limited and uncertain. Therefore, for calculations, in bulk crystalline silicon, the mobility of electrons is $\mu_e \approx 1200 \div 1450 cm^2 / V \cdot sec$ and the mobility of the holes is $\mu_d = 500 \ cm^2 / V \cdot sec$ [9,10]. The density of specific carriers for bulk crystalline silicon is equal to $n_m = 1.5 \cdot 10^{10} \ 1/sm^3$. Based on experimental electrical conductivity values of irradiated n-Si samples at $\nu = 0.1 \ MH_2$ frequency and T=100-400K temperatures, the values determined by the expression for the electronic conductivity of the carriers (12) are $n_{io}(0.1 \ Mhz, 100K) \approx 1.45 \cdot 10^8 1/sm^2$, $n_o(0.1 \ MH_2, 400K) \approx 5.39 \cdot 10^{11} 1/sm^2$. As can be seen, the specific charge mobility of nano-silicon at T = 100K is much lower than that of crystals. This suggests that surface levels in nanocrystals act as recombination centres. The density of the charge carriers at 100 K and 400 K at 1MHz electric field values in n-Si, respectively, was determined.

$$P_0(1Mhz, 100K) = 2.5 \cdot 10^{12} 1/sm^3 \tag{15}$$

$$N_0(1Mhz_2, 400K) = 8.6 \cdot 10^{12} 1/sm^3 \tag{16}$$

The amount of specific charge carriers of nano-silicon at 1MHz and 100 - 4006K temperatures is higher than that of crystals. Appropriately determined the concentrations of charge carriers in n-Si irradiated with neutrons for τ = 20 hours under appropriate conditions (ns)

$$n_s(0.1 \ Mhz, 100 \ K) = 2.58 \cdot 10^{11} \ 1/cm^3 \tag{17}$$

$$n_s(0.1 \ Mhz, 400 \ K) = 9.10 \cdot 10^{11} \ 1/cm^3 \tag{18}$$

$$n_s(1 \ Mhz, 100 \ K) = 1.08 \cdot 10^{13} \ 1/cm^3 \tag{19}$$

$$n_s(0.1 \ Mhz, 400 \ K) = 1.67 \cdot 10^{13} \ 1/cm^3 \tag{20}$$

As can be seen, the concentrations of the charge carriers determined based on the electrical conductivity measured under the same conditions increase as the radiation dose rate, field frequency and temperature increase. In practice, under optimal conditions, the density of charge carriers involved in the electrical conductivity of nano-silicon irradiated H=1Mhz, T=400 K, $T_s = 20 \ hours$ hours is $2.2 \cdot 10^5$ times

higher than the density of the initial charge carriers formed during the irradiation process.

$$\frac{N_{pair}}{n_s(1 \ Mh_z, 400 \ K)} = \frac{3.8 \cdot 10^{18}}{1.67 \cdot 10^{13}} \approx 2.2 \cdot 10^5 \tag{21}$$

This shows that most of the unbalanced charge carriers formed by the action of gamma and beta rays emitted by nuclear transmutation under the influence of neutrons undergo recombination processes. Only 10^{-5} part is involved in electrical conductivity.

4. CONCLUSION

As a result of elastic scattering in n-SI under the influence of epithermal neutrons, neutralization of neutron-activated nuclei, and beta radioactive decay, the unbalanced charge carriers generated by the energies transferred to n-Si particles undergo various recombination processes.

Therefore, only 10^{-5} part of these carriers are involved in electrical conductivity.

5. REFERENCES

1. GaribliA.A., GaribovA.A., Huseynov E.M. / Defect formation processes in the silicon nanoparticles under the neutron irradiation" Modern Physics Letters B 33 (26), 2019, 1950315.

2. GaribliA.A. / Energy transfer and defect formation processes in nano silicon under the influence of epithermal neutrons" Eurasion journal of physics and functional materials,3, 2019, p.242-253

3. A.A.Qəribli, S.Z.Məlikova, M.Ə.Ramazanov, A.A.Qəribov/ Nano-Silisiumda epitermal neytronların təsiri altında baş verən proseslərin Furye İQ-spektroskopiya üsulu ilə tədqiqi" Journal of radiation researches, 2018,2 ,p.109-118.

4. Huseynov E., Garibli A. /Effect of neutron flux on the frequency dependence of permittivity of nano silicon particles" Silicon,2018, 10, 1, p.99-105.

5. Huseynov E., Garibli A. /The neutron irradiation effects on the temperature dependencies of the electrical conductivity of nanosilicon particles" Modern Physics Letters B , 2017, 31(28), 1750257.

6. Garibli A., Huseynov E., Garibov R, Mehdiyeva A. /Additive analysis of nano silicon under the influence of neutron irradiation" International Journal of Modern Physics B 30 (10), 2016, 1650040.

7. Huseynov E., Garibli A. /Effect of neutron flux on the frequency dependencies of electrical conductivity of silicon nanoparticles" Revista mexicana de física 62 (4), 2016, 299-303.

8. Garibli A.A, Ramazanov M.Ə, Huseynov E.M./ Electrical Conductivity- Temperature Dependencies of nano silicon particles exposed to neutron irradiation" Modern trends in physics. İnternational conference. 2017,p.32

9. Elango M.A./ Elementary inelastic radio processes. M.Nauka, 1988, p. 152.

10. Ambrico M., Schiavulli L., Ligonzo T. et al./Optical absorption and electrical conductivity measurements of microcrystalline silicon layers grown by SiF4/H2 plasma on glass substrates//Thin Solid Films, 2001,383 p.200-202.

REGIOSPECIFIC N-TOSYLATION OF 4,5,6,7-TETRAHYDROINDAZOLES DERIVED FROM β-KETOLS

G.J.HASANOVA

Baku State University, Z.Khalilov Str.23, Baku, Azerbaijan

The regiospecific character of tosylation of 4-tolyl-5-acetyl-6-hydroxy-3,6-dimethyl-4,5,6,7-tetrahydroindazole has been established. The interaction of the latter with tosyl chloride in a boiling acetone in the presence of triethylamine proceeds exclusively at position N(1) and leads to 4-tolyl-5-acetyl-6-hydroxy-3,6-dimethyl-1-tosyl-4,5,6,7-tetrahydroindazole. Tosylation at position N(1) was also established in the case of the interaction of ethyl 3,6-dihydroxy-6-methyl-4-phenyl-4,5,6,7-tetrahydro-2H-indazole-5-carboxylate with tosyl chloride under similar conditions.

1. INTRODUCTION

Being polyfunctional compounds, 2,4-diacyl(dialk-oxycarbonyl)-3-R-5-hydroxy-5-methylcyclohexanones (1), also known as β-cycloketols, are promising building blocks for fine organic synthesis [1,2]. β-Cycloketols easily enter into heterocyclization reactions with various 1,2- and 1,3-dinucleophilic agents with the formation of isoquinolines (2) [3-6], indazoles (3) [7-11], benzo[c] isoxazoles (4) [8-10], [1,2,4]triazolo[3,4-b]quinazolines (5) and pyrazolo[3,4-c]isoquinolines (6) [12], 4,5,6,7,8,9-hexahydropyrazolo[1,5-a]quinazolines (7) and derivatives of 6,7,8,8a-tetrahydropyrazolo[5,1-b]quinazolin-9(5H)-one (8) [13] (Scheme 1).
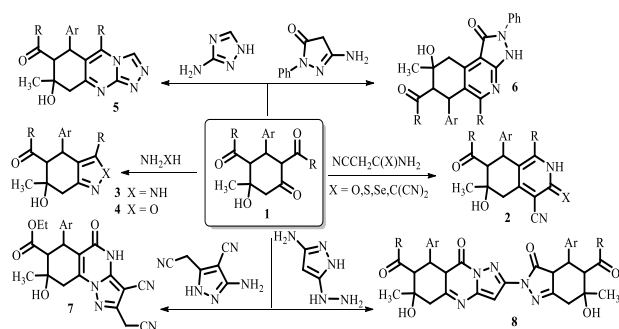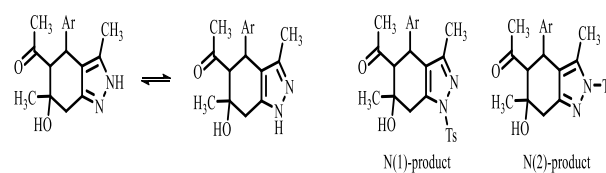

Scheme 1.

2.EXPERIMENTAL

Among the presented heterocyclic systems, indazole derivatives (3) attracted our attention. The synthesis of compounds (3) was first described by Paul Rabe and Fritz Elsé at the beginning of the 20th century. Since that time, a large amount of data has been accumulated on the synthesis of such indazoles using various β-cycloketols and substituted hydrazines [7-11, 14, 15], however, the direction related to the transformation and functionalization of indazoles (3) has received much less development.

It should also be noted that indazole scaffold is the structural basis of many compounds of therapeutic value. Continuing the research in the field of chemistry of β-cycloketols and their analogues [16-19], we decided to study the regiodirectionality of the indazole tosylation reaction (3). Indazole (3) tosylation can in principle proceed in three different directions - with the formation of N(1)-, N(2)- and O-derivatives (Scheme 2). The formation of the regioisomeric N(1) and N(2)-products can be assumed based on the principle possible prototropic tautomerism indazoles (3):

N(1)-product   N(2)-product

Scheme 2.

It was experimentally established that the interaction of indazole (3a) with tosyl chloride in dry acetone in the presence of a base (Et₃N) as the only isolated reaction products formed exclusively N(1)-tosyl derivative (3b) (Scheme 3).
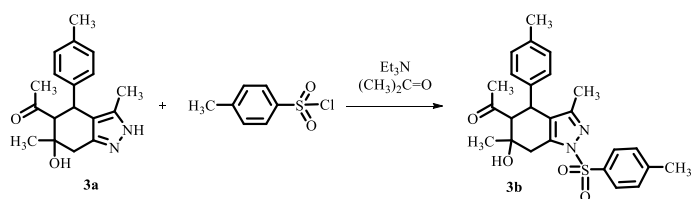
Scheme 3.

Structure (3b) was confirmed by NMR spectroscopy (Fig. 1, Fig. 2), as well as the result of X-ray diffraction (Fig. 3).
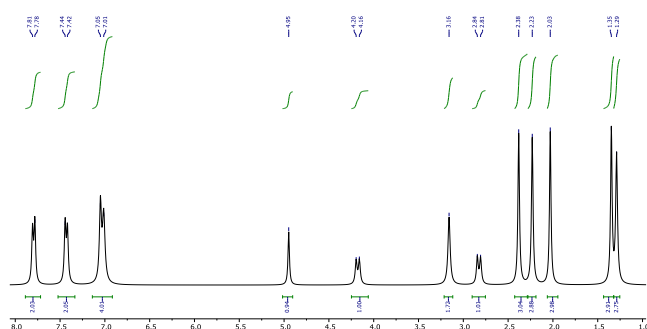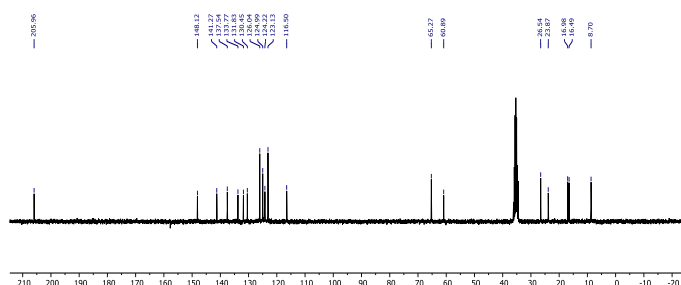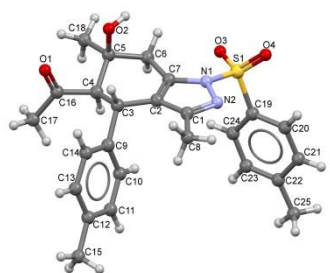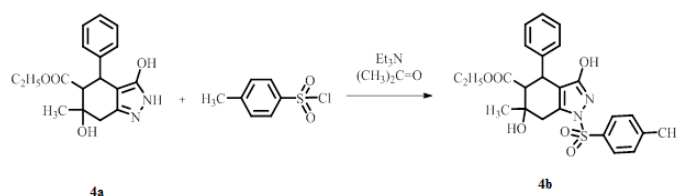

Figure 1.^{1}H NMR spectra of compound (3b)

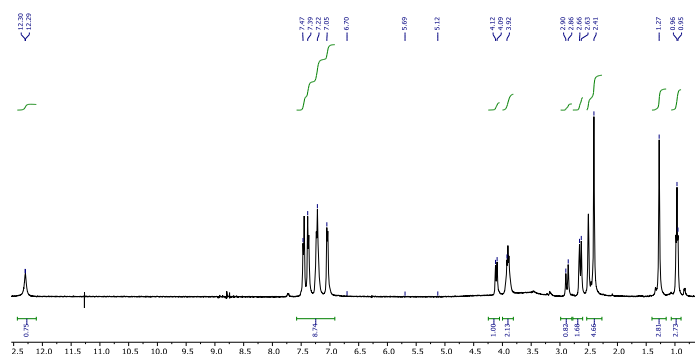Figure 2.^{13}C NMR spectra of compound (3b)

Figure 3. View of molecule of compound (3b) according to X-ray diffraction

Previously, the authors [20] carried out the synthesis and detailed structural study of ethyl 3,6-dihydroxy-6-methyl-4-phenyl-4,5,6,7-tetrahydro-2H-indazole-5-carboxylate (4a). In this compound, unlike compound (3a), there is a hydroxyl group at the pyrazole ring, which is an additional nucleophilic center capable of interacting with tosyl sulfoloride. From this point of view, it was interesting to study the selectivity of tosylation of the above compound. According to the results of the reaction of compound (4a) with toluenesulfonyl chloride in boiling acetone in the presence of triethylamine, it was found that tosylation does not affect the hydroxyl group. However, the NMR data unanimously confirm the introduction of a tosyl group into the molecule, therefore, based on the result of the synthesis of (3a), we give structure (4b) to the synthesized compound (Scheme 4).

Scheme 4.

Below is the ^{1}H NMR spectra of compound (4b) (Fig. 4), in which a weak-field signal in the form of a broadened singlet at 12.30 ppm. corresponds to the proton of the hydroxyl group at the pyrazole ring:

Figure 4. 1H NMR spectra of compound (4b)

3.RESULTS AND DISCUSSION

The ^{1}H and ^{13}C NMR spectrum were measured on a Bruker AC-300 MHs spectrometer at 300 and 75 MHs, respectively in a DMSO-d6 solution, residual signals of solvent were used as a standard. The IR spectra were run on a Varian 3600 FT-IR Excalibur Series FTIR spectrometer in KBr pellets. Elemental analysis for C, H and N was performed on a Carlo Erba 1106 analyzer. The experimental data for (3a) were obtained at 296(2) K on a Bruker APEX-II CCD

automatic three-circle diffractometer (MoKα, graphite monochromator, CCD detector, ω-scanning, 2θmax = 49.42°). All calculations were carried out using the SHELXT software suite [21]. The initial positions of the hydrogen atoms were found from the difference synthesis of electron density, and were geometrically calculated and clarified using the rider model with Uizo = nUeq carrier atom (n = 1.5 for methyl groups, n = 1.2 for other hydrogen atoms). The structure was clarified by full-matrix least squares in the anisotropic approximation for non-hydrogen atoms in F2.

The melting points were measured on a Kofler hot stage and were not adjusted. The purity of the synthesized compounds was checked by TLC on Silufol UV-254 plates, eluent–acetone–hexane (1:1), development in iodine vapor, UV detector.

General synthesis method

A mixture of the corresponding tetrahydroindazole (3a) and (4a) (5 mmol), 0.95 g (5 mmol) of p-toluenesulfonyl chloride and 1 ml of triethylamine is boiled in 30 ml of dry acetone for 6-8 hours (TLC conversion control). The mixture is cooled, and 30 ml of cold distilled water are added to the cooled solution. The resulting suspension is incubated for 24 hours, the precipitate is filtered off and recrystallized from EtOH. The products (3b) and (4b) are obtained in the form of white fine crystalline powders.

4-tolyl-5-acetyl-6-hydroxy-3,6-dimethyl-1-tosyl-4,5,6,7-tetrahydroindazole (3b), yield 67%, mp. 187°C.

^{1}H NMR spectrum (300 MHz, DMSO-d6), δ, ppm: 1.28 s (3H, CH3), 1.34 s (3H, CH3), 2.02 s (3H, CH3), 2.22 s (3H, CH3), 2.37 s (3H, CH3), 2.81 d (1H, H5, 3J 10.7 Hz), 3.15 br.s (2H, H7), 4.17 d (1H, H4, 3J 10.7 Hz), 4.94 br.s (1H, OH), 6.99 d (2H, H Ar, 3J 7.5 Hz), 7.05 d (2H, H Ar, 3J 7.5 Hz), 7.42 d (2H, H3, H5 Ts, 3J 7.8 Hz), 7.79 d (2H, H2, H6 Ts, 3J 7.8 Hz).

^{13}C NMR spectrum (75 MHz, DMSO-d6), δ, ppm: 12.9, 20.6, 21.1, 28.0, 30.7, 38.7, 38.9, 65.0, 69.4, 120.7, 127.3, 128.4, 129.2, 130.2, 134.6, 136.0, 137.9, 141.7, 145.4, 152.3, 210.1.

Found, %: C 66.34; H 6.36; N 6.15. $C_{25}H_{28}N_2O_4S$ (M 452.57). Calculated, %: C 66.35; H 6.24; N 6.19.

1-(6-hydroxy-3,6-dimethyl-4-(4-methylphenyl)-1-tosyl-4,5,6,7-tetrahydro-1H-indazol-5-yl)ethanone (4b), yield 62%, mp. 173°.

^{1}H NMR spectra of compound (4b) is shown in Fig. 4. Found, %: C 61.37; H 5.62; N 6.05. $C_{24}H_{26}N_2O_6S$ (M 470.15). Calculated, %: C 61.26; H 5.57; N 5.95.

4. CONCLUSION

Thus, as a result of the studies, it was found that the tosylation of 4,5,6,7-tetrahydroindazole derivatives of diacyl(diethoxycarbonyl)β-ketols in boiling acetone in the presence of triethylamine proceeds regiospecifically at the N(1) position of the heterocycle.

5. REFERENCES

1. Abiyeva, A.Y., Ismiyev, A.I., Nagiyev, Kh.D., Chyragov, F.M., Askerov, R.K. /Synthesis, crystal structure and research opportunities of 2,4-diacetyl-3-(3`-nitrophenyl)-5-hydroxy-5-methylcyclohexanone. New materials, Compounds and Applications, 2018, 2(1), p.22-27.
2. Ismiyev, A.I. /A new approach to synthesis of functionalized spiro[2,5]undec-2-en-2-carboxylates. New materials, Compounds and Applications, 2019, 3(3), p.172-179.
3. Dyachenko, V.D., Sukach, S.M., Dyachenko, A.D. /Synthesis of partially hydrogenated isoquinoline derivatives by condensation of 2,4-diacetyl-3-aryl(hetaryl)-5-hydroxy-5-methylcyclohexanones with malononitrile and its dimer and a study of their alkylation. Chemistry of Heterocycic Compounds, 2015, 51(1), p.51-55.
4. Dyachenko, V.D., Karpov, E.N. /Synthesis of functionalized alkyl-substituted cyclohexanones, pyridines, and 2,3,5,6,7,8-hexahydroisoquinolines by condensation of aliphatic aldehydes with CH acids. Russian Journal of Organic Chemistry, 2014, 50(12), p.1787-1796.
5. Sukach, S.M., Dyachenko, V.D./ Multicomponent synthesis of 3-(alkylsulfanyl)-8-aryl(hetaryl)-7-acetyl-6-hydroxy-1,6-dimethyl-5,6,7,8-tetrahydroisoquino-line-4-carbo-nitriles. Russian Journal of Organic Chemistry, 2015, 51(7), p.1020-1025.
6. Dyachenko, V.D., Sukach, S.M. /Synthesis of 7-acetyl-8-aryl(hetaryl)-6-hydroxy-1,6-dimethyl-3-selenoxo-2,3,5,6,7,8-hexahydroiso-quinoline-4-carbonitriles by the condensation of 2,4-diacetyl-3-aryl(hetaryl)-5-hydroxy-5-methyl-cyclohexanones with cyanoseleno-acetamide. Chemistry of Heterocycic Compounds, 2011, 46(12), p.1467.
7. Gein, V.L., Nosova, N.V., Potemkin, K.D., Aliev, Z.G., Krivenko, A.P./ Synthesis and structure of diisopropyl 6-Hydroxy-6-methyl-4-oxocyclohexane-1,3-dicarboxylates and their reactions with nucleophilic reagents. Russian Journal of Organic Chemistry, 2005, 41(7), p.1016-1022.
8. Sorokin, V.V., Grigoryev, A.V., Ramazanov, A.K., Krivenko, A.P. /Synthesis of 3-R2-4-R1-

acetyl-(ethoxycarbonyl)-6-hydroxy-6-methylindazoles. Chemistry of Heterocycic Compounds, 1999, 35(6), p.671-673.

9. Smirnova, N.O., Plotnikov, O.P., Vinogradova, N.A., Sorokin, V.V., Krivenko, A.P. /Synthesis and biological activity of substituted 7-aza-8-aza(oxa)-bicyclo[4.3.0]-6,9-nonadienes. Pharmaceutical Chemistry Journal, 1995, 29(1),p.49-50.

10. Hote, B.S., Lokhande, P.D./ Novel and efficient synthesis of 4-indazolyl-1,3,4-trisubstituted pyrazole derivatives. Synthetic Communications, 2014, 44(10), p.1492-1500.

11. Gein, V.L., Gein, N.V., Potemkin, K.D., Krivenko, A.P. /Reactions of dimethyl and di-tert-butyl 2-aryl-4-hydroxy-4-methyl-6-oxocyclohexane-1,3-dicarboxy-lates with difunctional nucleophiles. Russian Journal of General Chemistry, 2004, 74(10), p.1564-1568.

12. Dyachenko, V.D., Sukach, S.M. /Synthesis of 1H-pyrazolo[3,4-c]isoquinolin-1-ones by the condensa-tion of cyclohexanone derivatives with 3-amino-1-phenyl-1H-pyrazol-5(4H)-one. Russian Journal of General Chemistry, 2012, 82(2), p.305-309.

13. Etman, H.A., Sadek, M.G., Khalil, A.G.M. / Synthesis of some new heterocycles derived from 3-amino-5-hydrazinopyrazole dihydrochloride. Research Journal of Pharmaceutical, Biological and Chemical Sciences, 2015, 6(2), 247-254.

14. Gein, V.L., Zorina, A.A., Nosova, I.V., Voronina, É.V., Vakhrin, M. I., Kriven'ko, A. I. / Synthesis and antimicrobial activity of substituted tetrahydro-indazoles and cyclohexanones. Pharmaceutical Chemistry Journal, 2007, 41(6), p.319-322.

15. Gein, V.L., Yankin, A.N., Nosova, N.V., Levandovskaya, E.B., Novikova, V.V., Rudakova, I.P. /Synthesis and biological activity of 4,5,6,7-tetrahydro-2H-indazole derivatives. Russian Journal of General Chemistry, 2019, 89(6), p.1169-1176.

16. Ismiyev, A.I., Maharramov, A.M., Aliyeva, R.A., Askerov, R.K., Mahmudov, K.T., Kopylovich, M.N., Naili, H., Pombeiro, A.J.L./ Syntheses and some features of five new cyclohexane-1,3-dicarboxylates with multiple stereogenic centers. Journal of Molecular Structure, 2013, 1032, p.83-87.

17. Magerramov, A.M., Ismiev, A.I., Kadyrova, N.A., Gadzhieva, K.É., Askerov, R.K., Potekhin, K.A. /Crystal structure of diethyl-1-isobutyl-9-hydroxy-9-methyl-7-phenyl-1,4-

diazaspiro[4,5]decane-6,8-dicar-boxylate C25H38N2O5. Journal of Structural Chemistry, 2013, 54(6), p.1137-1139.

18. Dotsenko, V.V., Krivokolysko, S.G., Polovinko, V.V., Litvinov, V.P. /On the regioselectivity of the reaction of cyanothioacetamide with 2-acetylcyclo-hexanone, 2-acetylcyclopentanone, and 2-acetyl-1-(morpholin-4-yl)-1-cycloalkenes. Chemistry of Heterocyclic Compounds, 2012, 48, p.309-319.

19. Maharramov, A.M., Ismiyev, A.I., Allahverdiyev, M.A., Maleev, A.V., Potekhin, K.A. /Crystal structure of phenylhydrazine with diacetyl substituted ketol of the cyclohexane series. Journal of Structural Chemistry, 2016, 57(4), p.764-770.

20. Maharramov, A.M., Ismiyev, A.I., Rashidov B.A./ Ethyl 3,6-dihydroxy-6-methyl-4-phenyl-4,5,6,7-tetrahydro-1H-indazole-5-carboxylate monohydrate. Acta Crystallographica Section E: Crystallographic Communications, 2011, 67(2), p.0480.

21. Sheldrick, G. M. /SHELXTL v. 6.12, Structure Determination Software Suite, Bruker AXS. Madison, Wisconsin, USA, 2001.

CARBON COATING FOR REINFORCING PHOTOCATALYTIC ACTIVITY OF TITANIUM DIOXIDE: A REVIEW

A.M. RAHIMLI

Baku State University, Z. Khalilov Street, 23 Baku, AZ1148, Azerbaijan

Oxide-based semiconductor photocatalysis has attracted much attention due to its desirable properties. Photostable, non-toxic and highly reactive nature makes it attractive candidate for heterogenous photocatalysis. However, large band gap and speedy electron-hole recombination are the limiting factors for its photocatalytic efficiency. Doping TiO_2 with other materials is thought to sensitize titanium dioxide for the much larger visible fraction and retard electron-hole recombination. This has prompted researchers from many fields of science to look for the most suitable material and synthesis methods in order to optimize the surface chemistry of titanium dioxide nanoparticles for their interests. It was found that, carbon-coated TiO_2 modified exhibited larger absorption in the visible region and enhanced the degradation of organic dyes under visible light. Therefore, considerable amount of reports has been given on the carbon-modified TiO_2 nanoparticles. In this paper, carbon coating methods for the surface modification of TiO_2 nanoparticles are summarized by emphasizing their effect on the absorption and decomposition of different pollutants in aqeous solutions.

1. INTRODUCTION

Over the past decades, oxide-based semiconductor photocatalysis has received significant interest of scientists in many fields of chemistry, physics and material science. Among various semiconductor photocatalysts (WO3, ZnO, ZnS, Fe2O3, CdS, and SrTiO3) used, most attention has been given to TiO_2 because it is inexpensive, nontoxic, photostable and commercially available [1, 2]. These nanoparticles are utilized both in the bare form and sometimes their surfaces are modified with some organicmaterials to attain specific properties in the final product. Surface coated TiO_2 has drawn increasing attention for use in many application fields, such as anode material in sodium ion batteries [3], photocatalyst [4], and it was found to be quite useful for photocatalytic splitting of water [5]. It has been proven to be the most suitable photocatalyst for heterogeneous photocatalysis and has been extensively used in the photocatalytic degradation reactions of organic contaminants. However, the photocatalytic degradation rates for many organic pollutants tend to be too slow to be of practical interestwhich can be related to some factors like speedy electron-hole recombination due to the short charge separation distances within the particle which hinders chemical reactions to happen. Another reason is the large bandgap of TiO_2 (3.2 eV), so wavelengths below 400 nm are necessary for excitation, which limits its photosensitivity to the UV part of the solar spectrum. Doping other materials in anatase TiO_2 nanoparticles is thought to sensitize titanium dioxide for the much larger visible fraction. [6]. Variety of organic materials have been used for the surface coating of TiO_2 nanoparticles such as noble metals[7], polymer [8], carbon [9] and dye [10]. Considerable amount of reports has been given on the surface modified TiO_2 nanoparticles [4-6]. But sometimes a coating process is complicated and requires the surface treatment before coating [6]. Modification of TiO_2 with noble metals is expected to facilitate its photocatalytic performance in various applications. However, TiO_2 modification with noble metals as a practical modification technology is restricted because noble metals are expensive. In contrast, TiO_2 modified with nonmetal elements such as N, F, S and C exhibited larger absorption in the visible region and enhanced the degradation of organic dyes under visible light irradiation [11-13]. It is found that carbon coverage inhibits the phase transformation of TiO_2 and makes the absorption edge of titania shift to the visible region which results in efficient utilization of the active materials, and also increase electrical

conductivity of the materials [11]. Various methods for synthesis of carbon coating on the surface of TiO_2 nanoparticles have been employed to sensitize titanium dioxide for the much larger visible fraction. In this review we aim to provide a detailed introduction into the recent surface modification methods of TiO_2 nanoparticles by investigating the effect of surface modification on the electronic and structural properties of TiO_2. Special emphasis is given to the recent carbon coating technologies for the enhanced thermal stability, photocatalytic activity and absorptivity of TiO_2.

Various surface modification technologies available to coat TiO_2 with carbon reviewed in this article include pyrolysis of sucrose [13], sol–gel technique using alkoxide as precursors [14,16], treatment of TiO_2 at very high temperature with various polymers under an inert atmosphere [17], etc. Lin et al. [13] prepared simple carbon-coated titania (CCT) via pyrolysis of sucrose. Sucrose/TiO_2 precursors were prepared by impregnating titania with aqueous solutions of sucrose. Both the precursors and pure titania were calcined at 400, 500 or 600°C in N_2 with 50 mL min^{-1}flowing rate of for 2 h. Sucrose carbon was prepared via pyrolysis of sucrose at 500°C in flowing N_2 for 2 h as mentioned above. The samples were characterized via several characterization techniques and their photocatalytic properties were evaluated through model pollutant. CCT nanocomposites showed good photocatalytic activity for the photodegradation of MB under visible light illumination, whereas it was simply bleached over pure titania at the same condition. It becomes clear that carbon coating causes the phase transformation of TiO_2 and makes the absorption edge of titania shift to the visible region. Additionally, this method is promising for the controllability of the amount of carbon layers in CCT by changing the sucrose content in the precursors and the impregnation time. The pre-treatment of precursors and titania and high temperature conditions limit the further development of this method. Sol-gel method [14] have been employed for the preparation of carbon-coated titania by using various titanium alkoxide precursors as carbon source. It was found that carbon doped TiO_2 shows five times more efficiency than nitrogen doped TiO_2 [24]. Three samples TiO_2-C1a, TiO_2-C1b, and TiO_2-C2 containing 2.98, 0.42, and 0.03% carbon, respectively were prepared by the hydrolysis of titanium tetrachloride with tetrabutylammonium hydroxide followed by calcination at 400°C for 0.25 h (TiO_2-C1a) and 1 h (TiO_2-C1b), and at 550°C for 4 h (TiO_2-C2). Unmodified TiO_2 was

prepared by the same procedure but replacing the nitrogen base by sodium hydroxide. X-ray diffraction (XRD) measurements showed that all the materials are in anatase modification except TiO_2-C2 in which small amount of the rutile phase was also detected. X-ray photoelectron spectroscopy (XPS) measurements and Diffuse reflectance spectra revealed carbon content in the prepared sampes. In order to evaluate the photocatalytic activity of the new materials, photomineralization of water pollutant 4-chlorophenol with visible light (l = 455 nm) in the presence of the various photocatalysts was carried out. TiO_2-C1a and TiO_2-C1b showed complete mineralization after 210 and 180 min, respectively. UV absorption spectroscopy showed a small reduction in the 4-chlorophenol concentration. The corresponding rates found for TiO_2-C1a and TiO_2-C1b were about 30 and 60 times larger. The twofold rate enhancement induced by TiO_2-C1b relative to TiO_2-C1b (although the latter contains more carbon) may be due to the higher crystallinity of TiO_2-C1a as suggested by XRD spectra. In [16], authors employed sol–gel auto-combustion technique with a unique combination of the chemical sol–gel process and the combustion process for the synthesis of carbon-doped TiO_2 nanoparticles. Prepared samples were characterized by the means of X-ray diffraction(XRD), X-ray photoelectron spectra (XPS), Brunauer–Emmett–Teller method (BET) and UV–vis diffuses reflectance spectroscopy (DRS). UV–vis diffuse reflectance spectra of the prepared samples exhibited absorption in the visible light. After calcination at 873 K carbon coated samples showed the highest photocatalytic activity under solar irradiation.

Lettmann et al. [17] prepared titania based photocatalysts capable to photodegrade 4-chlorophenol (4CP) with visible light ($\lambda > 400$ nm) by a modified acid-catalysed sol–gel process using different alkoxide precursors as dopant ($Na_2[PtC_{16}]$). They have compared properties of catalysts prepared from different alkoxides and the surface areas and the pore-size distributions were calculated from adsorption measurements. The surface areas and pore-size distributions were found to be almost independent of the employed alkoxide precursor and centred around 135 m^2/g and 3.2 nm, respectively. Whereas the much higher activities of the sol–gel materials seem to depend on the nature of the alkoxide precursor. Total organic carbon content (TOC) measurements were used to prove the total mineralisation of 4CP. With the $Ti(O-iBu)_4$-based catalyst, 66% of 4CP are converted after 3h of irradiation as determined by

HPLC. The catalysts show an excellent long-time stability which indicates that the active site itself is resistant to photochemical degradation. Inagaki [18] et al. reported the preparation of carbon-coated anatase photocatalysts using different carbon precursors and described the effect of modification process on the photoactivity and adsorptivity properties of TiO. Poly(vinyl alcohol) (PVA), hydroxyl propyl cellulose (HPC) and poly(ethylene terephthalate) (PET) were used as precursors. The powder mixtures with different mixing ratios of anatase to carbon precursor were heat-treated on a tray of alumina (Al_2O_3) at various temperatures between 700 and 900°C for 1 h in a flow of Ar. In order to evaluate the photoactivity of the prepared samples, the decomposition behavior of MB in water was followed. Since the carbon layers formed on the TiO_2 particles were porous, the samples prepared showed a high adsorptivity, in addition to the photoactivity of TiO_2. So, it can be concluded from the experimental results obtained from above mentioned methods that carbon layer can give a rise to the adsorptivity, but at the same time it was found to weaken the intensity of UV rays arriving at the surface of the anatase photocatalyst and reduce the apparent diffusion rate of pollutants. In order to have a high photodecomposition rate (rate constant-k), a balance among these different effects of carbon layers is required. In [18] a good balance among these factors were attained when the samples prepared at 850°C for 1 h in a flow of Ar. The sample prepared at 850°C with a carbon content of about 3.5 wt % gave the highest rate constant k, where the transition to rutile was suppressed and carbon layer was thin enough to transmit UV rays to the surface of the TiO_2 particle. So, the apparent rate constant k was determined to be the result of a balance between the suppression of the transition of anatase to rutile and the decrease in UV rays reaching the TiO_2 surface, both of them being controlled by the carbon layer. In this study, it was experimentally shown that most of carbon-coated TiO_2 samples can decompose the pollutants in much higher rate than the bare TiO_2 nanoparticles.

The carbon-coated TiO_2 nanoparticles, on which various organic pollutants to be decomposed are adsorbed on the carbon layer and then diffuse onto the surface of catalyst particles TiO_2. When the carbon layer concentrates higher amount pollutants around the surface of TiO_2 nanoparticles, the decomposition rate of the pollutants will also accelerate. Therefore, adsorptivity of carbon layers is found to be a determining factor for the photocatalytic activity of carbon-coated TiO_2 [19]. Furthermore, it was shown schematically that UV

rays are weakened by scattering and absorption in carbon layer before arriving to the surface of photocatalyst particle [20]. So, it becomes clear that, the thicker carbon layer is a determining factor for the intensity of UV rays arriving on TiO_2 surface.
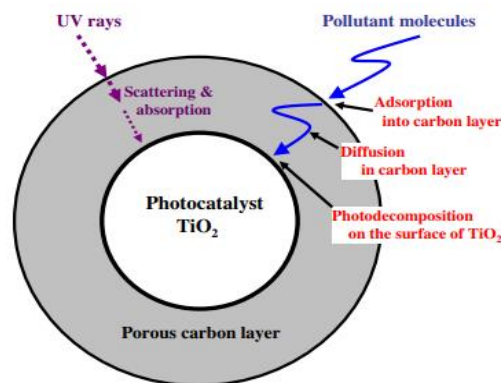

Figure 1. Schematic illustration of decomposition process on carbon-coated TiO_2 under irradiation [20]

Carbon-coated TiO_2 was easily prepared from the mixture of TiO_2 with PVA and then heating above 700°C in an inert atmosphere [21]. XRD measurements of the prepared samples proved the suppression of the phase transformation from anatase to rutile. Photocatalytic activity of the samples was observed in the solution of MB under the irradiation of visible light and the presence of carbon layer on the surface of the particles was found to enhance the adsorption process of MB to the surface of TiO_2 where it undergoes decomposition.

As it is clear, most of these methods are involved with elevated temperature, and consequently a high energy and operating conditions. To further improve the crystallinity of anatase TiO_2 for efficient photocatalysis, it is important to reduce surface defect sites as recombination centers for electron–hole pairs [22]. Thermal treatment is an effective approach to improve the crystallinity and discard surface defects at an appropriate content. However, thermal treatment often causes agglomeration of nanoparticles resulting in severe surface area decrease which further decreases the photocatalytic activity of the final product [23,24]. Considering the importance of surface states for photocatalysis, it is essential to develop preparation method that allows coating at low temperature. In addition to high temperature, the process mentioned above required specific conditions, such as the controlled nitrogen atmosphere. Therefore, hydrothermal process has been proposed as one alternative method that offers both low reaction temperature and simple preparation method.

Olurode et al. [25] offers a facile, low temperature hydrothermal method (200^oC) to construct carbon coating on the surface of TiO_2 by using dextrose as the source of carbon. FTIR spectra demonstrated the successful carbon coating on TiO_2 nanoparticles which were further supported by SEM and TEM observations. In order to evaluate the thermal behavior of TiO_2 before and after carbon-coating, TGA analysis of bare and carbon coated TiO_2 nanoparticles were performed. Carbon coated TiO_2 nanoparticles followed entirely different thermal behavior than that of TiO_2 nanoparticles. Hence it was experimentally shown that, the developed method is feasible and applicable to prepare thermally stable carbon-coated TiO_2 at low temperatures. The ease of using dextrose as carbon source and low temperature procedure, hence less cost production are advantages of this method. Additionally, authors state that this method can be applicable for the production of carbon coating on variety of semiconductor or metal nanoparticles. In another study, low-cost dichloromethane was used as carbon source for the preparation of ($C-TiO_2$) nanoparticles by a novel low cost hydrothermal method [26]. DR UV-vis spectrum detected additional absorption tails in visible region of more than 400 nm indicating the presence of carbon on the sample. Presence of the carbon layer on the surface of the particles was further supported by SEM observations. Moreover, the band gap values for carbon coated-TiO_2 samples calculated from the absorption spectra were around 0.7 eV which is considerably lower than bare TiO_2 [27], suggesting the influence of carbon in lowering the band gap energy of TiO_2. These studies indicate that surface modification of nanocrystalline TiO_2 with carbon compunds is an effective route to enhance photodecomposition of contaminations in aqeous solutions.

2. CONCLUSION

Despite considerable achievements on the preparation of the carbon-modified TiO_2 nanoparticles, there is a lack of general guidelines for their assessment. In this paper we presented a brief review on novel achievements in surface modification of TiO_2 nanoparticles aiming at enhanced TiO_2 photocatalytic efficiency, decreased electron-hole recombination, complete adsorption and decomposition of contaminant molecules and efficient utilization of visible fraction of solar light. It was shown that surface modification of nanocrystalline TiO_2 with carbon compunds is an effective route to enhance photodecomposition of

contaminants in aqeous solutions. Decomposition rate of the pollutants was found to be the result of a balance between the suppression of the transition from anatase to rutile and the decrease in UV rays reaching the TiO_2 surface, both of them being controlled by the carbon layer. In addition to the thickness of the carbon layer, the adsorptivity of carbon layer was found to be a determining factor for the photocatalytic activity of carbon-coated TiO_2. However, as the temperature promotes the separation of electron–hole pairs, most of these methods are involved with elevated temperature, and complex operating conditions. Additionally, some of the methods mentioned above required specific conditions, such as the controlled nitrogen atmosphere. Therefore, hydrothermal process has been illustrated as an alternative method that offers both low reaction temperature and simple preparation method. We believe this review will help to readers to choose suitable synthesis methods to construct carbon coating and to optimize the surface chemistry of titanium oxide nanoparticles for their interests.

3. REFERENCES

1. Ollis, D.F.; Pelizzetti, E., Serpone N./ Photocatalyzed destruction of water contaminants, Environ. Sci. Technol. 1991, 25, p.1523-1529.
2. Bahnemann, D.W.; Bockelmann, D., Goslich, R./ Mechanistic studies of water detoxification in illuminated TiO_2 suspensions, Sol. Energy Mater. 1991, 24, p.564-583.
3. Shen Qiu, Lifen Xiao, Xinping Ai, Hanxi Yang, and Yuliang Cao , Yolk−Shell/ TiO_2@C Nanocomposite as High-Performance Anode Material for Sodium-Ion Batteries, ACS Appl. Mater. Interfaces 2017, 9, p.345−353.
4. Shehzada N., Tahir M., Joharia K., Murugesan T., Hussain M./ A critical review on TiO_2 based photocatalytic CO2 reduction system: Strategies to improve efficiency, Journal of CO_2 Utilization, 26 2018, p.98-122.
5. Meng N., Leung M.K.H., Leung D.Y.C. and Sumathy K. /Renewable and Sustainable Energy Reviews, 2007,11(3), p.401-25.
6. Khan S., Mofareh Al-Shahry, Ingler W. / Efficient Photochemical Water Splitting by a Chemically Modified n-TiO_2, Science, 2002, 297(5590), p.2243-5.
7. Tan L.L., Ong, W.J., Chai S.P., Mohamed A.R. /Noble metal modified reduced graphene oxide/TiO_2 ternary nanostructures for efficient visible-light-driven photoreduction of carbon

dioxide into methane, Applied Catalysis B: Environmental, 2015, vol. 166–167, p.251-259.

8. Wang Y., Zhang J. / Investigations of Pulse Plasma Polymer Coating on TiO$_2$ Nanoparticles and Their Dispersion, 2011 p.899-909

9. Herrmann J.M., Matos J., Disdier J., Guillard C., Laine J., Malato S., Blanco J./ Solar photocatalytic degradation of 4-chlorophenol using the synergistic effect between titania and activated carbon in aqueous suspension. Catal Today 1999, 54, p.255–65

10. Blatnik J., Luebke L., Simonet S., Nelson M., Price R., Leek R., Zeng L., Wu A., and Brown E. / Dye Surface Coating Enables Visible Light Activation of TiO$_2$ Nanoparticles Leading to Degradation of Neighboring Biological Structures, Microsc. Microanal. 2012, 18, p.134–142,

11. Liu Y., Chen X., Li J., Burda C./ Photocatalytic degradation of azo dyes by nitrogen–doped TiO$_2$ nanocatalysts, Chemosphere 2005, 61, p.11–18.

12. Kondo K. , Murakami N. , Ye C. , Tsubota T. , Ohno T. / Development of highly efficient sulfur-doped TiO$_2$ photocatalysts hybridized with graphitic carbon nitride, Applied Catalysis B: Environmental, Vol. 142–143, October–November 2013, p. 362-367

13. Lin L., Lin W., Zhu Y.X., Zhao B.Y., Xie Y.C., He Y., Zhuet Y.F. / Uniform carbon-covered titania and its photocatalytic property. J. Mol. Catal. A: Chem. 2005, 236, p.46–53.

14. Sakthive S., Kisch, H./ Daylight Photocatalysis by Carbon-Modified Titanium Dioxide, Angew. Chem. Int. Ed. 42, 2003, p.4908.

15. Sakthive S., Kisch, H. /Photocatalytic and Photoelectrochemical Properties of Nitrogen Doped Titanium Dioxide, ChemPhysChem, 2003, 4, p.487

16. Xiao Q., Zhang J., Xiao C., Si, Z. Tan X./ Solar photocatalytic degradation of methylene blue in carbon-doped TiO$_2$ nanoparticles suspension, Sol. Energy 2008, 82, p. 706–713.

17. Lettmann C., Hildenbrand K., Kisch H., Macyk W., Maier W.F./ Visible light photodegradation of 4-chlorophenol with a coke-containing titanium dioxide photocatalyst, Appl. Catal. B, 2001, 32, p. 215-227.

18. Inakagi M., Kojin F., Tryba B., Toyoda M./ Carbon-coated anatase: The role of the carbon layer for photocatalytic performance, Carbon 2005, 43, p.1652

19. Inagaki M., Kobayashi S., Kojin F., Tanaka N., Morishita T., Tryba B./ Pore structure of carbons coated on ceramic particles, Carbon 2004;42:3153–8.

20. Inagaki M./ Carbon coating for enhancing the functionalities of materials, Carbon, 50(9), p.3247-3266.

21. Tsumura T., Kojitani N., Izumi I., Iwashita N., Toyoda M., Inagaki M./ Carbon coating of anatase-type TiO$_2$ and photoactivity, J. Mater. Chem. 2002, 12 , p.1391-1396.

22. Nawi M.A., Nawawi I./ Preparation and characterization of TiO$_2$ coated with a thin carbon layer for photocatalytic activity under fluorescent lamp and solar light irradiations, Appl. Catal. A: Gen., 2013, 453, p.80-91.

23. Warren S.C., Messina L.C., Slaughter L.S., Kamperman M., Zhou Q., Gruner S.M., DiSalvo F.J. and Wiesner U./ Ordered mesoporous materials from metal nanoparticle-block copolymer self-assembly, Science, 2008, 320, p.1748–1752.

24. Wang T., Jiang X. and Wu, Y. X./ Influence of Crystallization of Nano TiO$_2$ Prepared by Adsorption Phase Synthesis on Photodegradation of Gaseous Toluene, Ind. Eng. Chem. Res., 2009, 48, p.6224–6228

25. Olurode K., Neelgund G. M., Oki A., Luo Z./ A facile hydrothermal approach for construction of carbon coating on TiO$_2$ nanoparticles, Spectrochimica Acta Part A: Molecular and Biomolecular Spectroscopy, Volume 89, April 2012 , p. 333-336

26. Hatta M. H. M., Lintang H. O./ Buang and Yuliati N. A. L./ Simple and Low-cost Preparation of Carbon-Coated Titanium Dioxide via Hydrothermal Method, Advanced Materials Research, 2014,Vol 970, p. 279-282.

27. Anjum D.H, Memon N. K., Chung S. H./ Investigating the growth mechanism and optical properties of carbon-coated titanium dioxide nanoparticles, Mater. Lett, 2013,108, p.134-138.

75th anniversary of prominent scientist
Abdinov Ahmad Shahvalad oglu

Prof. A.Sh. Abdinov was born in May 30, 1945, Behrud village of Ordubad, Azerbaijan Republic. He graduated from high school in 1963and in the same year successfully graduated from the entered Faculty of Physics of Azerbaijan State University. During his study, A.Sh. Abdinov got "excellent" grades and became a pensioner named after Lenin. He graduated from the University with honors in 1968 with a degree in Physics. After graduating from the university, A.Sh. Abdinov was a full-time postgraduate student at the Institute of Physics and Technology named after A.F.Ioffe of the USSR Academy of Sciences in St. Petersburg in 1969-1971. He was accepted as a teacher at the Physics Faculty of the Azerbaijan State University.

A.Sh. Abdinov defended his PhD in 1972 and his doctoral dissertation in 1979 and became the youngest doctor of sciences, professor in physics in the Republic of Azerbaijan.

In 1971, he worked as an assistant at the Faculty of Physics of the Azerbaijan State University, then as a senior teacher (1974-1979), associate professor (1979-1981), professor (1981-1992), dean of the faculty (1988-1989), head of the department (1992- At the same time (1989-2005) he was the scientific director of the Scientific Research Laboratory "Solid State Electronics", and in 1993-2000 he served as Deputy Minister of Education of the Republic of Azerbaijan. For a long time he was the chairman, co-chair and chairman of the Physics Department of the Scientific-Methodical Council of the Ministry of Education of Azerbaijan.

Prof. A.Sh. Abdinov's scientific-pedagogical, organizational activity is great, but his scientific activity is richer and more colorful, so it has gained wide-scale fame. He began to conduct research during his student years and published his first scientific articles in the journals "Journal of Physical Chemistry" (Moscow-1968), "High-molecular compounds" (Moscow-1968). During his postgraduate studies, A.Sh. Abdinov was engaged in the study of phenomena related to electrons in semiconductors. In 1971, invented a fundamentally new and very high-sensitivity, low-inertia photo receiver.

Since 1972, Prof. A.Sh. Abdinov, in addition to semiconductors and electronic effects, he studied layered and chalcopyrite compounds, single crystals of solid solutions and various types of electrical instability observed in these semiconductors, unusual photoelectric phenomena, radiation effects, luminescence, injection and contact phenomena, and heterostructures. His scientific results made great contributions to the physics of electronic processes in non-homogeneous crystalline semiconductors. Scientists from different countries often refer to these scientific results and appreciate these results.

Prof. AB Abdinov is the author of several inventions, 5 textbooks for university students and about 430 scientific articles, including about 150 high-rated scientific journals ("Физика и техника полупроводников", «Физика» "Оптика и спектроскопия", "Известия ВУЗ-ов-Физика;"Микроэлектроника", "Прикладная физика", "Неорганические материалы", "Журнал физической химии"; «SPIE» «Yap. J.Appl. Phys., Optoelectronica; "Physical Status Solidi"). His scientific results have been published in the Russian Federation, the United States, France, Japan, Taiwan, the Islamic Republic of Iran, Ukraine, Belarus, Georgia, Kazakhstan, Uzbekistan, Turkmenistan, Lithuania, Turkey, Hungary and others. As many as 120 reports were presented at 75 international scientific conferences and symposiums held in up to 25 countries. He also tried to

solve applied problems on the basis of his fundamental scientific research and did a lot of work in this direction.

Prof. A.Sh. Abdinov was awarded the Republican Komsomol Prize in 1976 for his services and achievements in the field of science, in 1993 he was awarded the International Soros Foundation Prize, in 1995 he became a full member of the New York Academy of Sciences, in 2009 he worked in England. He was awarded the "Researcher of the Year" medal by the International Biography Center, the "Man of the Year" medal by the International Biographical Institute in the United States, the "Honorary Decree" of the Ministry of Education of the Republic of Azerbaijan in 2015, the "Labor Order" and the "Jubilee Order" in 2019.

Prof. Under the scientific guidance of A.Sh. Abdinov 22 master's, 30 candidate's and 7 doctors of sciences dissertations got their degrees. He was the official opponent of about 20 candidate and doctoral dissertations.

The editorial staff of LOW DIMENSIONAL SYSTEMS congratulates him on his 75th birthday and wishes him great success.